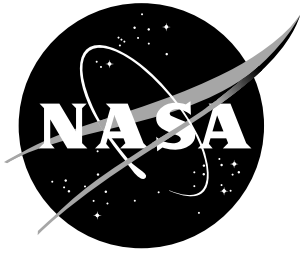


NASA/TP-2000-210310



# Dynamic Investigation of Static Divergence: Analysis and Testing

*Jennifer Heeg*  
*Langley Research Center, Hampton, Virginia*

---

November 2000

## The NASA STI Program Office ... in Profile

Since its founding, NASA has been dedicated to the advancement of aeronautics and space science. The NASA Scientific and Technical Information (STI) Program Office plays a key part in helping NASA maintain this important role.

The NASA STI Program Office is operated by Langley Research Center, the lead center for NASA's scientific and technical information. The NASA STI Program Office provides access to the NASA STI Database, the largest collection of aeronautical and space science STI in the world. The Program Office is also NASA's institutional mechanism for disseminating the results of its research and development activities. These results are published by NASA in the NASA STI Report Series, which includes the following report types:

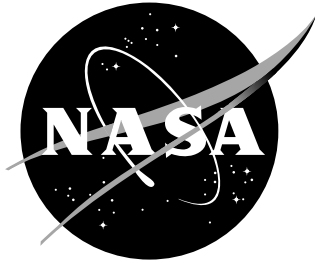
- **TECHNICAL PUBLICATION.** Reports of completed research or a major significant phase of research that present the results of NASA programs and include extensive data or theoretical analysis. Includes compilations of significant scientific and technical data and information deemed to be of continuing reference value. NASA counterpart of peer-reviewed formal professional papers, but having less stringent limitations on manuscript length and extent of graphic presentations.
- **TECHNICAL MEMORANDUM.** Scientific and technical findings that are preliminary or of specialized interest, e.g., quick release reports, working papers, and bibliographies that contain minimal annotation. Does not contain extensive analysis.
- **CONTRACTOR REPORT.** Scientific and technical findings by NASA-sponsored contractors and grantees.
- **CONFERENCE PUBLICATION.** Collected papers from scientific and technical conferences, symposia, seminars, or other meetings sponsored or co-sponsored by NASA.
- **SPECIAL PUBLICATION.** Scientific, technical, or historical information from NASA programs, projects, and missions, often concerned with subjects having substantial public interest.
- **TECHNICAL TRANSLATION.** English-language translations of foreign scientific and technical material pertinent to NASA's mission.

Specialized services that complement the STI Program Office's diverse offerings include creating custom thesauri, building customized databases, organizing and publishing research results ... even providing videos.

For more information about the NASA STI Program Office, see the following:

- Access the NASA STI Program Home Page at <http://www.sti.nasa.gov>
- E-mail your question via the Internet to [help@sti.nasa.gov](mailto:help@sti.nasa.gov)
- Fax your question to the NASA STI Help Desk at (301) 621-0134
- Phone the NASA STI Help Desk at (301) 621-0390
- Write to:  
NASA STI Help Desk  
NASA Center for AeroSpace Information  
7121 Standard Drive  
Hanover, MD 21076-1320

NASA/TP-2000-210310



# Dynamic Investigation of Static Divergence: Analysis and Testing

*Jennifer Heeg*  
*Langley Research Center, Hampton, Virginia*

National Aeronautics and  
Space Administration

Langley Research Center  
Hampton, Virginia 23681-2199

---

November 2000

---

Available from:

NASA Center for AeroSpace Information (CASI)  
7121 Standard Drive  
Hanover, MD 21076-1320  
(301) 621-0390

National Technical Information Service (NTIS)  
5285 Port Royal Road  
Springfield, VA 22161-2171  
(703) 605-6000

## ABSTRACT

The phenomenon known as aeroelastic divergence is the focus of this work. The analyses and experiment presented here show that divergence can occur without a structural dynamic mode losing its oscillatory nature. Aeroelastic divergence occurs when the structural restorative capability or stiffness of a structure is overwhelmed by the static aerodynamic moment. This static aeroelastic coupling does not require the structural dynamic system behavior to cease, however. Aeroelastic changes in the dynamic mode behavior are governed not only by the stiffness, but by damping and inertial properties. The work presented here supports these fundamental assertions by examining a simple system: a typical section airfoil with only a rotational structural degree of freedom.

Aeroelastic stability analysis is performed in the discrete time domain. The aerodynamic, structural dynamic, and downwash relationships are cast as time-marching equations and combined to form aeroelastic state space equations. The discrete time eigenvalues and eigenvectors of the coupled system are computed. This method is advantageous because the exact roots and the degree of stability of the system are determined, within the framework of the aerodynamic and structural dynamic representations. The discrete-time eigenvalues are transformed into the continuous time domain to facilitate their interpretation.

Results from the analysis have identified configurations of a simple model that exhibit different types of dynamic mode behavior as the system encounters divergence. For the simple configuration examined, these results indicate that low inertial properties and elastic axis location near the center of pressure promote divergence while the dynamic mode persists. Large inertias and large separation between elastic axis and center of pressure promote divergence where the dynamic mode becomes a static mode.

A wind tunnel model was designed and tested to examine divergence experimentally. The experimental results validate the analytical calculations and explicitly examine the divergence phenomenon where the dynamic mode persists. Three configurations of the wind tunnel model were tested. The experimental results agree very well with the analytical predictions of subcritical characteristics, divergence velocity and behavior of the noncritical dynamic mode at divergence.

## CONTENTS

ABSTRACT .....	i
LIST OF FIGURES.....	iii
LIST OF TABLES .....	vii
NOMENCLATURE.....	viii
INTRODUCTION.....	1
<u>Chapter</u>	
One BACKGROUND .....	4
Two ANALYSIS.....	13
Three EXPERIMENT .....	62
Four COMPARISON OF ANALYSIS AND EXPERIMENT .....	109
Five SUMMARY OF RESULTS.....	119
Six CONCLUSIONS & SUGGESTED FUTURE WORK .....	122
APPENDIX A: EQUATIONS OF MOTION .....	124
APPENDIX B: EIGENVECTOR INVARIANCE UNDER TRANSFORMATION....	135
BIBLIOGRAPHY .....	141

## LIST OF FIGURES

Figure 1 Eigenvalues for baseline case; discrete time eigenvalues, $z$ .....	16
Figure 2 Eigenvalues for baseline case; continuous time eigenvalues, $\lambda$ .....	17
Figure 3 Case I: Influence of varying the size of the aerodynamic elements. Continuous time eigenvalues, $\lambda$ .....	19
Figure 4 Case II: Influence of varying the number of aerodynamic elements in the wake. Continuous time eigenvalues, $\lambda$ .....	21
Figure 5 Case III: Influence of simultaneously varying the size and number of aerodynamic elements in the wake, maintaining a constant wake length. Continuous time eigenvalues, $\lambda$ .....	22
Figure 6 Typical section with pitch freedom .....	25
Figure 7 Discrete time root locus for configuration # 2.....	27
Figure 8 Discrete time root locus for configuration # 2, expanded scale.....	28
Figure 9 Continuous time root locus for configuration #2.....	29
Figure 10 Continuous time eigenvalues for configuration # 2 as functions of reduced velocity; a) Imaginary part, b) Real part .....	30
Figure 11 Surface of $\omega_D/\omega_\alpha$ as a function of mass ratio and radius of gyration. Elastic axis position is fixed, $e/b=0.375$ . .....	32
Figure 12 Surface of $\zeta_D$ as a function of mass ratio and radius of gyration. Elastic axis position is fixed, $e/b=0.375$ .....	33
Figure 13 Surface of $\omega_D/\omega_\alpha$ as a function of mass ratio and elastic axis position. Radius of gyration is fixed, $r_\alpha=0.5$ . .....	34
Figure 14 Surface of $\zeta_D$ as a function of mass ratio and elastic axis position. Radius of gyration is fixed, $r_\alpha=0.5$ .....	35
Figure 15 Surface of $\omega_D/\omega_\alpha$ as a function of elastic axis position and radius of gyration. Mass ratio is fixed, $\mu=50$ .....	36
Figure 16 Surface of $\zeta_D$ as a function of elastic axis position and radius of gyration. Mass ratio is fixed, $\mu=50$ . .....	37
Figure 18 Selected aerodynamic eigenmodes .....	43
Figure 19 Eigenvector associated with dynamic mode near zero velocity, associated continuous time eigenvalue $\lambda = -.16 + j 49.2$ .....	45
Figure 20 Eigenvector associated with dynamic mode at the divergence velocity, associated continuous time eigenvalue $\lambda = -17.7 + j 25.9$ .....	46
Figure 21 Vorticity portion of dynamic mode eigenvector for several velocities, magnitude and phase as functions of chord-wise location.....	47
Figure 22 Eigenvector associated with the unstable static mode just above the divergence velocity.....	48
Figure 23 Vorticity participation of last wake element, associated with the real eigenvalue that destabilizes .....	49

Figure 24 Root loci and vorticity ratio plots for a) wind tunnel model configuration 2; b) wind tunnel model configuration 1; c) the intermediate configuration and ; d) the traditional divergence configuration .....	50
Figure 25 Modal moments, configuration #2.....	53
Figure 26 Angle between eigenvectors as a function of reduced velocity, using all elements of the eigenvector.....	55
Figure 27 Angle between eigenvectors as a function of reduced velocity, using wake vorticities without last element .....	56
Figure 28 Angle between eigenvectors as a function of reduced velocity, using wing vorticities only.....	57
Figure 29 Angle between eigenvectors as a function of reduced velocity, only the structural dynamic portion of eigenvectors used.....	58
Figure 30 Angle between eigenvectors as a function of reduced velocity, only angular velocity component .....	59
Figure 31 Angle between eigenvectors as a function of reduced velocity, using only last element of the wake.....	59
Figure 32 Physical parameter variation results; ratio of frequency of dynamic mode at divergence to pitch mode natural frequency .....	64
Figure 33 Physical parameter variation results; damping of dynamic mode at divergence condition.....	65
Figure 34 Researcher installing wind tunnel model; airfoil shown with Plexiglass trailing edge segment .....	68
Figure 35 Ceiling mechanism of mount system.....	68
Figure 36 Floor mount mechanism, viewed from below .....	69
Figure 37 Stiffness data for 1 inch diameter torsional spring .....	70
Figure 38 Stiffness data for $\frac{3}{4}$ inch diameter torsional spring .....	71
Figure 39 Administering a pluck to the model.....	73
Figure 40 Divergence of wind tunnel model configuration #2 .....	75
Figure 41 Strain monitoring for predicting divergence onset .....	76
Figure 42 Predicting divergence using angle of attack ratio .....	77
Figure 43 Intermediate Southwell plot.....	78
Figure 44 Southwell method for predicting divergence onset .....	78
Figure 45 Southwell method results using increasing amounts of data .....	79
Figure 46 Frequency tracking to predict divergence.....	80
Figure 47 Inverse amplitude of the power spectral density of the angle of attack response .....	80
Figure 48 Extracting logarithmic decrement data from angle of attack time history, air off data for configuration # 2 .....	81
Figure 49 Logarithmic decrement results; large symbols are average values for each dynamic pressure.....	83
Figure 50 Frequency domain representations for extracting modal parameter data .....	84
Figure 51 Amplitude of Fourier transformation of angle of attack; Configuration # 2, dynamic pressure 1.52 psf.....	85



Figure 52 Real part of measured modal data as functions of dynamic pressure, Configuration # 2 .....	86
Figure 53 Imaginary part of measured modal data as functions of dynamic pressure, Configuration # 2 .....	88
Figure 54 Root locus of experimental data as dynamic pressure is varied .....	89
Figure 55 Divergence of wind tunnel model configuration #1 .....	90
Figure 56 Real part of measured eigenvalues, Configuration # 1 .....	92
Figure 57 Imaginary part of measured eigenvalues, Configuration # 1 .....	93
Figure 58 Root locus using experimental data, Configuration # 1 .....	94
Figure 59 Divergence of wind tunnel model configuration #3 .....	95
Figure 60 Real part of measured eigenvalues, Configuration # 3 .....	96
Figure 61 Imaginary part of measured eigenvalues, Configuration # 3 .....	97
Figure 62 Root locus as a function of dynamic pressure, Configuration # 3 .....	97
Figure 63 Hard limit instability encountered as dynamic pressure is increased, (Configuration #2) .....	98
Figure 64 Divergence encountered while at constant dynamic pressure .....	99
Figure 65 Divergence encountered while at constant dynamic pressure, expanded scale .....	99
Figure 66 Regions of behavior for the airfoil .....	100
Figure 67 Nonlinear system divergence for configuration 1 at constant dynamic pressure .....	102
Figure 68 Nonlinear system divergence for configuration 3, tab 976, as velocity is slowly increased until divergence condition .....	103
Figure 69 Instability encountered for several values of rigid angle of attack, Configuration #2 .....	104
Figure 70 Instability encountered for several values of rigid angle of attack, each at a different dynamic pressure, Configuration #1 .....	105
Figure 71 Instability encountered for several values of rigid angle of attack, each at a different dynamic pressure, Configuration #3 .....	106
Figure 72 Comparison of analytical and experimental results for configuration # 2, frequency of system behavior as a function of dynamic pressure .....	110
Figure 73 Comparison of analytical and experimental results for configuration # 2, damping behavior as a function of dynamic pressure .....	111
Figure 74 Comparison of analytical and experimental results for configuration # 2, root locus as dynamic pressure is varied .....	112
Figure 75 Comparison of analytical and experimental results for configuration # 1, imaginary part as a function of dynamic pressure .....	113
Figure 76 Comparison of analytical and experimental results for configuration #1, real part as a function of dynamic pressure .....	114
Figure 77 Comparison of analytical and experimental results for configuration #1, root locus as a function of dynamic pressure .....	115
Figure 78 Comparison of analytical and experimental results for configuration # 3; frequency versus dynamic pressure .....	116
Figure 79 Comparison of analytical and experimental results for configuration # 3; damping characteristic versus dynamic pressure .....	117

Figure 80 Comparison of analytical and experimental results for configuration # 3; root locus as dynamic pressure is varied .....	118
---	-----

## LIST OF TABLES

Table 1 Aerodynamic Configurations .....	18
Table 2 Comparison Cases for Parametric Variations .....	18
Table 3 Nondimensional parameters of aeroelastic system .....	25
Table 4 Parameter values used in analysis, wind tunnel model configuration #2 .....	26
Table 5 Structural dynamic parameters associated with wind tunnel model configurations .....	39
Table 6 Analytical calculation of divergence conditions .....	40
Table 7 Static equilibrium calculations of divergence conditions .....	41
Table 8 Eigenvector numbering and description.....	44
Table 9 Dynamic mode frequencies estimated from wake portion of dynamic mode eigenvector and calculated from analysis.....	47
Table 10 Parameter Values for traditionally divergent configuration.....	52
Table 11 Analytical frequency ratios and damping at divergence .....	66
Table 12 Description of wind tunnel model configurations.....	66
Table 13 Frequency ratios of experimental data .....	106
Table 14 Comparison of analysis and experimental values for configuration # 2.....	112
Table 15 Comparison of analysis and experimental values for configuration # 1 .....	115
Table 16 Comparison of analysis and experimental values for configuration # 3.....	118

## NOMENCLATURE

### Symbols:

A	Aerodynamic matrix
a	Amplitude of cycles, used in logarithmic decrement method
B	Aerodynamic matrix
b	Semi-chord
C	Aeroelastic force matrix
$C_{L\alpha}$	Lift curve slope
D	Structural dynamic matrix
E	Downwash matrix
e	Elastic axis position, measured positive aft from the center of pressure
f	Aerodynamic load vector
$f_\alpha$	Frequency of torsional mode (Hz)
$I_\alpha$	Torsional inertia
j	Imaginary number, $j = \sqrt{-1}$
k	Reduced frequency, ( $k=\omega b/U$ )
$L_{wake}$	Length of the wake
M	Number of aerodynamic elements on the wing

$m$	Mass
$N$	Total number of aerodynamic elements
$n$	Time step number
$N_{\text{cycles}}$	Number of cycles
$N_{\text{wake}}$	Number of aerodynamic elements in the wake
$q$	Generalized structural coordinates
$q$	Dynamic pressure
$r_{\alpha}$	Radius of gyration
$U$	Velocity
$V$	Reduced velocity, ( $V=U/\omega_{\alpha}b$ )
$w$	Downwash
$x$	Vector of locations of vortices in the aerodynamic model; chord-wise location
$z$	Discrete time eigenvalue
$\Delta t$	Time step size, temporal discretization
$\Delta x$	Aerodynamic element size, spatial discretization
$\Gamma$	Vorticity vector
$K$	Aerodynamic kernel function
$K_{\alpha}$	Torsional stiffness
$M$	Moment
$\alpha$	Angle of attack

$\delta$	Logarithmic decrement
$\lambda$	Continuous time eigenvalue
$\lambda$	Intermediate Southwell parameter, slope of moment vs. rigid angle of attack
$\mu$	Mass ratio
$\rho$	Density of air
$\omega$	Frequency (radians/second)
$\omega_\alpha$	Frequency of torsional mode (radians/second)
$\xi$	Vector of locations of collocation points in the aerodynamic model
$\zeta$	Damping

**Superscripts:**

n	time step number
---	------------------

**Subscripts:**

$\alpha$	pertaining to the torsional degree of freedom
mode	pertaining to a specified mode
D	pertaining to the divergence condition
i,j	designation for an element of a matrix which lies in the ith row, jth column
wing	quantity on the wing

wake	quantity in the wake
TE	trailing edge
A	pertaining to the aerodynamics
S	pertaining to the structure
0	vector or quantity at time 0
1	matrix multiplies vector at time step n
2	matrix multiplies vector at time step n+1
o	the rigid value of a quantity
e	the elastic increment of a quantity

## INTRODUCTION

Aeroelasticity is concerned with systems in which there is substantial interaction among the aerodynamic, inertial and structural forces of an object. The phenomenon known as aeroelastic divergence occurs when the structural restorative capability or stiffness of a structure is overwhelmed by the static aerodynamic moment. The static aeroelastic coupling that produces divergence does not require the dynamic system behavior to cease, however. Aeroelastic changes in the dynamic mode behavior are governed not only by the stiffness, but by damping and inertial properties.

The work presented supports these assertions by examining a simple system: a typical section airfoil with only a rotational structural degree of freedom. The analyses and experiment to be presented show that divergence can occur without a structural dynamic mode losing its oscillatory nature and becoming static.

The aeroelastic analysis method utilized in this study allows calculation of the eigenvalues or modal characteristics of a system for subcritical, critical and supercritical systems. The primary analysis is performed in the discrete time domain. The aerodynamic, structural dynamic, and downwash relationships are cast as time-marching equations and combined to form aeroelastic state space equations. The discrete time eigenvalues and eigenvectors of the coupled system are computed. The discrete-time eigenvalues are transformed into the continuous time domain to ease interpretation. This method is advantageous, as the exact roots and the degree of stability of the system are determined, to the extent of the accuracy of the aerodynamic and structural dynamic representations. The method differs from traditional aeroelastic analyses. Background information is provided on these traditional methods, which reveals differences between the current method and each of them. Most of the traditional analyses produce results that are only valid for neutrally stable behavior. This limitation is often not in the stability method itself, but rather in approximations in the aerodynamic behavior. The current analysis method resembles the p-method to be discussed, but the fundamental quantity,  $p$ , has been replaced by the discrete time unit delay operator,  $z$ .

The discrete-time aeroelastic eigenanalysis method was used to examine the aerodynamic and structural parametric space of a typical section airfoil that had a single structural degree of freedom. These results distinguished configurations where different types of dynamic mode behavior were observed as the system encountered divergence. This facilitated the design of an experiment which encountered divergence while the structural dynamic mode persists.

A wind tunnel model was designed and tested to examine divergence experimentally and validate the analytical calculations. All freedom of motion was denied to the airfoil,



except for rotation about the elastic axis. Allowing only the single structural degree of freedom eliminated the complications of interpreting modal interaction effects or participation of multiple modes in the divergence mechanism. This simplicity allowed the focus to be precisely on the coupling of the aerodynamics with the structural pitching motion. Three configurations of the wind tunnel model were tested to examine the effects of a limited range of torsional stiffness and inertia. All three configurations exhibited divergence of a static mode existing simultaneously with a dynamic mode. The constraints imposed by the fundamental design of the model limit the potential source of both the statically unstable mode and the measured dynamic mode. The mode that originates as the structural dynamic pitch or torsional mode was tracked at subcritical airspeeds. As the dynamic pressure was increased, the aeroelastic coupling changes the damping and frequency of this tracked mode. At divergence, this mode appears as a damped oscillatory mode. The frequency and damping of the dynamic mode are complicated functions of the air-off system characteristics.

There are several notable examples in aeroelastic literature where this category of behavior has been produced by analysis or noted in experiment. More notably, however, there is a century of experimentation in which this phenomenon has not been observed. The current work utilizes a very simple system. In extension to more complicated systems, the phenomenon may change or simply be more difficult to observe. This category of system behavior has not been widely predicted by analysis and generally the dynamic mode behavior is very damped, both factors making it difficult to locate in an experimental setting.

Knowledge of the subcritical, supercritical and noncritical mode behavior is an asset for many reasons. Understanding the fundamental physics of a system is a good thing all by itself, of course. However, in addition, two practical reasons to have this knowledge come immediately to mind. Test techniques for predicting divergence onset have included frequency tracking of dynamic modes- divergence onset being indicated by the nearness of this frequency to zero. For configurations where divergence occurs without a structural dynamic mode losing its oscillatory nature this technique would not alert one to the onset of divergence. A second practical reason to understand the noncritical mode behavior is related to control applications. As active control of aeroelastic responses becomes more commonplace, it becomes more vital to understand the behavior of system modes which are noncritical for the uncontrolled or open loop system. Control law designs which are model-based rely on modal knowledge of system characteristics, not simply stability.

The body of this paper first presents a discussion of aeroelastic analysis methods and a historical perspective of programs which studied the divergence phenomenon. In the background material, a discussion is presented of past research that studied divergence mechanisms. The present analysis method and results are then presented and discussed. These results include a discussion and examples of the parametric database that delineates regions where the dynamic mode behavior at divergence changes. Detailed

analytical results are presented for one configuration of the wind tunnel model design. These results include stability analysis and study of the eigenvectors. Brief results are presented for the two additional wind tunnel model configurations. Analytical results are also presented for a set of parameters which produces divergence after the structural dynamic originated mode has become non-oscillatory. The experiment is next described. The model design process is summarized, as well as the hardware employed. The experimental techniques and data reduction methods are addressed. The results of the experiment are presented for the three configurations tested. The data are presented and discussed in the following order: determination of the divergence condition, subcritical techniques for predicting divergence onset, system behavior at divergence, and subcritical modal characteristics. Analytical and experimental results are then compared in terms of the divergence dynamic pressure and modal characteristics. The body of this work concludes with a discussion, summary of conclusions and suggestions for future directions.

## CHAPTER ONE

### BACKGROUND

Aeroelasticity is concerned with problems in which there is substantial interaction among the aerodynamic, inertial and structural forces of an object. When a body moves through the atmosphere, or when a body is placed in a wind tunnel, aerodynamic forces act over its surface. If the body is deformed, there is a change in the magnitude and distribution of these surface forces. This redistribution causes additional deformations; the result is an interactive feedback loop between aerodynamic loads and aircraft deflections.<sup>1</sup> Static aeroelastic behavior is generally considered to be a study of the mutual interaction between static aerodynamics and the stiffness, but not the inertia, of an elastic structure.

Background material is presented on several topics which unite in this work. Methods which have been used to examine aeroelastic stability are discussed first. A historical look at programs which have studied aeroelastic divergence is then presented. Focusing on divergence by virtue of an aerodynamic-originated root, as distinct from a root of structural origin, then follows.

#### *Aeroelastic Stability Methods*

Methods for analyzing the stability of an aeroelastic system set the foundation for the work to be presented. The classical methods of solving for stability of the aeroelastic equations are the p-method, the k-method and the p-k method. Each of these methods, which go by several names, will be discussed in the following paragraphs. In the following methods, the non-dimensional Laplace operator, or differential operator, is denoted p. In addition to these well-established methods, the g-method will also be briefly discussed.

The linearized equations of motion for a flexible aircraft contain unsteady aerodynamic terms, which depend on the Mach number,  $M$ , and the reduced frequency,  $k$ . For all but the simplest aerodynamic theories, the exact aerodynamic coefficients which are dependent on  $M$  and  $k$ , have not been developed in the form of algebraic functions. As a result, aerodynamic coefficients are often computed for each desired Mach number for a set of predetermined values of reduced frequency.

---

<sup>1</sup> Weisshaar, Terrence B., *Fundamentals of Static Aeroelasticity*; Dowell, Earl H., Edward F. Crawley, Howard C. Curtiss Jr, David A. Peters, Robert H. Scanlan and Fernando Sisto. *A Modern Course in Aeroelasticity*; Raymond L. Bisplinghoff and Holt Ashley, *Principles of Aeroelasticity*

The k-method is also known as the V-g method or the American method of flutter solution to determine the aeroelastic stability of a system. Many aerodynamic formulations, such as the Doublet Lattice method, lead to aerodynamic matrices which are only valid for harmonic motion,  $p=ik$ . Using these simple harmonic loads, and introducing an artificial structural damping factor, complex roots are obtained from the equations. There are several well-known disadvantages to the k-method. The complex eigenvalues obtained do not represent the actual damping or frequency of the system modes except for neutrally stable roots, where the damping is zero. Many solutions are required to obtain “matched-point” flutter boundaries. For a given airspeed, several solutions with different frequencies may occur. Information regarding non-critical conditions and eigenvalues is only qualitative.

The p-k method, sometimes referred to as the “British Method” or as Hassig’s modified version of the Frazer and Duncan method, attempts to improve upon the k-method by allowing the reduced frequency to be complex. In 1971, in discussing the p-k method, Hassig wrote, “It is generally conceded that it is desirable to formulate and solve the flutter equation such that the solution leads to a value for the rate of decay. Ideally, this requires the formulation of the unsteady aerodynamics matrix as a function of the complex variable  $p$ . When one wants to work with exact theoretical aerodynamics one must work with a formulation for harmonic motion and devise approximate methods to determine the rate of decay.” The equations of motion are written in a form indicating that the aerodynamic matrix is available only for harmonic motion. The eigenvalues of this approximate system can be solved, producing complex roots. The aerodynamics are then recomputed using the frequency that resulted from the eigenvalue computation. The equations of motion in the p-k method are solved in an iterative fashion so that the assumed value of  $k$  converges to the computed value of the imaginary part of a pre-selected eigenvalue. The iterations are repeated, for a single mode at a time, until all the modes have achieved convergence. There are several disadvantages to the p-k method. While the results for the flutter condition are shown to be quite good, the eigenvalues of damped modes are only approximate. The calculated damping is only good for low levels of damping. Another disadvantage of the p-k method is the requirement to track the eigenvalues of the system as the velocity or dynamic pressure is increased. For an  $n$ -degree of freedom system, as each mode is tracked, the equations produce  $n$  eigenvalues. Selection of the proper root is vital to the success of the method.

The p-method is the simplest method to understand, but perhaps the most difficult to apply. Utilizing the p-method means simply solving for the complex eigenvalues of the governing equations. Bisplinghoff and Ashley<sup>2</sup> comment on the process of finding eigenvalues of an aeroelastic system to determine stability: “The system consisting of a typical section in an airstream possesses dynamic eigenvalues. The critical (instability) condition is defined to occur at the lowest speed ... at which the damping ratio of any aeroelastic mode passes through zero. Mathematically they consist of values of the complex (non-dimensional Laplace) variable,  $p$ , which cause the determinant of the

---

<sup>2</sup> Raymond L. Bisplinghoff and Holt Ashley, *Principles of Aeroelasticity*

(nondimensionalized coupled aeroelastic system) matrix to vanish. Because (the aerodynamic velocity potentials) are transcendental functions (of  $p$ ), there exists in theory an infinity of such roots. So, with the air included, (the aeroelastic system) has an infinite number of degrees of freedom. ... The most logical way of studying the dynamic aeroelastic stability of a structure... could seem to be to calculate the root locus of  $p$  as a function of airspeed and altitude. In engineering practice, however, this has not been the customary approach, as ... more data are available on airloads resulting from simple harmonic motion.” The  $p$ -method avoids the iteration process by using explicit expressions for the aerodynamics. If the aerodynamics can be expressed as a sufficiently simple function of  $p$ , the aeroelastic equations define a polynomial in  $p$ . The main difficulty with the  $p$ -method lies in the derivation of appropriate aerodynamic expressions. The  $p$ -method has been used with quasi-steady aerodynamics represented by a first order differential equation, which ignores any effect of the wake. Two methods of approximating higher order aerodynamic theories are the Pade method by Vepa<sup>3</sup> and the minimum state method by Karpel and Hoadley<sup>4</sup>. These methods apply rational polynomial fits to the tabular values of the complex aerodynamic coefficients which were derived for oscillatory motion. Another method of approximation was developed by Nissim<sup>5</sup>, in which a second order complex coefficient fit is used rather than a rational function approximation.

A damping perturbation method, named the  $g$ -method, has recently been developed by Chen<sup>6</sup>. This is a generalization of the  $k$ -method and the  $p$ - $k$  method. The basic assumption is that a first order Taylor series approximation in  $g$  can be developed. Chen utilizes analytical continuation to replace the derivative with respect to  $g$  with a derivative with respect to reduced frequency. He states that this substitution is valid in the complete  $p$ -domain except along the negative real axis in subsonic flow. The  $g$ -method produces results that agree well with well-established methods. His method also yields some results in which aerodynamic lag divergence is illustrated. He explicitly points out that damping results of the  $p$ - $k$  method are valid for where damping or reduced frequency are zero or where the change (derivative) in the aerodynamics with respect to reduced frequency is zero.

### ***Divergence, down through the ages***

New flight vehicle concepts often invigorate the study of aeroelasticity, as new types of interactions are anticipated or observed. Examining the literature on divergence, several

---

<sup>3</sup> Vepa, R., *On the use of Pade Approximants to Represent Unsteady Aerodynamic Loads for Arbitrarily Small Motions of Wings*

<sup>4</sup> Karpel, Mordechai, and Sherwood Tiffany Hoadley, *Physically Weighted Approximations of Unsteady Aerodynamic Forces Using the Minimum-State Method*

<sup>5</sup> Nissim, E., *Flutter Analysis Using a New Complex  $p$ -Method*

<sup>6</sup> Chen, P.C. *A Damping Perturbation Method for Flutter Solution: The  $g$ -Method.*

programs or research areas stand out as having inspired the study of aeroelastic divergence.

Consideration of various planforms sparked work in static divergence at the National Advisory Committee for Aeronautics (NACA) in the 1940's and 1950's. Diederich and Budiansky<sup>7</sup> conducted analytical and experimental research into swept and tapered wings which resulted in charts and approximate formulae for estimating wing divergence for various configurations. This work demonstrated among other things, the dramatic decrease in the divergence speed for a wing that was swept forward. The analytical work investigating different planforms was continued by Diederich and Foss<sup>8</sup>, as they produced an analytical method of calculating divergence of wings with various planforms including delta wings. A summary of the NACA analytical efforts is provided by Diederich<sup>9</sup>.

The 1970's and 1980's brought a resurgence in the study of static aeroelastic effects. Advances in composite materials lead to a reconsideration of the forward-swept wing concept, which had been previously dismissed due to divergence. A study by Krone<sup>10</sup> showed clearly that "the detrimental effect of divergence on forward swept airfoils can be successfully controlled. By tailoring the composite layer thickness distributions and orientations a design can be obtained that produces optimum stiffness and strength characteristics ... with little fear of suffering the weight penalties that have previously been caused by the divergence phenomenon." Static aeroelastic characteristics of forward swept wings were investigated by many aeroelasticians. To note a few, Weisshaar<sup>11</sup> discussed forward-swept wing divergence from a fundamental concepts point-of-view, and Blair<sup>12</sup> performed wind tunnel experiments which demonstrated the fundamental relationships among sweep, composite fiber orientation and divergence speed. An experimental study of the static aeroelastic divergence of forward-swept wings was conducted in the NASA Langley Transonic Dynamic Tunnel by Ricketts and Doggett<sup>13</sup>. Flat plate models with varying geometry were tested. Six subcritical response testing techniques were formulated and evaluated at transonic speeds for accuracy in predicting static divergence. Ricketts and Doggett concluded that, "in general, the static methods seemed to consistently give better quality data than the dynamic methods." As pointed out by Doggett and Ricketts, dynamic methods of divergence prediction produce inferior results to those produced by static methods. The current work addresses the issue of why this is true. The dynamic behavior is governed not only by the stiffness (static) properties but by the inertial properties. Dynamic methods work only if a complex mode

---

<sup>7</sup> Diederich, Franklin W., and Bernhard Budiansky, *Divergence of Swept Wings*

<sup>8</sup> Diederich, Franklin W., and Kenneth A. Foss. *Static Aeroelastic Phenomena of M-, W-, and  $\square$ -Wings*.

<sup>9</sup> Diederich, Franklin W., *Divergence of Delta and Swept Surfaces in the Transonic and Supersonic Speed Ranges*

<sup>10</sup> Krone, Norris J., Jr., *Divergence Elimination with Advanced Composites*.

<sup>11</sup> Weisshaar, Terrence B. *Forward Swept Wing Static Aeroelasticity*.

<sup>12</sup> Blair, Maxwell, *Wind Tunnel Experiments on the Divergence of Swept Wings with Composite Structures*

<sup>13</sup> Rodney H. Ricketts, and Robert V. Doggett, Jr, *Wind-tunnel Experiments on Divergence of Forward-Swept Wings*.

of the system becomes real. A survey article by Shirk, Hertz and Weisshaar<sup>14</sup> provides an extensive reference list for other work on this subject.

Two forward swept wing airplanes were designed, built and flight tested. “Grumman Aircraft Corporation built two X-29's. Phase 1 of the project, using aircraft No. 1, was flown from December 1984 to 1988 and investigated handling qualities, performance, and systems integration. Phase 2 of the X-29 program involved aircraft No. 2 and studied the high angle of attack characteristics and military utility of the X-29.<sup>15</sup> “ In the development of the flight vehicle concept, dynamic analysis and wind tunnel testing of a free-free configuration was performed by Miller, Wykes and Brosnan<sup>16</sup>. Their analyses revealed a different type of instability. The phenomenon involved a coupling between the wing divergence mode and the aircraft short period mode, termed rigid body/ wing bending flutter. The analytical results showed that the wing response was completely different from the cantilevered case. While the divergence of the forward swept wing flight vehicle was controlled by aeroelastic tailoring, the coupling of the wing divergence-prone mode and the rigid body motion was controlled by enhancement of the stability augmentation system (SAS). One of the research objectives for the X-29 flight test program became correlating flight data with the predicted structural stability and determination of the aeroservoelastic stability margins.<sup>17</sup> In testing the X-29, methods of divergence prediction as applied to flight tests were investigated. Schuster and Lokos focused on applying the Southwell method to flight test data. Consideration of potential errors lead to a more conservative pace in envelope expansion than might otherwise have been required.

The 1990's topic in divergence centered around the National Aerospace Plane (NASP). Researchers working on this program examined divergence of all-moveable surfaces, which were representative of wing configurations under consideration. Experimental data was obtained in a supersonic test conducted in the Unitary Plan Wind Tunnel at the NASA Langley Research Center<sup>18</sup>. The wing models had low aspect ratios and highly swept leading edges. The wings were attached by a single-pivot mechanism along the wing root. The supersonic divergence was predicted to be primarily dependent on the first wing pitch mode. Two subcritical response instability prediction techniques were used: the static Southwell method and the dynamic frequency tracking method. The improved Southwell method uses the change in slope of load-versus-angle of attack measurements as dynamic pressure is increased to predict divergence conditions. Accurate predictions were not obtained for this wind tunnel model using measurements from the strain gauge bridges on the pitch stiffness elements. The frequency of the wing

---

<sup>14</sup> Shirk, M.H., T.J. Hertz, and T.B. Weisshaar. *Aeroelastic Tailoring- Theory, Practice, and Promise*.

<sup>15</sup> <http://www.dfrc.nasa.gov/gallery/photo/X-29>

<sup>16</sup> Miller, Gerald D., John H. Wykes and Michael J. Brosnan. *Rigid Body-Structural Mode Coupling on a Forward Swept Wing Aircraft*

<sup>17</sup> Sefic, Walter J., and Cleo M. Maxwell, *X-29A Technology Demonstrator Flight Test Program Overview*

<sup>18</sup> Stanley R. Cole, James R. Florance, Lee B. Thompson, Charles V. Spain and Ellen P. Bullock, *Supersonic Aeroelastic Instability Results for a NASP-like Wing Model*.

pitch mode was tracked as the dynamic pressure was incrementally increased in the wind tunnel, and the model vibration frequency as it approached zero at the divergence condition was monitored. Extrapolation of subcritical measured frequencies was then performed. This method was successfully used during the wind tunnel test to extrapolate divergence dynamic pressure and as guidance in anticipating actual divergence instabilities.

It is interesting to note that the experimental data show that divergence occurred at dynamic pressures only 3-6 percent beyond the dynamic pressure at which the frequency reaches a value that is fifty percent of the wind off natural frequency. As described by the authors, there is a large change in frequency that is determined only by observing the dynamic pressure of the instability itself. For two of the Mach numbers for the nominal stiffness configuration, the nearest subcritical data indicates that the mode has a frequency that is at 50% of its wind off value. For the other two cases, however, there is subcritical data which show the pitch mode frequency has dropped much further just prior to divergence.

### *Non-traditional divergence*

Static divergence that occurs without a structural dynamic mode losing its oscillatory nature and becoming static is central to the current work. A very interesting body of work on this subject exists in the literature. Studies will be discussed which were performed by Rodden and various co-authors, Edwards, Dashcund and Martin and Watkins. Already mentioned in the discussion of stability methods is the work of Chen, in which aerodynamic lag divergence was also found.

From 1969 to 1994, publications by Rodden and various coauthors present analytical results which demonstrate aerodynamic lag divergence and provide a method for calculating the true damping of non-critical modes. In the first of these articles, Rodden and Stahl<sup>19</sup> performed aeroelastic stability analysis utilizing the p-method. A transient formulation of the flutter and divergence problems was presented using aerodynamic strip theory and an exponential approximation (the W.P. Jones approximation) to the Wagner function. The limitation of the method presented in the referenced work is in the aerodynamic strip theory approximation.

A cantilevered wing with 5 structural modes was analyzed. The divergence velocity was found and agreed very well with static calculations. Using the p-method, they determined the subcritical frequencies and dampings. They discovered that tracking the frequency of the mechanical modes did not produce the instability. Tracking the aerodynamic lag roots, which are explicitly present due to the W.P. Jones approximation, produced the divergence instability. Their results show the first mode frequency curve decreased rapidly at speeds slightly higher than the divergence speed. The frequency

---

<sup>19</sup> William P. Rodden and Bernhard Stahl, *A Strip Method for Prediction of Damping in Subsonic Wind Tunnel and Flight Flutter Tests*.



went to zero in a small range of velocity and then increased rapidly. Their results are also show that the subcritical damping values differ significantly from the artificial damping predicted by another stability analysis method, except for the instances where the modes behave in a nearly simple harmonic fashion.

Additional work published by Rodden, Harder and Bellinger<sup>20</sup> compared the p-method results from the above work to results utilizing a p-k solution. While the divergence velocity predicted by the two methods agreed, this publication indicated that the divergence mechanisms predicted disagreed. The p-method indicated that the mechanism was aerodynamic lag divergence; the p-k method predicted divergence of the first bending mode. The matter was revisited<sup>21</sup> and the p-k results reinterpreted. The transition from the bending mode to the aerodynamic lag root was then recognized, bringing the predicted divergence mechanisms into agreement- an aerodynamic lag divergence.

The previously cited references analyzed a cantilevered wing. This work was extended to include a vehicle plunge mode<sup>22</sup>. Applying the aerodynamic approximations and p-method analysis technique predicted instability of an aerodynamic lag root. In the unrestrained system the instability is oscillatory as the unstable aerodynamic mode is coupled with the vehicle plunge freedom.

The cantilevered configuration was revisited by Rodden and Johnson in 1994<sup>23</sup>. The subsonic Doublet-Lattice aerodynamic method was employed in a p-k solution procedure. This analysis shows no aerodynamic lag root present in the divergence mechanism. They commented that the first bending frequency moved smoothly to zero frequency. They assert in this publication that the demonstrated discontinuous behavior of the eigenvalues is not due to a physical phenomenon, but due to the change in the definition of damping when a root becomes real. The authors do not comment in this publication on anticipated inaccuracies due to aerodynamic modeling or inexactness of the p-k solution for predicting subcritical characteristics.

Aerodynamic mode divergence was also illustrated in an analytical study by Edwards<sup>24</sup>. In this work, he discussed aerodynamic modeling in depth and notes some of the shortcomings of different aeroelastic stability methods.

Edwards began with a solution of the linearized potential equation for the case of two-dimensional airfoils undergoing simple harmonic motion in incompressible flow, published by Theodorsen. He next extended the derivation to arbitrary motion or

---

<sup>20</sup> William P. Rodden, R.L. Harder and E. Dean Bellinger, *Aeroelastic Addition to NASTRAN*.

<sup>21</sup> William P. Rodden and E. Dean Bellinger, *Aerodynamic Lag Functions, Divergence and the British Flutter Method*.

<sup>22</sup> William P. Rodden and E. Dean Bellinger, *Unrestrained Aeroelastic divergence in a Dynamic Stability Analysis*.

<sup>23</sup> William P. Rodden and Erwin H. Johnson, *MSC/NASTRAN Aeroelastic Analysis User's Guide*.

<sup>24</sup> John E. Edwards, *Unsteady Aerodynamic Modeling and Active Aeroelastic Control*.

complex values of reduced frequency. He called this the generalized Theodorsen aerodynamic representation. The expressions for the aerodynamic loads, lift and pitching moment, were incorporated into typical section equations of motion. The stability of the aeroelastic system was investigated using the p-method. The advantage of the p-method is that the exact roots and the degree of stability of the system are determined, to the extent of the accuracy of the aerodynamic representation. Edwards' presented a derivation and analytical results which produce an aerodynamic mode at divergence. This mode produces the motion of the diverging airfoil and occurs in addition to the structural poles. Inherent in his work is the realization that the aerodynamic equations are not constant coefficient equations. The fundamental theorem of algebra<sup>25</sup> states that an nth order polynomial equation is guaranteed to have exactly n roots for the case of constant coefficients. In the case of the Theodorsen aerodynamic representation, the coefficients of the governing polynomial are not constants and as such, no guarantee as to the number of roots can be asserted.

The occurrence of this divergence mode was studied by locating the poles of the system in the complex plane. Both the exact system model and a Pade approximate model were used to locate these poles. The divergence speed was indicated for the exact model by the emergence of an additional real pole on the positive real axis. The Pade model contained an eigenvalue which migrated from the stable negative real axis into the unstable positive real axis. Both results produced the same value for divergence speed.

Divergence in the case of a wing instead of a typical section was investigated by Dashcund<sup>26</sup>, the distinction being that his model had wing modes, not rigid pitch and plunge degrees of freedom. In the course of performing a flutter suppression study using active control, Dashcund discovered that for his configuration a non-structural originated root diverged. Divergence is mainly addressed by the analytical portion of the work. The equations of motion were generated employing a Rayleigh-Ritz energy method. The included modes were beam bending modes and rod twisting modes. The aerodynamics were full unsteady 2-D strip theory. Dashcund writes: "Modeling the unsteady aero in the Laplace domain in terms of an irrational, exact representation of the generalized Theodorson function shows the presence of additional stability roots which are not associated with the structural modes of the system nor with the feedback compensation or control surface actuator dynamics. The existence of these additional aerodynamic system roots, which includes the divergence root, is confirmed by the qualitatively good agreement between predicted and experimental divergence boundaries for the active flutter controlled wing." These results provide an indication that aerodynamic-based divergence can exist on wings. A recommendation presented in this work is that a frequency tracking of all modes needs to be performed experimentally. This would show that the still-existing structural dynamic modes are stable, while simultaneously observing the divergent mode.

---

<sup>25</sup> Johnson, R.E., and Fred L. Kiokemeister, *Calculus*

Martin and Watkins<sup>26</sup> present and discuss analytical and experimental data for delta wings. The data presented is of a summary nature. Only the divergence conditions are given; no frequency information is provided. In their discussion of the transonic test data, however, they say, “The divergence dynamic pressures were very sharply defined and were marked by one or two large excursions of the tip of the model just prior to divergence. ... The model motion, when divergence was reached, was quite rapid and the deflection quickly increased until the model was bent beyond 90 degrees to the airflow.” Their comments lead to speculation regarding the nature of the divergence mechanism that they observed.

---

<sup>26</sup> D. J. Martin and C. E. Watkins, *Transonic and Supersonic Divergence Characteristics of Low-aspect-ratio Wings and Controls*.

## CHAPTER TWO

### ANALYSIS

A standard procedure for solving a structural dynamic problem is to employ eigenanalysis to calculate the structural dynamic eigenvalues and eigenmodes. Recently, this eigenvalue/eigenmode procedure has been extended to unsteady aerodynamics, and to coupled aeroelastic equations<sup>1</sup>.

In computational fluid dynamics, CFD, there are two approximations that are typically employed. One is the construction of a computational grid, which determines the limits of spatial resolution of the computational model. The second is the approximation of an infinite fluid domain by a finite domain. It is a principal purpose of the present discussion to demonstrate that the computational grid not only determines the spatial resolution obtainable by the CFD model, but also the frequency or temporal resolution that can be obtained. Also, as will be shown, the finiteness of the computational domain determines the resolution of the eigenvalue distribution for a CFD model. Both of these observations have important ramifications for assessing the CFD model and its ability to provide an adequate approximation to the original fluid model on which it is founded. To these ends, a finite-wake, time-domain, discretized vortex lattice aerodynamic model has been utilized.

Results of aerodynamic parametric variations are presented, as well as detailed discussion of the trends produced by these systematic variations. The discussion includes the parametric effects on both the discrete- and continuous-time aerodynamic eigenvalues. These studies give insights into aerodynamic modeling in the discrete time domain including how one may construct reduced order aerodynamic models using the dominant aerodynamic modes.

The aerodynamic model was also combined with time-domain discretized structural dynamic equations to examine the aeroelastic behavior of a typical section. Aeroelastic response is also discussed in terms of eigenanalysis results. Aeroelastic stability analyses generally focus on the migration of the eigenvalues as a function of the velocity or other flow parameter. Indeed, much flutter analysis in practice today uses at best only an approximation to the true aeroelastic eigenvalues. Here, the true eigenvalues are found for all aeroelastic modes without iteration. This enables an examination of the subcritical modal characteristics of the system as well as the behavior the noncritical modes at instability.

---

<sup>1</sup> Dowell, Earl H., Kenneth C. Hall, and Michael C. Romanowski, *Eigenmode Analysis in Unsteady Aerodynamics: Reduced Order Models*; Hall, Kenneth C., *Eigenanalysis of Unsteady Flows about Airfoils, Cascades and Wings*.

The eigenvalue migration is observed and the eigenvectors are investigated to determine the relative participation of the aerodynamics and the structural dynamics. Nondimensional parametric variations were performed to investigate the changing character in the dynamic modes as the system diverges. Using this database, configurations were identified and analyzed which exhibited different types of dynamic mode behavior as the typical section became statically unstable. Specific emphasis is paid to configurations where the dynamic mode persists at a nonzero frequency as the system destabilizes.

The eigenvectors associated with the dynamic and divergent modes are also studied. They provide a wealth of information and can supplant or supplement the eigenvalues in providing stability information. They are studied from the standpoint of their own modal content as well as their phase relationship to other eigenvectors of the system. They are utilized to identify the relative importance of the structure and the aerodynamics in a given aeroelastic mode's behavior.

### *Aerodynamic Studies*

#### Aerodynamic Modeling

A Vortex Lattice solution to Laplace's equation for incompressible two-dimensional flow is utilized in this study. The flow over an airfoil with a certain number of vortex elements on the airfoil and in the wake is now considered. The airfoil is modeled as a two-dimensional flat plate. The airfoil and the wake are divided into segments, referred to as aerodynamic elements. Vortex lattice aerodynamics are generated by placing vortices of strengths to be determined at points on the airfoil and in the wake. Collocation or control points, usually located aft of the vortex locations, are points where the boundary conditions must be satisfied. Typical placement is for the vortices to be located at the  $1/4$ -chord points of the aerodynamic elements. The collocation points are typically placed at the  $3/4$ -chord locations of the elements.

The governing equations are presented by Hall<sup>2</sup> and shown in detail in Appendix A; they are briefly summarized here. There are 3 basic relationships, described in the following paragraph, which are combined to form a matrix equation for the vortex strength, Equation 1, where  $n$  and  $n+1$  denote the next and the current discrete time sample.  $\Gamma$  is a vector of vorticities and  $w$  is a vector of downwashes at each of the collocation points. The number of elements on the wing is denoted  $M$ , while the total number of elements is denoted  $N$ .

$$[A]\{\Gamma\}^{n+1} + [B]\{\Gamma\}^n = \{w\}^{n+1} \quad \text{Equation 1}$$

---

<sup>2</sup> Hall, Kenneth C., *Eigenanalysis of Unsteady Flows about Airfoils, Cascades and Wings*.

Three basic relationships determine the contents of the A and B matrices seen in Equation 1. These represent N equations with N variables. The first of the three basic relationships equates the velocity induced by the discrete vortices at the collocation points to the downwash caused by the airfoil's motion. This relationship accounts for M rows within the matrices where M is the number of spatial grid points on the airfoil or wing. Applying Kelvin's theorem generates a second basic relationship utilized in deriving the matrix equations. Unsteady vorticity is shed into the wake; its strength is proportional to the time rate of change of circulation about the airfoil. The time step is taken to be equal to the time it takes the vorticity to convect from one vortex station to the next. This relationship accounts for the (M+1) row of the matrix equations. Once the vorticity has been shed into the wake, it is convected in the wake at the freestream velocity. This is the third basic relationship which appears in Equation 1 as rows (M+2) through (N-1). Vorticity convection also provides the final, Nth, row of the matrix equations. Because the wake is modeled with a finite length, the last vortex element must be treated specially. "Otherwise, the starting vortex would disappear abruptly when it reached the end of the computational wake, producing a discontinuous change in the induced wash at the airfoil. To alleviate this difficulty, ... the vorticity is allowed to dissipate smoothly by using a relaxation factor." <sup>2</sup>

The formulation and analysis of the aerodynamic model progresses in the following manner. Discrete, time-marching equations are written as shown in Equation 1. Once these equations are written, they inherently contain the approximations of the finite wake and the discretization. A discrete Fourier transformation is performed on the unforced equations, producing the z-plane representation, Equation 2.

$$z\Gamma_0 = (-A^{-1}B)\Gamma_0 \quad \text{Equation 2}$$

The discrete time eigenvalues,  $z$ , and the eigenvectors,  $\Gamma_0$ , are extracted from these equations. These provide insight into the behavior of the aerodynamic model and also provide a method for constructing a reduced order model. These eigenvalues are then converted to the continuous time domain,  $\lambda$ -plane, through a zero order hold transformation, Equation 3.

$$\lambda = \frac{\log(z)}{\Delta t} \quad \text{Equation 3}$$

## Baseline Configuration

As the first of several numerical examples, the flow over an airfoil with 20 vortex elements on the airfoil and 180 elements in the wake, equally spaced, is now considered. This will be referred to as the baseline case. The (finite) length of the wake thus extends 9 chord lengths. The eigenvalues and eigenmodes of the flow can be computed by established methods. Because there are 200 elements in the model, 200 eigenvalues result.

The discrete time (z-plane) eigenvalues, extracted from Equation 2, approximately form a circle centered at the origin, as shown in Figure 1. In addition to these eigenvalues, there are a finite number of eigenvalues at the origin. The number of eigenvalues at the origin is equal to the number of segments or grid points on the wing. This conclusion follows from examining the rank of the system matrices in equation 1, from the numerical results obtained here, and appears to be supported by the results presented in Hall<sup>2</sup>, though it was not noted in this previous work. Eigenvalues at the origin in the discrete time domain transform to  $-\infty$  in the continuous time domain.

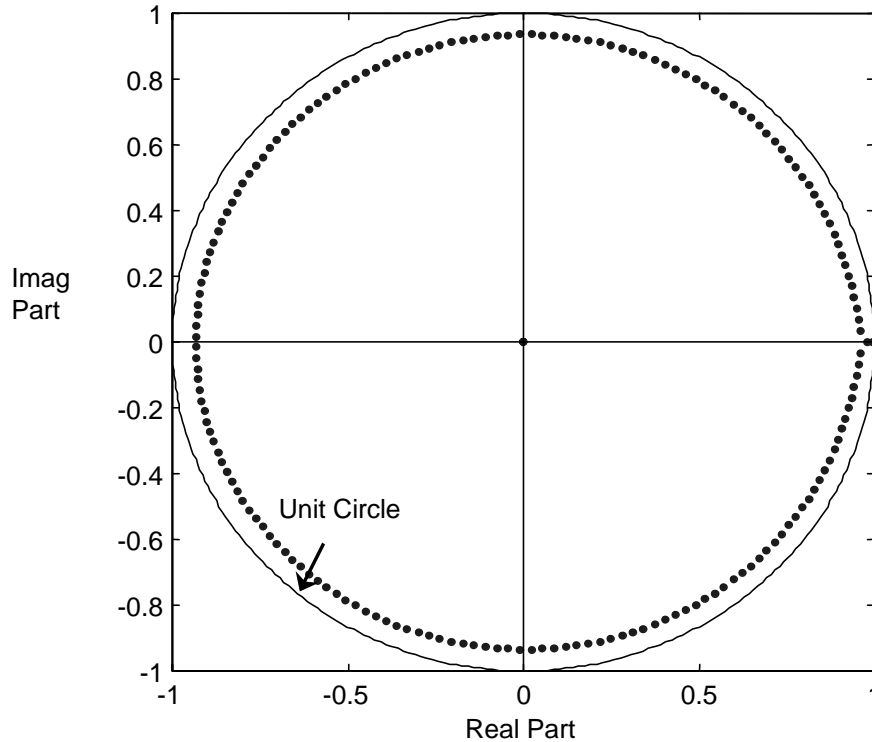


**Figure 1** Eigenvalues for baseline case; discrete time eigenvalues,  $z$

The continuous time eigenvalue distribution for the baseline case is shown in Figure 2. The real part of the eigenvalue is indicative of the damping and the imaginary part is the damped frequency of each fluid eigenmode. Examining the eigenvalues of the aerodynamic matrix in the continuous domain produces several observations. The continuous domain eigenvalues are discretely spaced and are arranged in “arms” that emanate from the origin and reach up and down in the left half plane. Additionally, the real parts of the arms asymptotically approach a limiting value.

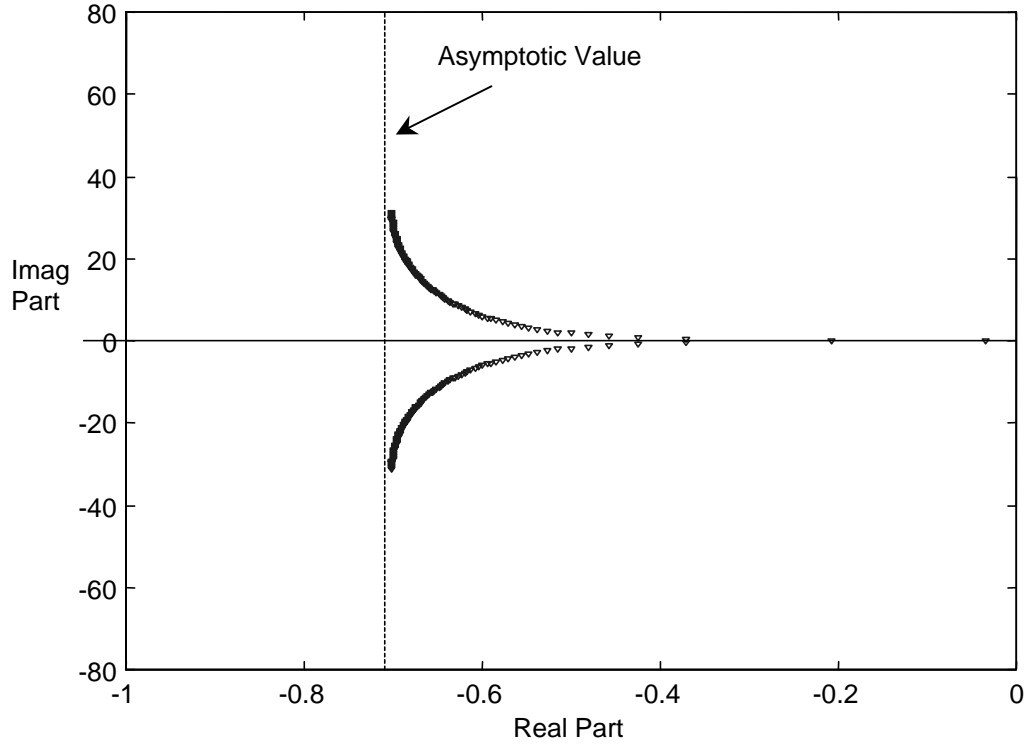


**Figure 2** Eigenvalues for baseline case; continuous time eigenvalues,  $\lambda$

The presence of positive aerodynamic damping is evidenced by the arms lying in the left half plane. The primary contribution to the damping appears to lie with the overall flow field, however, there is additional damping due to the presence of a vorticity relaxation factor at the last wake element. The relaxation factor used in the vortex lattice model provides energy dissipation in the wake; as the relaxation factor is decreased, more energy is dissipated and the aerodynamic damping increases. If the number of aerodynamic boxes within the wake is increased, the last box will be a smaller percentage of the total wake length and thus, the influence of the relaxation factor will be diminished.



## Parametric Variations

Three aspects of the aerodynamic modeling significantly impact the eigenvalue distribution: the size of the aerodynamic elements, the number of these elements that lie in the wake, and the length of the wake. The three aerodynamic configurations, detailed in Table 1, compared against each other two at a time, produce the three comparison cases, which are organized in Table 2 and discussed next.

Aero Config No.	Airfoil			Wake		
	No. of elements	Normalized element size	Normalized airfoil length	No. of elements	Normalized element size	Normlized wake length
1 (Baseline)	20	1	1	180	1	1
2	20	1	1	360	1	2
3	40	$\frac{1}{2}$	1	360	$\frac{1}{2}$	1

**Table 1 Aerodynamic Configurations**

Comparison Case No.	Aerodynamic Configurations Compared			Parametric Variation	Quantity Held Constant
	1	2	3		
I		x	x	Size of aerodynamic elements in wake	Number of aerodynamic elements in wake
II	x	x		Number of aerodynamic elements in wake	Size of aerodynamic elements in wake
III	x		x	Size and number of elements in wake	Length of wake

**Table 2 Comparison Cases for Parametric Variations**

The three comparison cases are discussed in terms of their discrete time eigenvalue distributions (z-values), their discrete-to-continuous time domain transformations (z-transformations) and their continuous time eigenvalue distributions ( $\lambda$ -values).

Comparison case I compares aerodynamic configurations 2 and 3, examining the effects of varying the size of the aerodynamic elements while maintaining the number of elements which lie in the wake. Because the number of wake elements remains fixed, configuration #2 has a wake that is twice the length of the wake in configuration #3 and elements which are twice as large. Although not shown, the discrete time eigenvalue patterns for configurations 2 and 3 are identical because the number of elements in each wake is identical. However, changing the size of the aerodynamic elements changes the transformation, which must be applied to convert the discrete time system to continuous time. This difference in transformation produces the change in continuous domain eigenvalues, as illustrated in Figure 3.

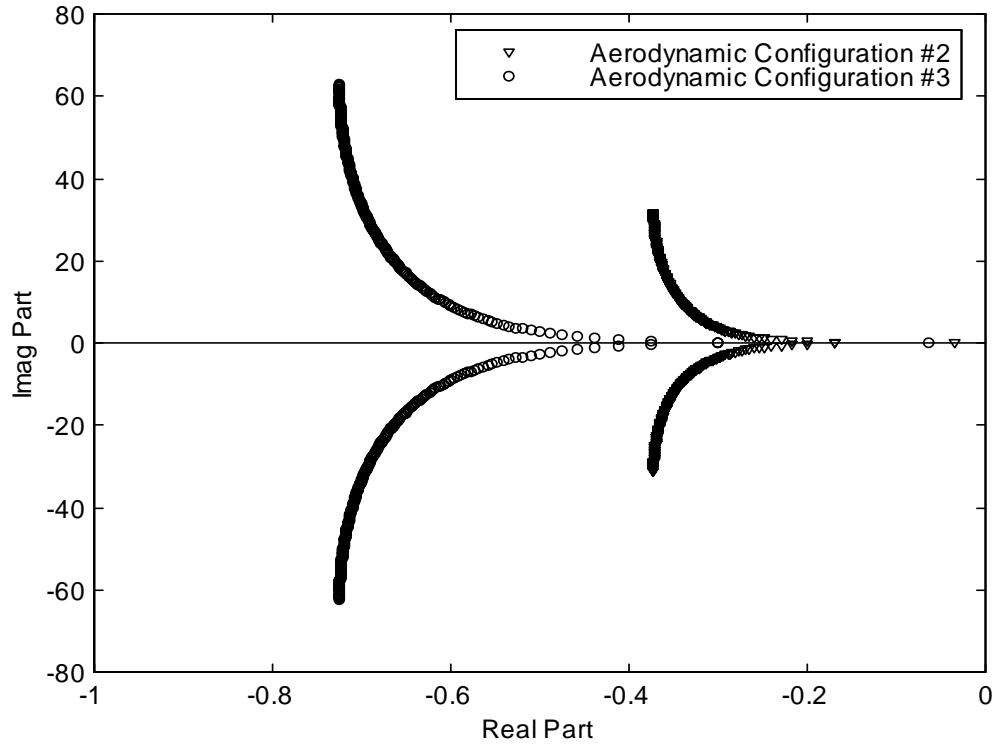


**Figure 3 Case I: Influence of varying the size of the aerodynamic elements. Continuous time eigenvalues,  $\lambda$**

It is easily shown that the frequency of each eigenvalue scales linearly with the aerodynamic element size. The maximum frequency of the arms can be determined a priori by utilizing Shannon's sampling theorem. The aerodynamic eigenfrequencies are bounded from discrete time considerations similar to those that predetermine the discrete Fourier transform frequencies<sup>3</sup>. The maximum frequency,  $\omega$ , that can be resolved would have 1 cycle spanning two aerodynamic panels. Using the velocity to relate the spatial and temporal sample sizes, Equation 4, leads to maximum frequency that can be resolved, Equation 5.

$$U = \frac{\Delta x}{\Delta t} \quad \text{Equation 4}$$

$$\max(\omega) = \frac{\pi U}{\Delta x} \quad \text{Equation 5}$$

<sup>3</sup> Hardin, J.C., *Introduction to Time Series Analysis*.

Thus, changing the aerodynamic element size changes the frequencies of the aerodynamic eigenvalues. As the size of the elements becomes infinitesimal, it is speculated that the eigenvalue arms will cover the frequency range from  $\pm\infty$ .

It should be noted in studying Case I that the number of eigenvalues has remained constant in going from configuration 2 to configuration 3, while the frequency range has doubled. Thus, the density of the eigenvalues has halved. The implications of this will be further discussed in studying Case III.

Comparison case II compares aerodynamic configurations 1 and 2 and examines the effect of varying the number of aerodynamic elements in the wake while holding their size constant. The number of aerodynamic elements in the wake determines the number of discrete time eigenvalues comprising the pseudo-circular pattern. As more elements are placed in the wake, the more crowded pattern expands outward towards the unit circle and the damping of each aerodynamic mode. As the element size decreases, the radius of the pseudo-circular pattern asymptotically approaches 1. In discrete time eigenvalue analysis, an eigenvalue lying on the unit circle represents a neutrally stable system. In the continuous time domain, the imaginary axis is the line of demarcation for stability. It is thus anticipated that the additional boxes in the wake force the “arms” of the continuous time eigenvalues closer to the imaginary axis. Figure 4 bears this out. As more elements are added to the wake, the closer the aerodynamic roots get to those associated with simple harmonic motion. Thus, changing the number of aerodynamic elements in the wake changes the damping of the aerodynamic eigenvalues. As the number of elements goes to infinity, it is speculated that the arms will move to the imaginary axis.

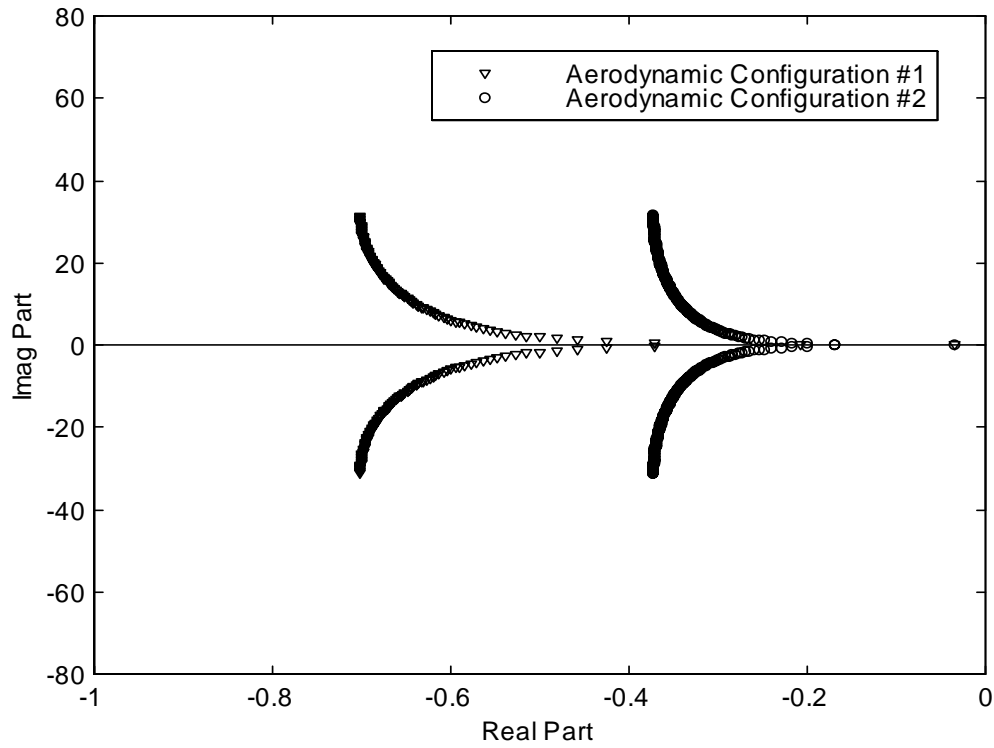


**Figure 4 Case II: Influence of varying the number of aerodynamic elements in the wake.**  
Continuous time eigenvalues,  $\lambda$

It should be noted in studying Case II, as the wake length is increased, leaving the size of the aerodynamic elements constant, the frequency range of the continuous time eigenvalues remains constant. The number of aerodynamic elements determines the maximum frequency. Doubling the number of elements in the wake means doubling the number of eigenvalues on the “arms.” Twice as many eigenvalues reside in arms of the same length. Hence, the continuous time eigenvalue distribution has become denser.

Comparison case III compares aerodynamic configurations 1 and 3 and examines the effects of varying simultaneously and in inverse proportion, the number and length of aerodynamic elements in the wake, such that the wake length remains constant. The expected trends for the behavior of the arms of the continuous time eigenvalues are difficult to predict because, in going from configuration 1 to configuration 3 there are multiple tendencies: increasing the number of elements tends to move the arms closer to the imaginary axis; decreasing element size tends to extend the frequency range of the arms. The combined result on the continuous time eigenvalues, shown in Figure 5, is that the arms of the eigenvalues lie approximately the same distance from the imaginary axis, while the frequency range of configuration 3 is twice that of configuration 1. This corresponds to the effects of smaller element size of configuration 3. Thus, the spacing of the eigenvalues is approximately constant between the two analysis runs.

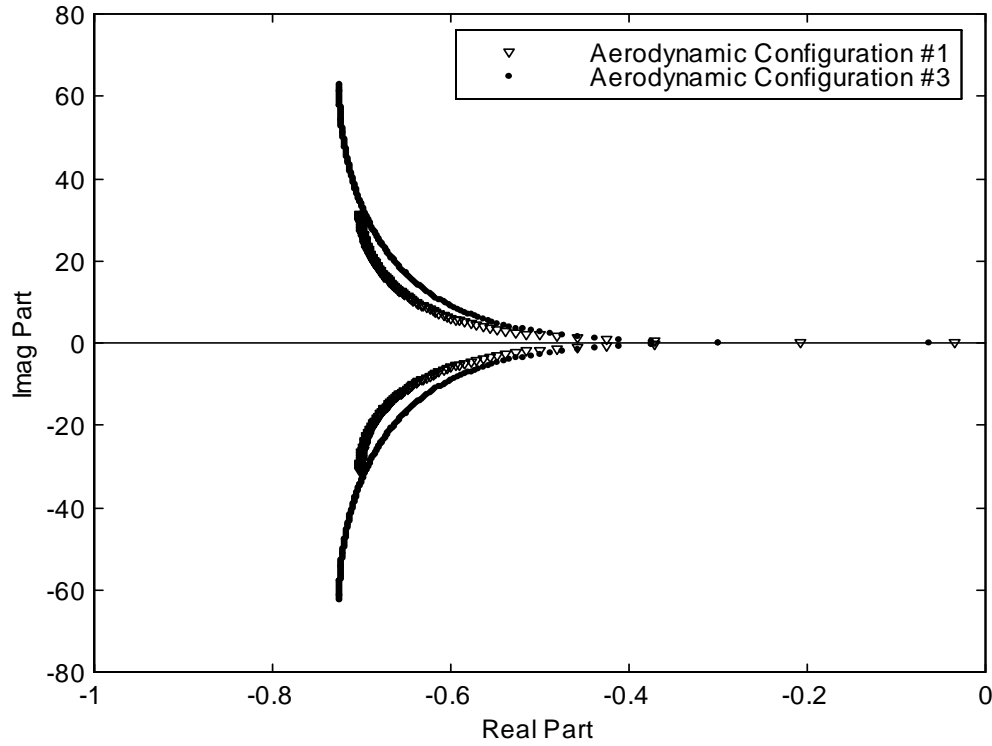


**Figure 5 Case III: Influence of simultaneously varying the size and number of aerodynamic elements in the wake, maintaining a constant wake length. Continuous time eigenvalues,  $\lambda$**

An approximate formula for eigenvalue spacing is derived using the frequency range and the number of eigenvalues. The maximum frequency was found using Equation 5. Accounting for positive and negative values, the frequency range is twice this. Dividing this range by the number of elements or eigenvalues in the wake, and recognizing that the element size times the number of elements in the wake is the wake length produces the relationship given in Equation 6.

$$\Delta\omega = \frac{2\pi U}{L_{wake}} \quad \text{Equation 6}$$

The reader may recognize that this is similar to determination of the discrete Fourier transformation frequencies, as determined by the length of the time record. The eigenvalue spacing is approximate due to the eigenvalues not lying on the imaginary axis, that is, due to the discretization-induced damping. For the case of the element size becoming infinitesimally small, the formula is exact.

Thus, the effect of the finite wake is to produce discretely spaced eigenvalues, instead of a continuous line. As the wake length becomes infinite, it is speculated that the arms of discretely spaced eigenvalues form continuous lines emanating from the origin.

### Discussion of Aerodynamic Studies

The study of aerodynamic eigenvalues using the vortex lattice code has led to some basic insights. The eigenvalues have been shown to be artifacts of the discretization and the finite length wake.

The effects of discretization are controlled by two independent factors. The size of the elements determines the range of frequencies covered by the eigenvalues, while the number of elements in the wake drives the damping. Their effects are shown to be independent, as one controls the transformation from discrete to continuous time, and the other controls the discrete time eigenvalue pattern. The effect of the finite wake is to produce discretely spaced eigenvalues, instead of a continuous line.

The following speculations regarding the limiting cases are offered. As the size of the elements becomes infinitesimal, the eigenvalue arms will cover the frequency range from  $\pm\infty$ . As the number of elements goes to infinity, the arms will move to the imaginary axis. As the wake length becomes infinite, the arms of discretely spaced eigenvalues form continuous lines emanating from the origin.

Aerodynamic eigenvalues have been shown to be artifacts of the discretization, which exist regardless of the airfoil or wing motion applied to the model. The eigenvalues exist even with no airfoil or wing motion. A direct analogy with the feedback control problem can be drawn for aeroelastic systems. The poles of the controller exist, even when the system is open loop. The system is open loop when the feedback path is cut. Three scenarios produce open loop behavior: the sensor information is not provided to the control law, the controller output is not applied to the physical system, or the control law has a zero gain. The last case is analogous to the aeroelastic feedback scenario when the velocity is zero. Just as the poles and zeros of the control law are independent of the feedback gain, the poles or eigenvalues of the aerodynamic system are independent of velocity.

It should be noted that this analogy is not be carried further because standard root locus rules of migration for increasing gain are not directly applicable to the aeroelastic scenario, except with the simplest aerodynamic models. The open loop aerodynamic poles are complicated functions of the velocity, which vary with airspeed.

## Aeroelastic Studies

The discrete time aerodynamic model can be coupled with a discretized structural dynamic model to produce the following time-marching aeroelastic equations of motion, which can then be analyzed to determine the behavior of the system. The vector  $q$  contains the structural dynamic degrees of freedom, the vector  $f$  represents the aerodynamic loads and the matrices,  $D_1$  and  $D_2$  describe the coupling between the aerodynamic and structural dynamic quantities present in an aeroelastic system.

$$D_2 q^{n+1} + D_1 q^n + f^{n+1} = 0 \quad \text{Equation 7}$$

The aerodynamic loads,  $f$ , can be expressed in terms of the unsteady vorticities on the wing,  $\Gamma$ .

$$f^{n+1} = C_2 \Gamma^{n+1} + C_1 \Gamma^n \quad \text{Equation 8}$$

For a system with no external disturbances, the downwash on the airfoil,  $w$ , is produced by the motion on the airfoil.

$$w^n = E q^n \quad \text{Equation 9}$$

Combining Equation 1, 7, 8, and 9 produces the aeroelastic system equations, Equation 10.

$$\begin{bmatrix} D_2 & C_2 \\ -E & A \end{bmatrix} \begin{Bmatrix} q \\ \Gamma \end{Bmatrix}^{n+1} + \begin{bmatrix} D_1 & C_1 \\ 0 & B \end{bmatrix} \begin{Bmatrix} q \\ \Gamma \end{Bmatrix}^n = \begin{Bmatrix} 0 \\ 0 \end{Bmatrix} \quad \text{Equation 10}$$

## The Typical Section

The typical section is a structural and aerodynamic idealization where the motion and the airflow can be represented as two-dimensional. The airfoil section is considered rigid and its permitted motion limited to vertical translation and rotation about a fixed axis. Here, the typical section motion has been further limited to permit only rotation. The boundary condition or mounting system is such that the structural stiffness is represented by a torsional spring. The axis of rotation is termed the elastic axis; its position is measured positive aft from the center of pressure. The geometric parameters are illustrated in Figure 6. The non-dimensional parameters of interest for a single degree-of-freedom typical section are defined in Table 3.

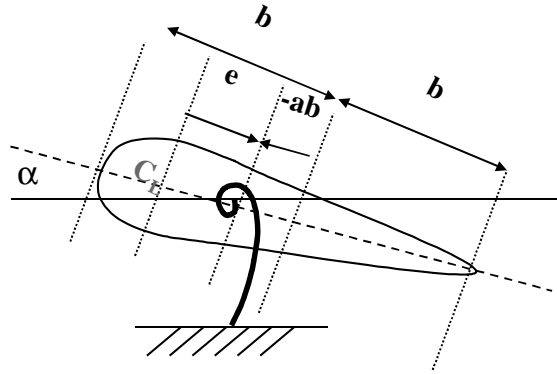


Figure 6 Typical section with pitch freedom

Description	Parameter Symbol	Relationship with dimensional quantities
Torsion mode frequency	$\omega_\alpha$	$\sqrt{K_\alpha / I_\alpha}$
Elastic axis location	$e/b$	$e/b$
Mass ratio	$\mu$	$m / (\text{span } \rho_{\text{air}} b^2)$
Radius of gyration	$r_\alpha$	$\sqrt{I_\alpha / mb^2}$
Reduced velocity	$V$	$U / \omega_\alpha b$

Table 3 Nondimensional parameters of aeroelastic system

Details of the structural dynamic equations are presented in Appendix A. They are represented in generic notation in Equation 7. The generalized coordinate vector,  $q$ , contains only a single degree of freedom, i.e. angle of attack, and its time derivative.

### Stability Analyses

The stability of the aeroelastic system was analyzed by solving the equations of motion for a series of reduced velocities. Eigenanalyses of the discrete time systems were performed on each set of equations and the system eigenvalues tracked. The eigenvalues were transformed into the continuous time domain using a zero order hold



transformation. Stability can be inferred from either the discrete or the continuous time root locus.

A detailed look at the stability analysis for wind tunnel model configuration # 2 is presented. The parameters used in this analysis are summarized in Table 4. This configuration diverges while the dynamic mode that originated as the structural mode persists.

Description	Parameter	Value	Units
Semi-chord	b	4	inches
Span	span	21	inches
Radius of gyration	$r_\alpha$	0.459	
mass ratio	$\mu$	51.42	
torsion mode frequency	$\omega_\alpha$	49.5	radians/second
Elastic axis location	e/b	0.375	
Number of aerodynamic elements on the wing	M	10	
Total aerodynamic elements	N	100	
Density of air	$\rho_{\text{air}}$	0	slinches/inch <sup>3</sup>
Aerodynamic relaxation factor	$\alpha$	0.996	
Size of aerodynamic element	$\Delta x$	0.8	inches

**Table 4 Parameter values used in analysis, wind tunnel model configuration #2**

The discrete time root locus is presented in Figure 7. These z-plane plots show the imaginary part versus the real part of the eigenvalues. The structural-dynamic-originated mode eigenvalue and the aerodynamic-originating eigenvalues, referred to collectively as the aeroelastic eigenvalues, migrate as the reduced velocity is increased. Figure 7 somewhat resembles the plot of the eigenvalues for the uncoupled aerodynamic equations which was presented in Figure 1. The complex aerodynamic-originating eigenvalues appear relatively undisturbed by the coupling with the structural dynamic equations. In addition, the single structural dynamic eigenvalue can be seen near the unit circle, indicating that it is more lightly damped than the aerodynamic eigenvalues. It undergoes substantial movement with the increase in velocity.

An instability occurs when an eigenvalue lies outside the unit circle. For this system, this is observed on the positive real axis. The axes are expanded to more closely examine the behavior near instability, Figure 8. This figure shows the migration of the structural-dynamic-originating eigenvalue, and also the interplay with several aerodynamic eigenvalues. The lowest complex aerodynamic eigenvalue is clearly influenced, as well as the real aerodynamic eigenvalues, one of which becomes unstable. It is difficult to

further study system behavior from these graphs because each velocity produces eigenvalues that essentially belong in different z-planes. This will be discussed in detail in a subsequent section of this paper.

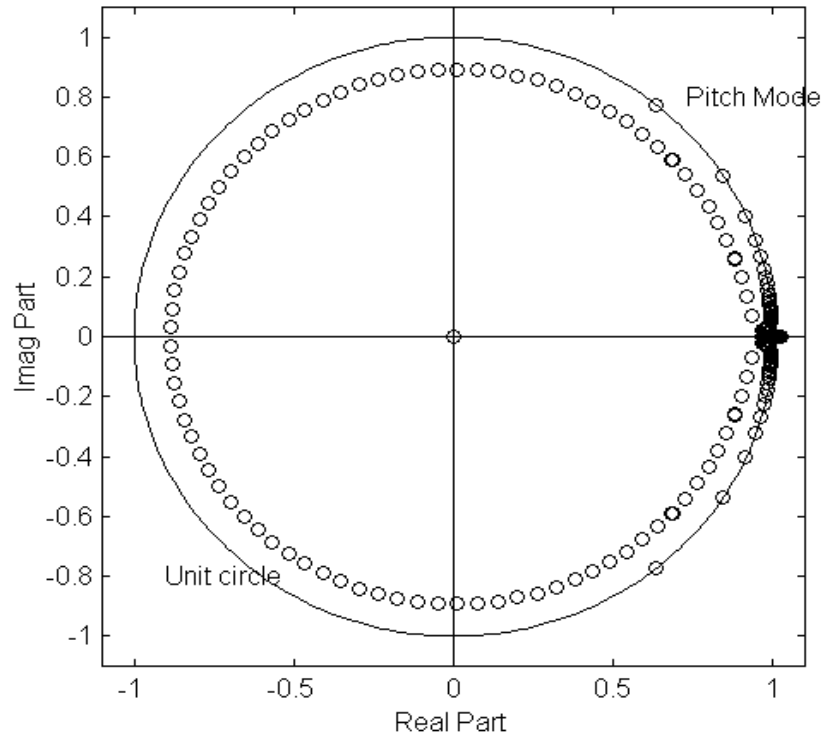


**Figure 7 Discrete time root locus for configuration # 2**

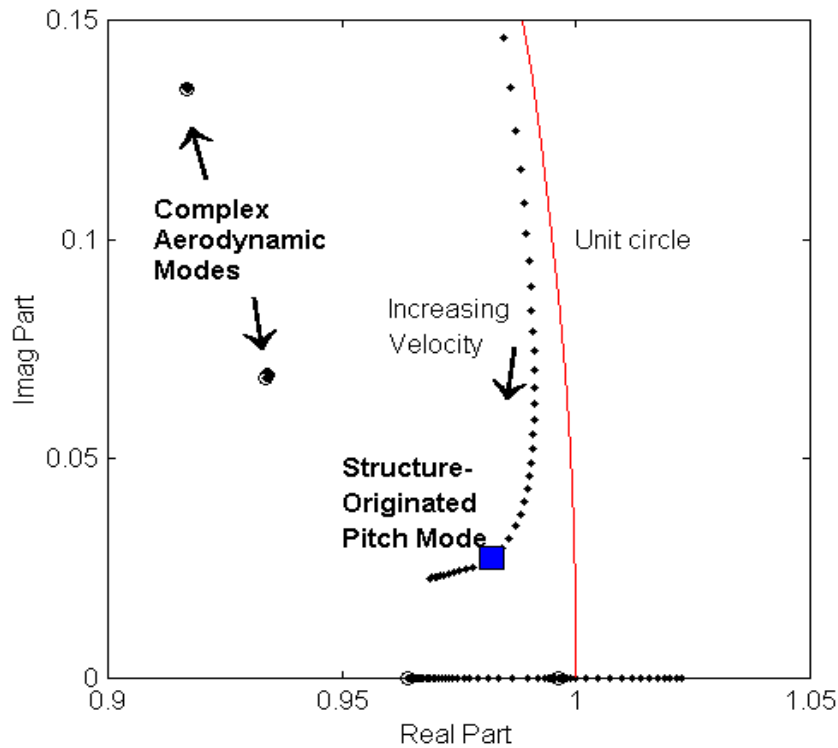


**Figure 8 Discrete time root locus for configuration # 2, expanded scale**

The aeroelastic system is converted to the continuous domain by zero order hold transformations. The behavior of the continuous time domain eigenvalues is shown in Figure 9. For clarity, only the region near the origin is presented. The influence of velocity on the aerodynamic eigenvalues is now evident. As in the aerodynamic case previously discussed where changing the size of the aerodynamic elements changed the transformation from the discrete to continuous time, the same effect is now observed for the aeroelastic case as the time step size is changed. Recall that the aerodynamic parametric studies were conducted at a fixed velocity. The aerodynamic eigenvalue “arms” are stretched with increasing reduced velocity. As velocity increases, the individual complex eigenvalues’ frequencies increase at constant damping.

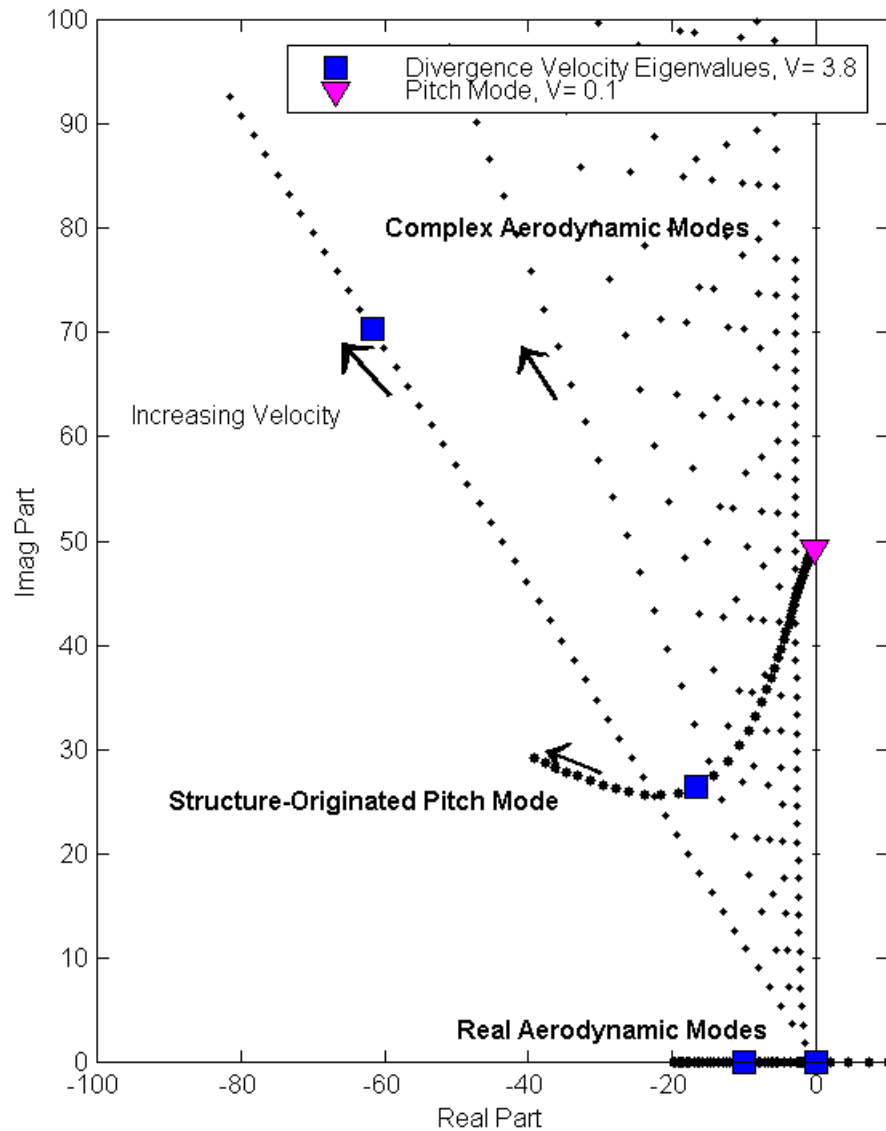


**Figure 9 Continuous time root locus for configuration #2**

Increasing velocity produces a migration in the structural dynamic mode also. The coupled mode that originates as the structural dynamic mode will be referred to here as simply the dynamic mode of the system. This mode is a pure structural mode only at zero airspeed. For any finite velocity, it and all other modes are strictly speaking aeroelastic modes. The lowest reduced velocity for which this system was analyzed was 0.2. The structural dynamic mode for this nearly-zero velocity is indicated by a solid triangle in Figure 9. The root lies at 49.5 rads/second, which agrees with the torsional

natural frequency. It is helpful to simultaneously examine Figure 9 and Figure 10 when interpreting root migration. Figure 10 shows the real and imaginary parts of each eigenvalue plotted versus reduced velocity.

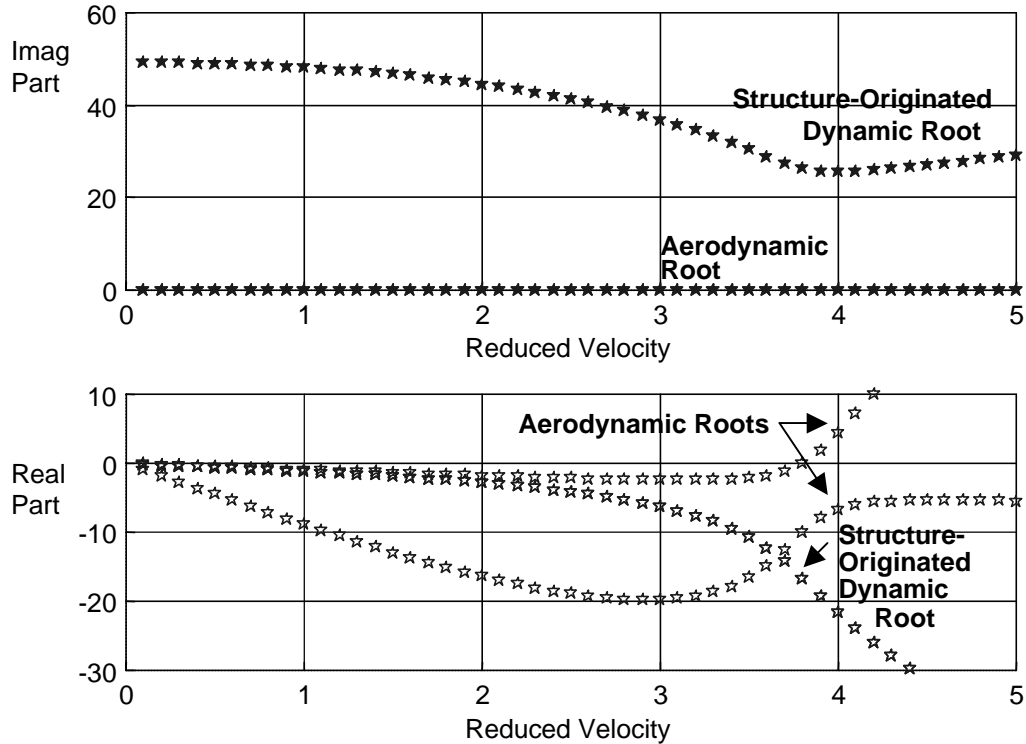


**Figure 10** Continuous time eigenvalues for configuration # 2 as functions of reduced velocity; a) Imaginary part, b) Real part

Increasing velocity produces a larger aerodynamic feedback. This aeroelastic coupling causes the dynamic mode frequency to decrease as velocity increases. This trend holds true until the system becomes unstable. This configuration destabilizes as a zero frequency root, aerodynamic in origin, migrates across the imaginary axis, that is, divergence occurs.

The eigenvalues of the system for the divergence reduced velocity are distinguished in Figure 9 by solid squares. It is apparent that the dynamic mode still exists with a nonzero frequency when the system becomes unstable. At this velocity, the dynamic mode is a coupled structural and aerodynamic mode; the modal content and resultant system behavior will be addressed subsequently.

Attention is now turned back to the aerodynamic roots, focusing on the real axis. The aerodynamic roots which lie on the real axis are of primary concern in the study of divergence. Two real poles originate from the present aerodynamic model. The existence of aerodynamic roots at zero velocity is addressed in the discussion portion of

this paper. For increasing airspeed, both roots initially become more stable. However, at approximately 75% of the divergence reduced velocity, one root changes direction and eventually destabilizes. The real part of the eigenvalues, shown in Figure 10, is indicative of the damping characteristics. The real part of a root that is losing damping will shrink. This indicates that energy is not being dissipated by this mode as effectively as at lower velocity. The real part of the dynamic root is becoming smaller, showing that it is losing its ability to dissipate energy. Once the static root destabilizes, the dynamic root, structural in origin, no longer tends towards instability.

### Modal Characteristics at Divergence: Non-dimensional Parametric Variations

The configuration analyzed above exhibited divergence while the dynamic mode persisted. This behavior is predominant throughout much of the parametric space. This design space will now be explored. Variations in the structural non-dimensional parameters were performed. For each set of parameters, the aeroelastic equations of motion were constructed and eigenvalues found. At the divergence reduced velocity, the modal characteristics can be observed, specifically the frequency and damping of the mode which originated as the structural dynamic mode.

A database of modal characteristics at divergence was generated to identify regions in the parameter space where the divergence mechanism changes from being associated with the structural root versus an aerodynamic root. The parameter variation results were also utilized in the design process for the wind tunnel configurations. The structural dynamic parameters varied in the database are elastic axis location,  $e/b$ , radius of gyration,  $r_\alpha$ , and mass ratio,  $\mu$ .

The natural frequency of the pure structural torsional mode,  $\omega_\alpha$ , was also varied in the initial studies. Changing  $\omega_\alpha$ , however, was found to have no effect on the eigenvalue migration pattern as reduced velocity varied. From steady aerodynamic equations, it can be readily observed that  $\omega_\alpha$  has no direct impact on the reduced velocity of divergence. Thus, the natural frequency is not studied in the parameter variation database.

Varying the three parameters produces a four-dimensional parameter space. Thus, the results can not be shown by a single plot. Sample results are presented here as three-dimensional surface plots. For each surface, one of the parameters is held at a fixed value. Three surfaces are presented showing the ratio of the dynamic mode frequency at divergence normalized by the pure torsion frequency,  $\omega_D/\omega_\alpha$ . Three corresponding surfaces for the damping ratio at divergence,  $\zeta_D$ , are also presented.

The elastic axis position is fixed for the surfaces shown in Figure 11 and Figure 12. Figure 11 presents a surface of frequency of the dynamic mode at divergence, normalized by the air off pitch frequency. The surface shows the variation of the divergence frequency as a simultaneous function of both radius of gyration and mass ratio. The

presented surface is for a nondimensional elastic axis position of 0.375, which corresponds to the wind tunnel model configurations. The solid square on this surface corresponds to wind tunnel configurations 2 and 3. The circle shown on the surface corresponds to wind tunnel model configuration #1, which has a higher radius of gyration. Note that the two wind tunnel model configurations lie in different plateaus of the surface. This difference will be shown to be indicative of a qualitative change in system characteristics. This figure is one slice from the parametric variation design space, here a four-dimensional space. As the elastic axis moves closer to the center of pressure, the surface becomes less smooth. The ridge that is shown in the back left corner of this parametric slice becomes a sudden hill. A trough develops in front of the hill and an additional ridge emerges which runs from low values of mass ratio diagonally across the space to low values of radius of gyration. The front right corner drops to a form a plateau where the frequency ratio becomes zero, or the dynamic mode has become real.

Figure 14 presents the companion surface showing the damping ratio at the divergence condition. The damping information is presented as the angle between the imaginary axis and the eigenvalue. This angle is shown in radians, with a maximum magnitude of the angle of  $\pi/2$  or 1.57 radians.

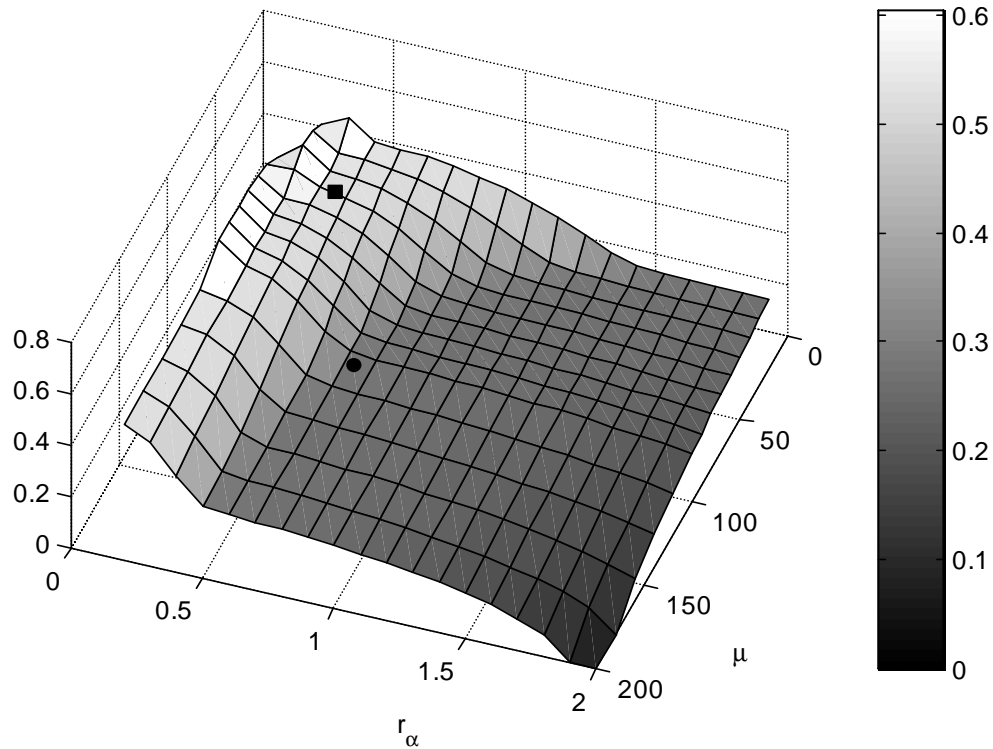


**Figure 11 Surface of  $\omega_D/\omega_\alpha$  as a function of mass ratio and radius of gyration. Elastic axis position is fixed,  $e/b=0.375$ .**

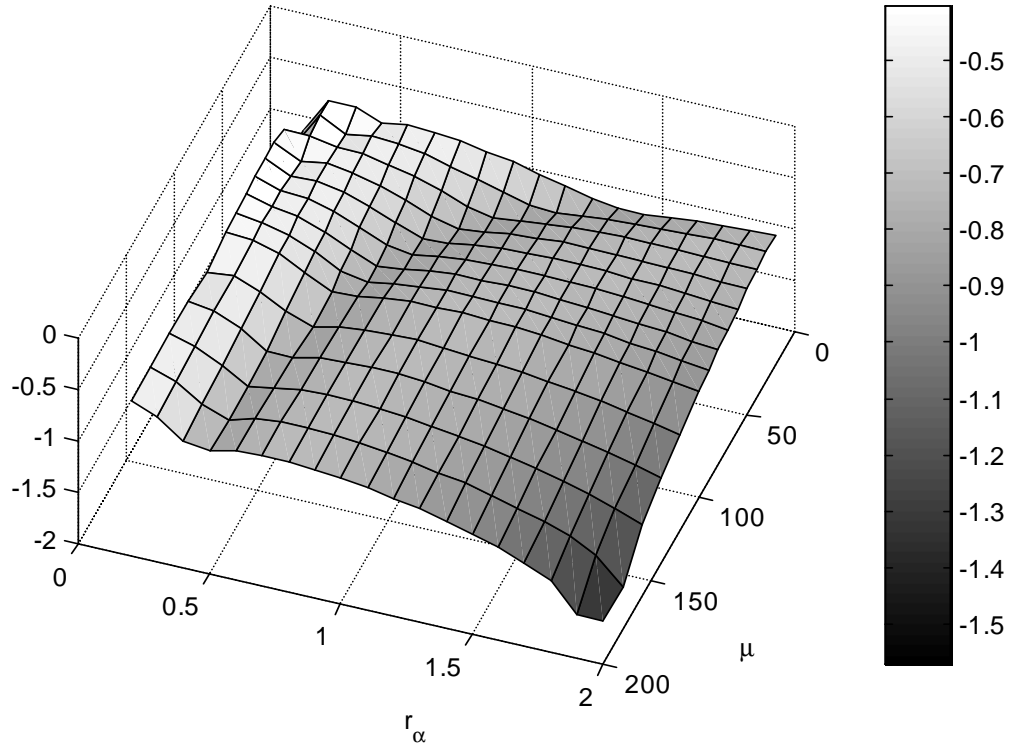


**Figure 12 Surface of  $\zeta_D$  as a function of mass ratio and radius of gyration. Elastic axis position is fixed,  $e/b=0.375$ .**

The radius of gyration is fixed for the surfaces shown in Figure 13 and Figure 14. Figure 13 presents the surface of frequency of the dynamic mode at divergence, normalized by the air off pitch frequency for a radius of gyration of 0.5, which roughly corresponds to the primary wind tunnel model configuration. The surface shows the variation of the divergence frequency as a simultaneous function of mass ratio and elastic axis position. The solid square on this surface corresponds to wind tunnel configurations 2 and 3. Again, this figure is one slice from the parametric variation design cube. As the radius of gyration decreases, the surface becomes overall smoother. As the radius of gyration increases, the trough in the middle of the mass ratio range migrates to lower values and a new trough forms at high values. The new trough at higher mass ratios grows as radius of gyration increases and the overall surface resembles two plateaus connected by a steep grade. The plateau in the frequency ratio surface at high mass ratios has a value of zero, where the dynamic mode has become real. Figure 14 presents the companion surface showing the damping ratio at the divergence condition.



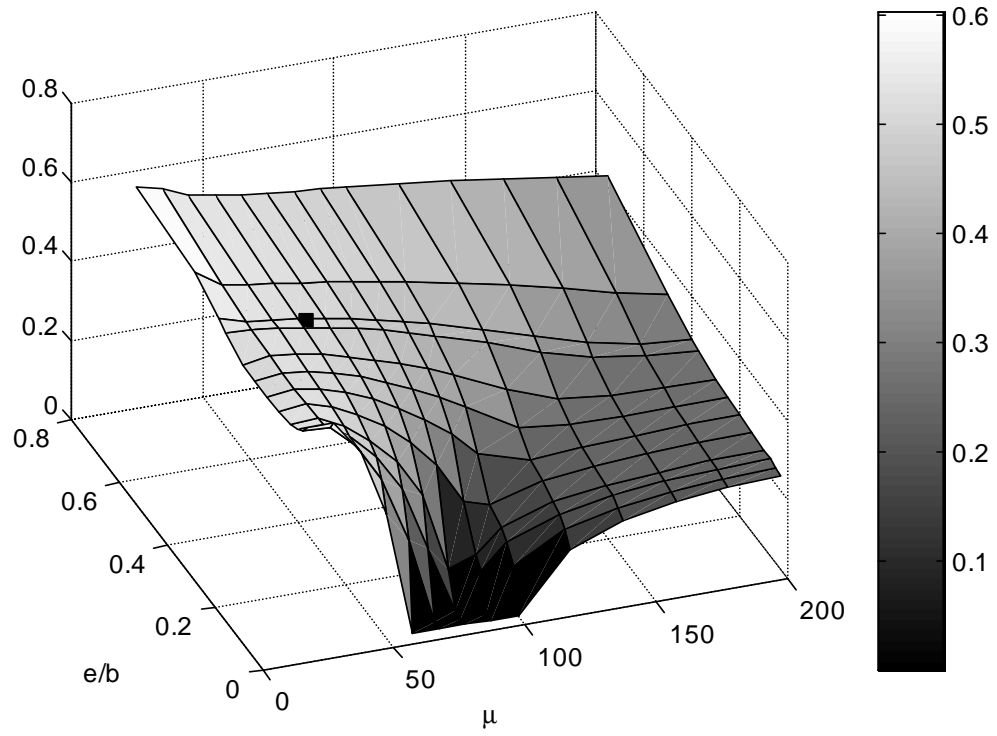


**Figure 13** Surface of  $\omega_D/\omega_\alpha$  as a function of mass ratio and elastic axis position. Radius of gyration is fixed,  $r_\alpha=0.5$ .

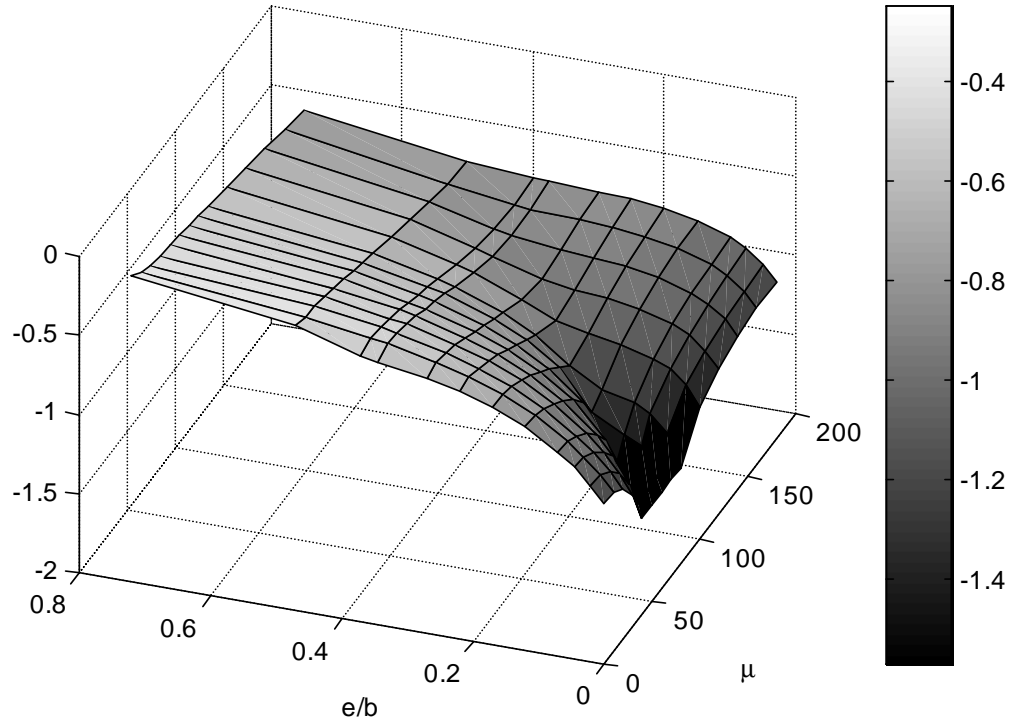


**Figure 14** Surface of  $\zeta_D$  as a function of mass ratio and elastic axis position. Radius of gyration is fixed,  $r_\alpha=0.5$

The mass ratio is fixed for the surfaces shown in Figure 15 and Figure 16. Figure 15 presents the surface of frequency of the dynamic mode at divergence, normalized by the air off pitch frequency for a mass ratio of 50, which roughly corresponds to the wind tunnel model configuration 2. The surface shows the variation of the divergence frequency as a simultaneous function of elastic axis position and radius of gyration. The solid square on this surface corresponds to the wind tunnel configurations 2 and 3. The rolling hills at low values of elastic axis location and the gentle slope into a single plateau at high values of elastic axis location are characteristic throughout the range of mass ratio considered, which was from 20 to 200. Lower values of mass ratio make the hills more dramatic, while higher mass ratios make the valleys sink to zero. Figure 16 presents the companion surface showing the damping ratio at the divergence condition.

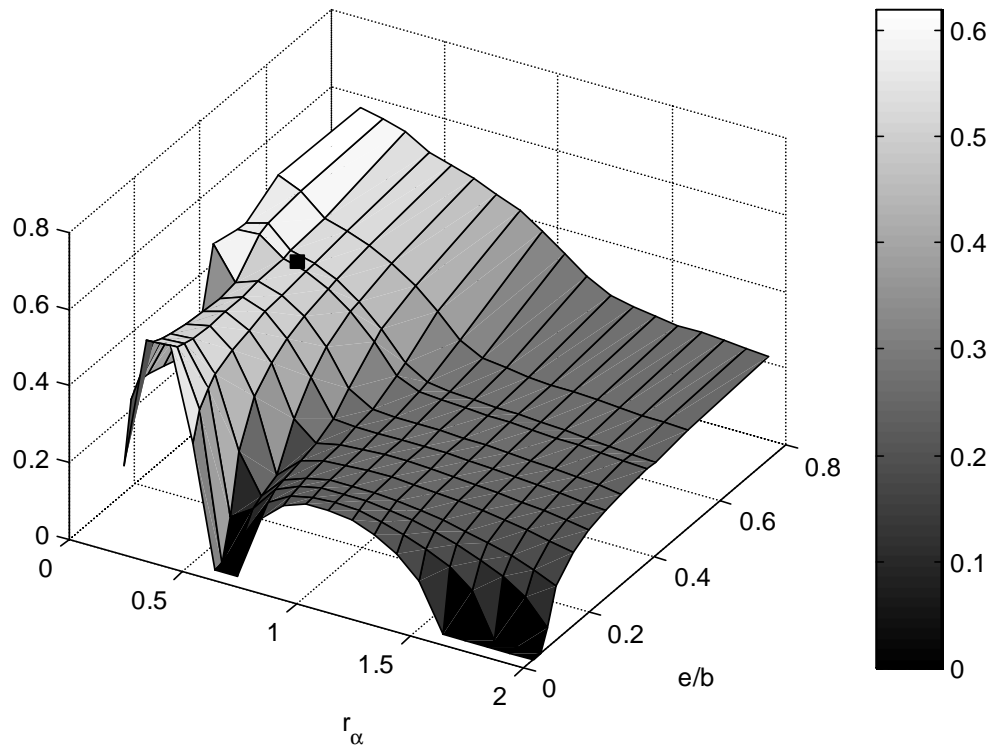


**Figure 15** Surface of  $\omega_D/\omega_\alpha$  as a function of elastic axis position and radius of gyration. Mass ratio is fixed,  $\mu=50$ .

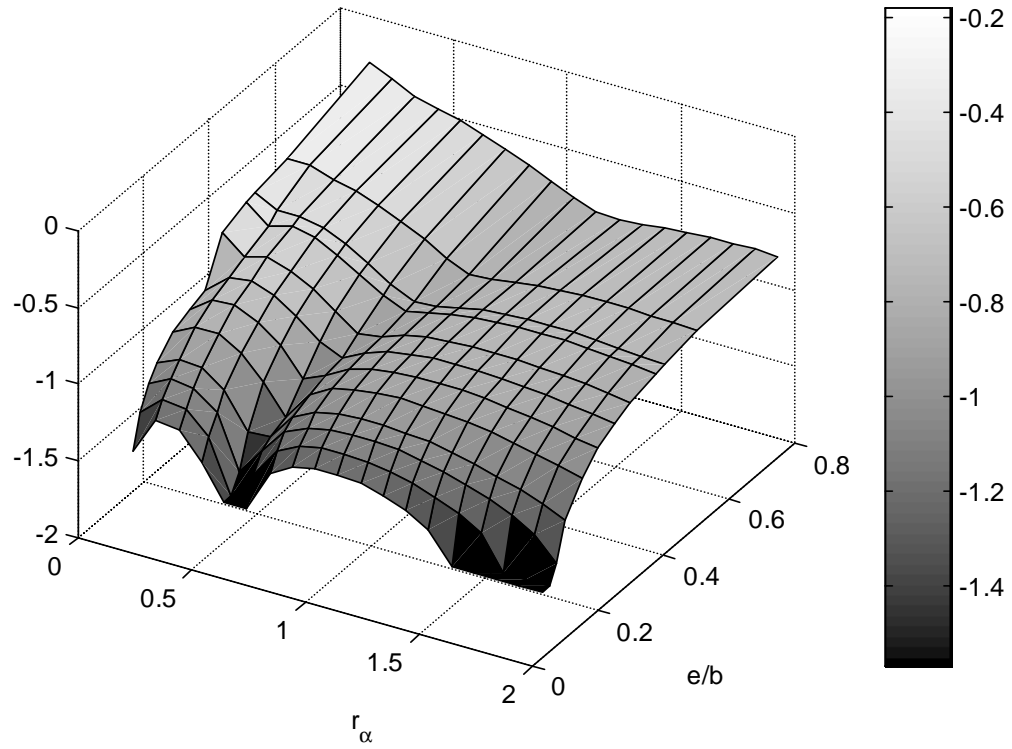


**Figure 16** Surface of  $\zeta_D$  as a function of elastic axis position and radius of gyration. Mass ratio is fixed,  $\mu=50$ .

As seen in the sample parameter surfaces, there are regions where the structural dynamic roots have become real, indicated by the frequency ratio becoming zero. These regions indicate where the divergence mechanism will look like the traditional interpretation of divergent behavior. This information occurs in a relatively small region of the nondimensional parameter space, however. This region is shown in Figure 17.

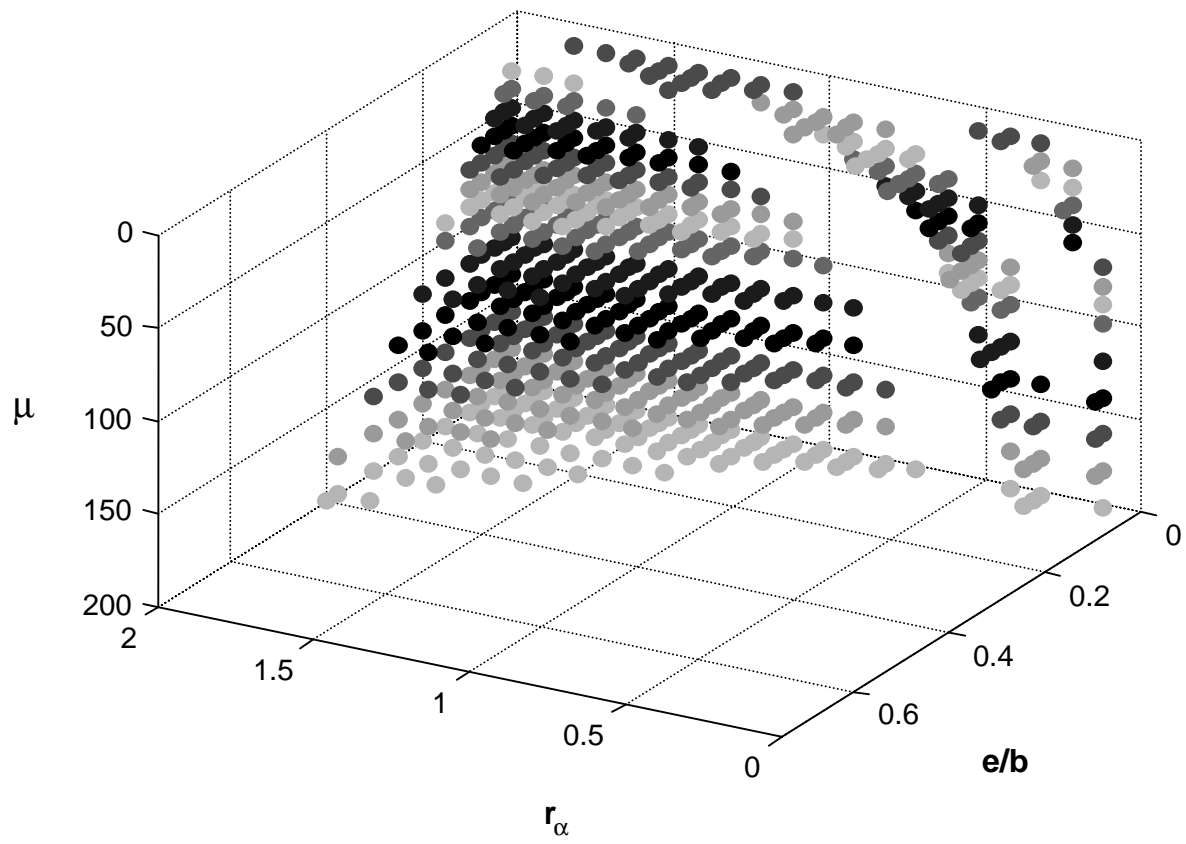


**Figure 17 Non-dimensional parameter space where traditional divergence mechanism occurs**

From the parametric database, many observations can be made. The surfaces of frequency ratio and damping at divergence are neither uniform nor monotonic. However, in general locating the elastic axis just aft of the center of pressure tends to make the typical section diverge in a traditional manner. Large radii of gyration also produce this effect, as do large mass ratios.

The three-dimensional parameter variations reveal that the parameter space is divided into three distinct regions. 1) The structural dynamic root migrates to the real axis as the reduced velocity increases. This mode diverges, as in the traditional interpretation of divergence. 2) A real aerodynamic eigenvalue diverges. The structural dynamic mode still exists as a complex mode at the corresponding reduced velocity. 3) A real aerodynamic root diverges. The structural dynamic root has previously become real, migrated further left along the real axis, becoming more damped, and then becoming complex again prior to divergence.

The wind tunnel model configurations were designed to fall into the second category and demonstrate divergence of a static mode whose origin lies in an aerodynamic root.

Three wind tunnel model configurations will be discussed in this paper. Analytical stability results for what will come to be known as configuration # 2 have already been presented. Each of these configurations diverges as a static mode which originated in the aerodynamic model becomes unstable, while the dynamic mode with its origin in the structural model persists at a non-zero frequency. The structural dynamic parameters for all three configurations are provided in Table 5. For definitions of non-dimensional parameters, see Table 3.

Config #	$I_\alpha$ (slinch- in <sup>2</sup> )	$K_\alpha$ (lb <sub>f</sub> - in/deg)	$\omega_\alpha$ (rads/sec)	$f_\alpha$ (Hz)	$\zeta$	$r_\alpha$	$\mu$
1	0.1147	.90	21.2	3.37	0.0046	0.741	107.9
2	0.021	0.90	49.5	7.88	0.0053	0.459	51.4
3	0.021	2.78	87.1	13.86	0.0035	0.462	50.8

**Table 5 Structural dynamic parameters associated with wind tunnel model configurations**

Configuration #1 has the same torsional stiffness as configuration #2, but the trailing edge segment is made of Tungsten, which substantially increases the pitch inertia. The eigenvalue migration is qualitatively different than that presented for configuration #2. The root locus will be presented shortly. Configuration #3 has the same pitch inertia as configuration #2, but the torsional stiffness was increased. The eigenvalue pattern is identical to that of configuration #2. The change in torsional stiffness manifests itself in

changing the divergence dynamic pressure of the system, but the non-dimensional locus does not change at all.

Table 6 lists the analytical calculations for divergence conditions for the three configurations. Note that the non-dimensional divergence condition is invariant with torsional stiffness. This is shown by the agreement of the reduced velocity for configurations 2 and 3. Also note that the physical divergence condition is invariant with pitch inertia. This is shown by the agreement of the velocity or dynamic pressure for configurations 1 and 2.

Configuration #	Reduced Velocity	Velocity		Dynamic Pressure	
		(in/sec)	(mph)	(psf)	(N/m <sup>2</sup> )
1	8.89	754	42.8	4.6	222
2	3.8	754	42.8	4.6	222
3	3.8	1324	75	14.25	687

**Table 6 Analytical calculation of divergence conditions**

The divergence conditions calculated using the aeroelastic eigenanalysis can be compared to the divergence conditions calculated using the equations of static equilibrium of the system. The equations of static equilibrium for the single degree of freedom typical section can be written by equating the aerodynamic and structural moments which act at the elastic axis, Equation 11. The aerodynamic moment for a symmetric airfoil can be expressed in terms of the lift curve slope and total angle of attack, which is comprised of the rigid angle of attack,  $\alpha_0$ , and the elastic increment,  $\alpha_e$ , Equation 12. The structural restorative moment, Equation 13, is proportional to the elastic increment. Setting them equal and rearranging produces a ratio of elastic increment to rigid angle of attack, Equation 14. For a finite rigid angle of attack, the elastic increment will become infinite, diverge, if the denominator of the right hand side becomes zero. This provides the expression in Equation 15 for calculating the divergence dynamic pressure. Recasting the equation in non-dimensional quantities produces Equation 16.

$$M_A = M_S \quad \text{Equation 11}$$

$$M_A = \bar{q} S e C_{L_\alpha} (\alpha_0 + \alpha_e) \quad \text{Equation 12}$$

$$M_S = K_\alpha \alpha_e \quad \text{Equation 13}$$

$$\frac{\alpha_e}{\alpha_0} = \frac{\bar{q} Se C_{L_\alpha}}{K_\alpha - \bar{q} Se C_{L_\alpha}} \quad \text{Equation 14}$$

$$\bar{q}_D = \frac{K_\alpha}{Se C_{L_\alpha}} \quad \text{Equation 15}$$

$$V_D = r_\alpha \sqrt{\frac{\mu \pi}{e/b C_{L_\alpha}}} \quad \text{Equation 16}$$

The divergence conditions were calculated for the three wind tunnel model configurations, utilizing the parameters listed in Table 5. The results, summarized in Table 7, compare almost exactly with the analytical results shown in Table 6.

Configuration	Divergence Dynamic Pressure (psf)	Divergence Reduced Velocity
1	4.69	8.89
2	4.69	3.80
3	14.49	3.80

**Table 7 Static equilibrium calculations of divergence conditions**

Divergence of an eigenvalue which originates in the aerodynamic model is contrary to the traditional interpretation of system behavior at divergence, although several similar phenomena have been reported by earlier researchers, as discussed in the introduction and background sections of this thesis. The modal content of the instability and the dynamic mode are addressed in the following study of the eigenvectors which provides a deeper insight into the observed phenomena..

### Eigenvector Study

The eigenvectors of the aerodynamic and/or aeroelastic system are now examined in detail. While it is common to examine the eigenvalues for information on system behavior and stability characteristics, it is quite uncommon to attempt to garner insights from the eigenvectors. As noted by Bisplinghoff and Ashley<sup>2</sup>: “(the aeroelastic eigenvalues) have associated with them eigenfunctions when the complex representation is used. Since (the absolute magnitude of eigenfunctions, or eigenvectors) may be



specified arbitrarily, the mode shape is completely defined by the amplitude ratio and a phase angle between ... degrees of freedom. This information has only minor interest in stability studies, and modes are often not even calculated. Their variation with airspeed can throw some light on the physical nature of (the instability), however.”

Determination of the flutter mode shape is the most common use of the eigenvectors resulting from an elastic analysis. The eigenvectors contain a wealth of information that is only hinted at by the eigenvalues. An individual eigenvector can reveal the frequency and damping of the associated eigenvalue. It also provides a ratio of the energy present in the mode due to each component of the state vector. In the case of the eigenmodes analyzed here, an eigenvector provides information on the modal content: whether a mode should be considered as primarily structural, primarily aerodynamic or as a hybrid, aeroelastic mode. The orthogonality or lack of orthogonality among the eigenmodes indicates whether energy can be transferred from one mode to another. This can be important in understanding when, how and why an aeroelastic system destabilizes.

### **Aerodynamic Eigenmodes**

The eigenmodes of the aerodynamic system are considered first. These modes do not change as velocity increases, but it is instructive to know what the modes look like. The aerodynamic eigenmodes contain the modal vorticity for each aerodynamic element. Eight of the eigenmodes are shown in Figure 18. The eigenmodes are presented for an aerodynamic model with 10 elements on the wing and 180 elements in the wake. The modal vorticities are plotted at the chord-wise location of the associated aerodynamic elements.

The first mode, a real mode, resembles a static pressure coefficient distribution over the wing, with little participation from the wake. The second mode is also a real mode resembling a static pressure distribution over the wing. However, this mode contains a large amount of wake participation. The remaining aerodynamic modes are complex and are comprised primarily of an oscillating wake. The wing vorticities are insignificant compared to those in the wake. The modes are ordered by increasing frequency. Each mode contains a single frequency; as the frequency increases or as the mode number is advanced more oscillations are observed in the wake.

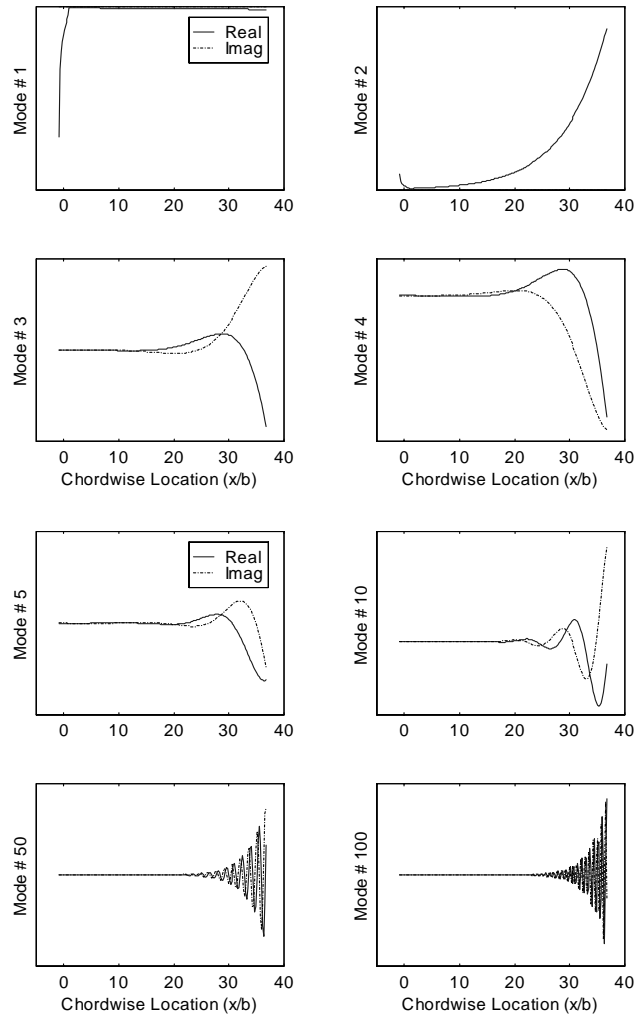


**Figure 18 Selected aerodynamic eigenmodes**

## Aeroelastic Eigenvectors

The aeroelastic eigenvectors are now studied from several perspectives. The first approach taken in examining the aeroelastic eigenvectors is to study the behavior associated with individual modes. Following this, the relationship between two eigenvectors is examined.

In a numerically stiff set of ordinary differential equations<sup>4</sup>, the system behavior is seen to be dominated by the lightly damped and unstable modes. The disparity in the time scales of components of the system allows the overall behavior to be studied by

<sup>4</sup> Kincaid, D.R., and E. W. Cheney, *Numerical Analysis: Mathematics of Scientific Computing*

observing only a few eigenmodes of the system. Thus, in this discussion of system behavior, the modal participation factors associated with only a few modes are examined. Three eigenvectors are considered: 1) the dynamic mode which originates as the structural dynamic mode; 2) the least stable real mode which originates in the aerodynamics and becomes the source of divergence and 3) the second real aerodynamic mode. This information is repeated for reference in Table 8.

<b>Eigenvector Numbering</b>	<b>Real or Complex</b>	<b>Origination</b>
1	Complex	Structural dynamic mode
2	Real	Aerodynamic mode
3	Real	Aerodynamic mode

Table 8 Eigenvector numbering and description

### **Examination of individual eigenvectors**

The first approach taken in examining the aeroelastic eigenvectors is to study the behavior associated with individual modes. The eigenvector associated with a particular eigenvalue can be viewed as the set of modal participation factors for each degree of freedom. Note that the eigenvectors are invariant under the transformation from discrete to continuous time domain. A proof of this is given in Appendix B. The dynamic mode and the destabilizing static mode are examined in detail; the vorticity portion of the eigenvectors is emphasized.

The analysis results presented here are for wind tunnel model configuration #2. The eigenvectors have been normalized to have unity magnitude and phased such that the structural dynamic generalized displacement coordinate,  $\alpha$ , has zero phase.

The dynamic mode near zero velocity is considered first. The modal participation at a low reduced velocity,  $V=0.225$ , is presented for the dynamic mode in Figure 19. At this velocity, the mode is almost a pure structural pitch mode. The associated eigenvalue is identified in the continuous time root locus, Figure 9, by the diamond symbol. The real and imaginary parts of the modal participation are plotted as a functions of chord-wise or downstream position. At this low velocity, the aerodynamics are being driven at the frequency of the structural mode. The portion of the eigenvector associated with the vorticity at each aerodynamic control point, referred to as the vorticity participation, shows that most of the aerodynamic energy associated with this mode is in the wake. The first ten participation factors correspond to elements on the airfoil. Only these vorticities can produce forces on the airfoil. At this velocity, there is very little aerodynamic energy being imparted to the airfoil.

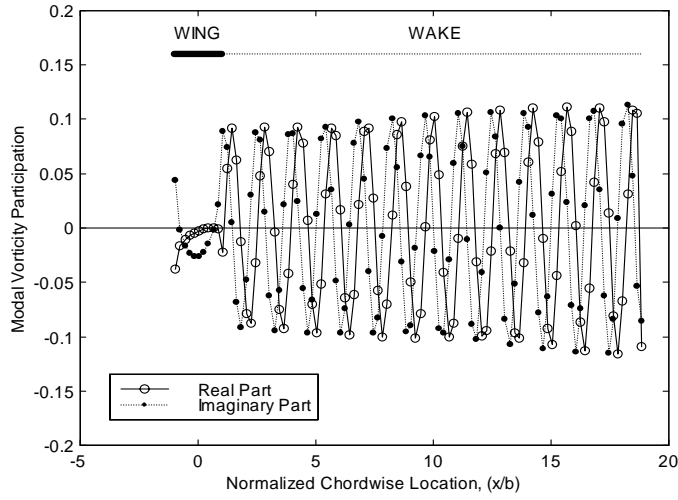


**Figure 19 Eigenvector associated with dynamic mode near zero velocity, associated continuous time eigenvalue  $\lambda = -.16 + j 49.2$**

The wake portion of the vorticity participation appears as a negatively damped sinusoid when viewed spatially. The eigenvector provides a snapshot of the vorticity distribution. Initial examination of the data may lead one to conclude that the system is unstable. In fact, the opposite is indicated. For a stable system, the vorticity being shed from the wing into the wake will decrease as time advances. The vorticity on the last wake element at time  $n$  is the same as the vorticity on the first wake element at time  $n - N_{\text{wake}}$ . Thus, the spatial vorticity distribution could also be thought of as a time history, where time originates at the wake trailing edge and proceeds towards the airfoil.

Near the divergence reduced velocity, the eigenvector associated with the dynamic mode contains significant participation from both the structural dynamic and the aerodynamic states. Figure 20 shows the vorticity participation spatially for a velocity just above divergence,  $V = 3.85$ . The number of oscillations to be expected in the wake,  $N_{\text{cycles}}$ , can be estimated using the frequency of the associated eigenvalue,  $\omega_{\text{mode}}$ , the reduced velocity,  $V$ , and the number of aerodynamic discrete elements in the wake and on the airfoil,  $N_{\text{wake}}$  and  $M$ :

$$N_{\text{cycles}} = \frac{\omega_{\text{mode}} N_{\text{wake}}}{\omega_{\alpha} M \pi V} \quad \text{Equation 17}$$

Using the values for the divergence condition results in a prediction of 0.48 spatial oscillations; the vorticity participation in Figure 20 is consistent with this estimate.

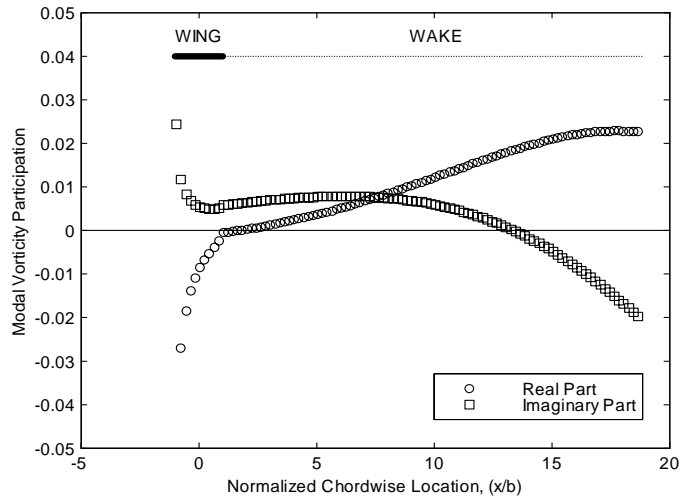


**Figure 20 Eigenvector associated with dynamic mode at the divergence velocity, associated continuous time eigenvalue  $\lambda = -17.7 + j 25.9$**

It is also instructive to view the eigenvectors in terms of the magnitude and phase angle. The vorticity portion of the dynamic mode eigenvector is presented in this format in Figure 21. For 5 values of reduced velocity, listed to the left of each magnitude plot, the magnitude and phase of the eigenvector components are plotted as a function of the chord-wise location of the aerodynamic box. The modal vorticities on the wing are shown by the circles. The wake modal vorticities are shown by dots, which appear as solid lines due to the dense spacing. The last element of the wake has not been shown in these plots- it will be discussed separately.

The magnitude plots show that as the velocity is increased and approaches the divergence speed, more modal energy is contained in the aerodynamic portion of the eigenvector. The divergence reduced velocity for this configuration was calculated as 3.8. The magnitude plots indicate that beyond this velocity, the wing vorticity participation decreases. As previously discussed, the vorticities on the wing determine the importance of the aerodynamic feedback. As velocity increases, the aeroelastic coupling in the dynamic mode increases as evidenced by the growing magnitudes of wing vorticities.

The phase plots also provide much useful information. The dynamic mode eigenvector can be viewed as if the aerodynamics are being forced at the modal frequency. As the airspeed advances, the frequency of the excitation changes. As shown in the cases of the zero airspeed and divergence, the number of cycles expected in the wake can be approximated using Equation 17. The phase information from Figure 21 is summarized in Table 9. The cycles in the wake are estimated and an approximate value of the frequency is calculated. These are shown in the table to compare almost exactly with the imaginary parts of the associated eigenvalues.

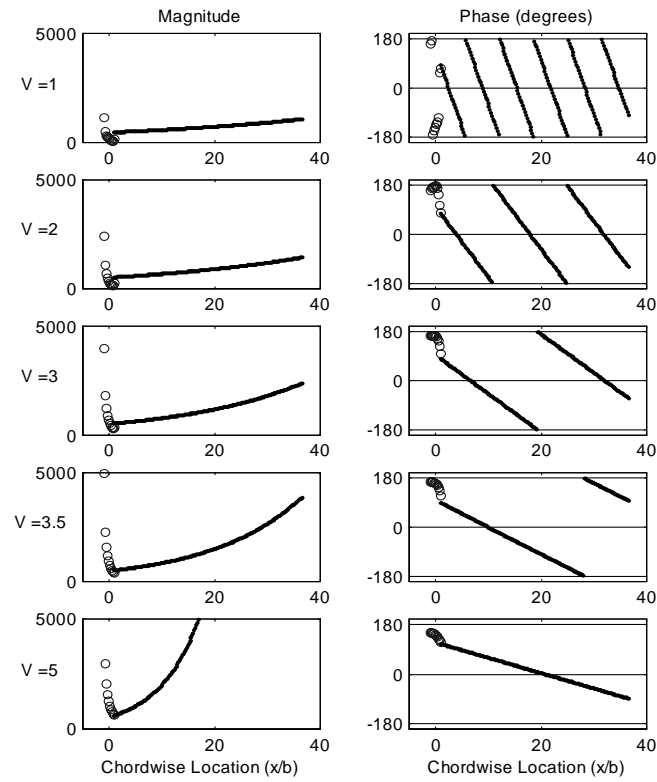


**Figure 21 Vorticity portion of dynamic mode eigenvector for several velocities, magnitude and phase as functions of chord-wise location**

<b>Reduced Velocity</b>	<b>Number of cycles counted in the wake</b>	<b><math>\omega_{\text{mode}}</math> calculated from Equation 17 (rads/sec)</b>	<b><math>\omega_{\text{mode}}</math> from aeroelastic eigenvalue (rads/sec)</b>
1	5.5	48	48.1
2	2.6	45	44.5
3	1.4	36	36.7
3.5	1.0	30	29.9
5	.56	24	24.1

**Table 9 Dynamic mode frequencies estimated from wake portion of dynamic mode eigenvector and calculated from analysis**

The aeroelastic system studied destabilizes as a real eigenvalue moves into the right half plane. The vorticity participation factor associated with this mode resembles a pressure coefficient distribution on the airfoil elements, while the wake contains almost no participation except for the last element. The vorticity participation factor at an example reduced velocity, chosen here to correspond with divergence,  $V = 3.85$ , is presented in Figure 22. As the reduced velocity changes, it is the participation of the last wake element is especially interesting. The magnitude and phase of this element of the eigenvector is plotted versus reduced velocity in Figure 23. Note that these eigenvectors have an overall magnitude of 1. Initially, nearly all of the vorticity participation resides in the last element of the wake. As velocity increases, all of the wake elements begin to participate in the mode. Just prior to divergence, the participation of the last wake element drops sharply. At the divergence velocity, all of the vorticity participation is on the airfoil; the wake factors are zero. As the system moves beyond the divergence velocity, the behavior of all of the vorticity participation factors change. The last wake element quickly becomes influential again, but now with vorticity that is negative, or out of phase, with the airfoil vorticity. As velocity is further increased, the participation of the last wake element smoothly, asymptotically, approaches zero. Also beyond divergence the overall wake vorticity participates.

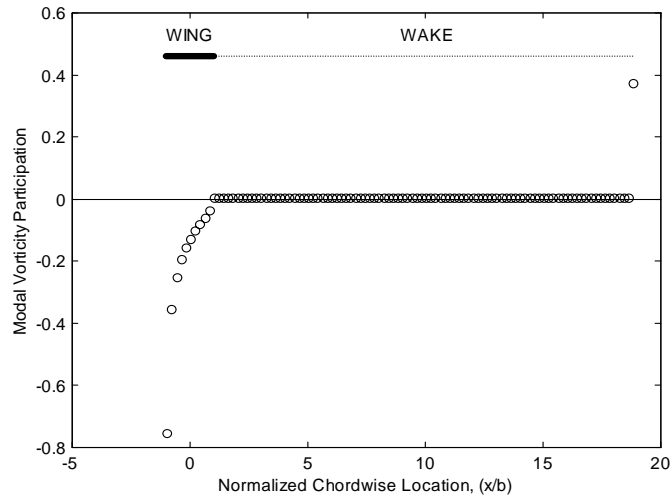


**Figure 22 Eigenvector associated with the unstable static mode just above the divergence velocity**

Transition from stability to instability produces dramatic changes in the associated eigenvector. While the eigenvalue smoothly traverses across the imaginary axis, the character of the vorticity participation changes sharply.

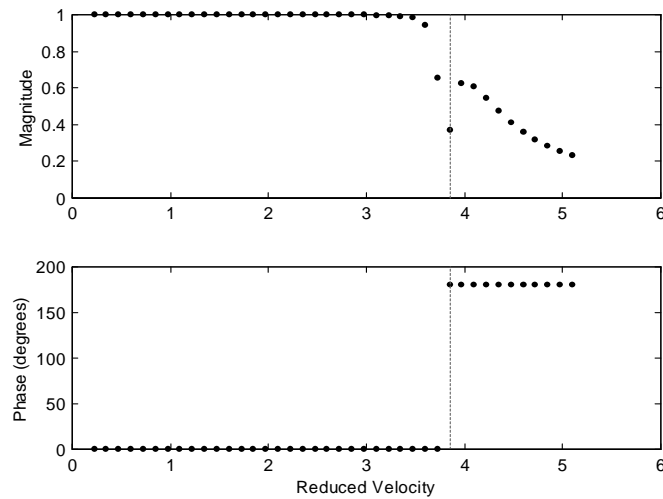


Figure 23 Vorticity participation of last wake element, associated with the real eigenvalue that destabilizes

### Vorticity Ratios as Indicators of Modal Participation

Each of the modes of an aeroelastic system contains structural and aerodynamic participation to varying degrees. This participation changes as the velocity increases and the feedback from the aerodynamics into the structure increases. Furthermore, the structural contributions and the aerodynamic contributions are different for different configurations. As an indicator of the aerodynamic contribution to the dynamic mode and the divergence mode, the modal vorticities on the wing were summed. These sums were normalized by the summation of the wing and wake modal vorticities. This ratio indicates the amount of aerodynamic participation in the mode.

Four configurations are examined in Figure 24. The root loci are shown in the left column. The roots are shown which correspond to the structural dynamic mode, which originates as a complex pair, and also the two real aerodynamic eigenvalues. The zero airspeed values for each of the roots are shown in the plot with open triangles. As the reduced velocity is increased towards the divergence condition, the roots of the system are shown by the dots. The value of each root at the instability dynamic pressure is denoted by a solid triangle. The vorticity ratios are shown in the right column. The vorticity ratios are presented for the dynamic mode which is structural in origin, (mode 1), and the divergent static mode which is aerodynamic in origin, (mode 2), as functions of reduced velocity. The area above each curve represents the energy dissipated into the wake. The area below each curve represents the modal energy imparted to the structure. A higher curve indicates that a larger portion of the modal energy can be attributed to the aerodynamics.



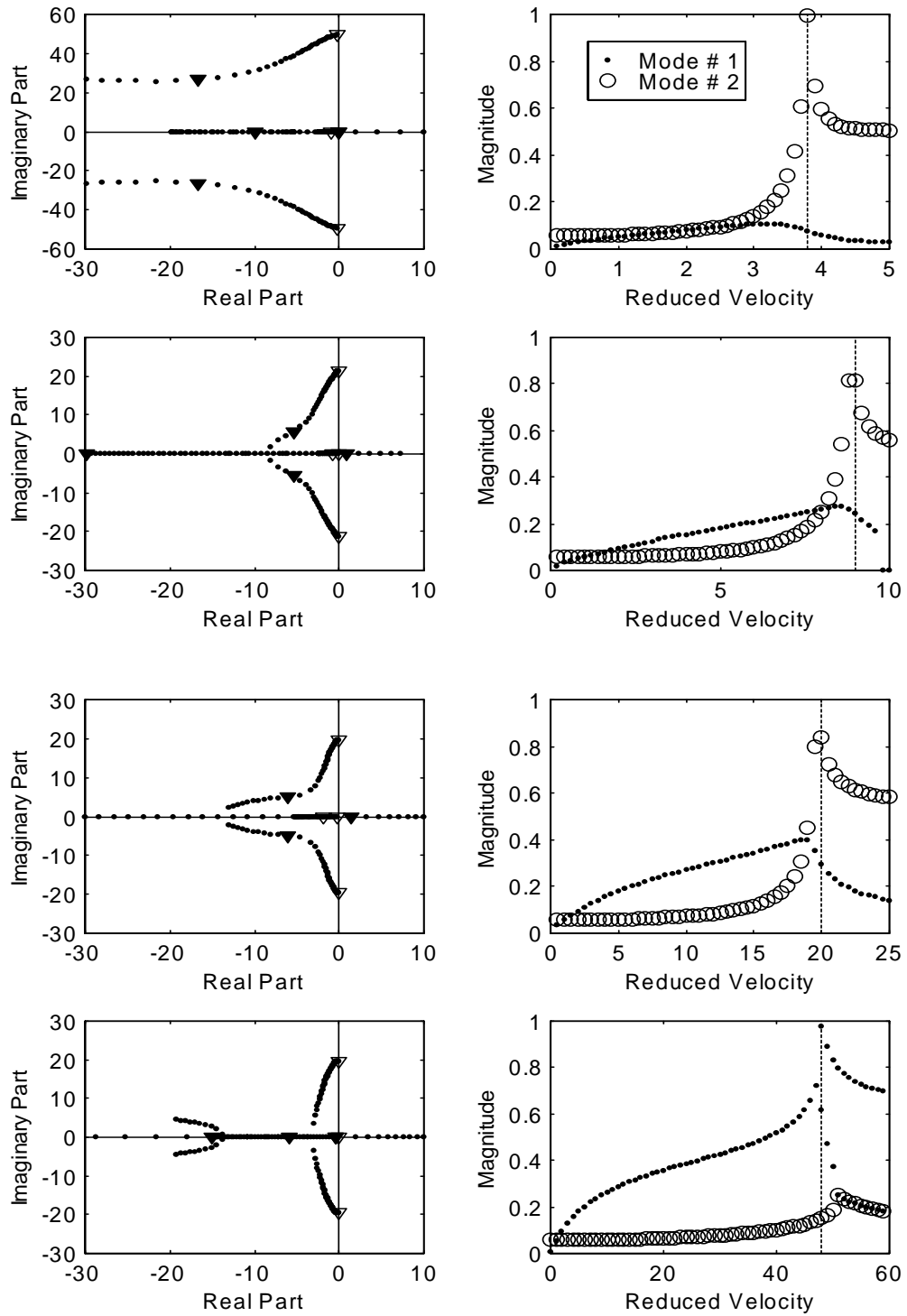


**Figure 24** Root loci and vorticity ratio plots for a) wind tunnel model configuration 2; b) wind tunnel model configuration 1; c) the intermediate configuration and ; d) the traditional divergence configuration

The first configuration is the previously analyzed wind tunnel model configuration #2. The dynamic mode persists for this configuration at divergence. The root locus shows the dynamic mode frequency at greater than half the natural frequency of the air off system. This suggests that the structural influence is a dominant participant in the mode. The vorticity ratio tells a similar story. The dynamic mode's vorticity ratio is shown by the smaller symbols. The aerodynamic contribution to the mode is low throughout the reduced velocity range. Thus, the dynamic mode is primarily a structural dynamic mode. Revisiting the root locus, it can be observed that the primary contribution of the aerodynamics to this mode is a large amount of damping. The vorticity ratio associated with the static divergence mode is also shown. At divergence, the aerodynamic participation is shown to increase dramatically and dominate the mode. Consideration of the root locus and the vorticity ratio indicates that divergence for this configuration is primarily aerodynamic.

The second configuration shown in Figure 24 corresponds to wind tunnel model configuration #1. The frequency of the dynamic eigenvalue has decreased significantly at divergence compared to the previous configuration. The vorticity ratio indicates that the dynamic mode has more aerodynamic participation than the previous configuration. The dynamic mode is still observed to have a nonzero frequency at divergence and be primarily driven by the structural participation. The divergent mode is primarily aerodynamic in nature.

The third configuration shown does not correlate with a constructed wind tunnel model configuration. It is analyzed to show the progression of the aerodynamic participation in the dynamic mode. The vorticity ratio indicates that the dynamic mode has more aerodynamic participation than the previous configurations.

The fourth configuration illustrates the divergence mechanism that is traditionally envisioned. The parameters used in this example do not represent a buildable configuration with known materials, but are presented to show that the analysis methodology is not single-minded. This configuration was generated by modifying the parameters associated with wind tunnel model configuration #1. The elastic axis was moved to  $\frac{1}{4}$  inch aft of the center of pressure. The radius of gyration was then doubled.

Description	Parameter	Value	Units
Semi-chord	b	4.0000	inches
Span	span	21.0000	inches
Radius of gyration	$r_\alpha$	1.6034	
mass ratio	$\mu$	108.0000	
torsion mode frequency	$\omega_\alpha$	19.6000	radians/second
Elastic axis location	e/b	0.0561	
Number of aerodynamic elements on the wing	M	10.0000	
Total aerodynamic elements	N	180.0000	
density of air	$\rho_{\text{air}}$	0.0000	slinches/inch <sup>3</sup>
aerodynamic relaxation factor	$\alpha$	0.9960	
size of aerodynamic element	$\Delta x$	0.8000	inches

**Table 10 Parameter Values for traditionally divergent configuration**

The corresponding root locus, which is presented in the last row of Figure 24, indicates that the structural dynamic originated mode frequency decreases with increasing reduced velocity until they turn from a complex pair of roots into two real roots. Shortly after the pair become real, one root becomes more highly damped and one becomes unstable. As the reduced velocity is increased, the real aerodynamic eigenvalue migrates toward the left, or damped condition. The structural dynamic eigenvalues migrate towards the real axis. As they hit the axis, the complex pair of eigenvalues both become real. One of them becomes more highly damped and the other one becomes unstable.

The non-dimensional parameters used in this last example case can be produced by physical parameters which approach buildability only for semichord values which exceed wind tunnel blockage guidelines. Also, there are a few additional issues regarding the potential for successful fabrication and testing of this configuration. In locating the elastic axis so near the center of pressure, there is very little room for error or change in the fabrication process. The dynamic pressure of the instability is proportional to the inverse of the distance from the center of pressure to the elastic axis. If a 1/16 inch error exists in the location of the pivot axis, the divergence dynamic pressure would be 75% of the anticipated value. A second consideration is the potential for a camber mode to be induced. The airfoil is a 1/32-inch thick aluminum shell. At the trailing edge, a tungsten mass is attached with set screws. Moving the rotational axis forward, which is required to generate the traditional mechanism configuration, means moving the rotational axis away from the supporting, stiffening interior spars and also giving the tungsten a longer moment arm. These factors will make the airfoil section tend to deform in the streamwise direction. All analyses to date have been performed assuming a rigid airfoil. The airfoil section, however, is a closed cell. This means that it is a fairly stiff structure, and the deformation may not be a cause for concern.

## Modal Moment Comparison

The structural and aerodynamic moments can also be calculated by using the eigenvector information. The static structural moments corresponding to each mode were calculated using the static moment equation, Equation 13, and the modal results for angular displacement. The static aerodynamic modal moments are calculated in similar fashion, employing the static aerodynamic equation, Equation 12. The results are compared in Figure 25. In this comparison, the angle of attack component of the dynamically determined eigenvectors was employed. For each velocity, the ratio of the aerodynamic to static moment is a ratio of dynamic pressure to divergence dynamic pressure. This can be shown by comparison of Equation 2 and Equation 3. Subcritically, for each mode, the static structural modal moment is less than the aerodynamic static moment. Thus, each mode has enough structural restorative power to counteract the effect of the aerodynamic moment, and the modes are stable. In the supercritical case, the static mode, labeled mode 2, indicates that the aerodynamic moment is too large for the structure to restore the system to equilibrium. This indicates that the mode is statically unstable, as indicated previously by the eigenvalue analysis.

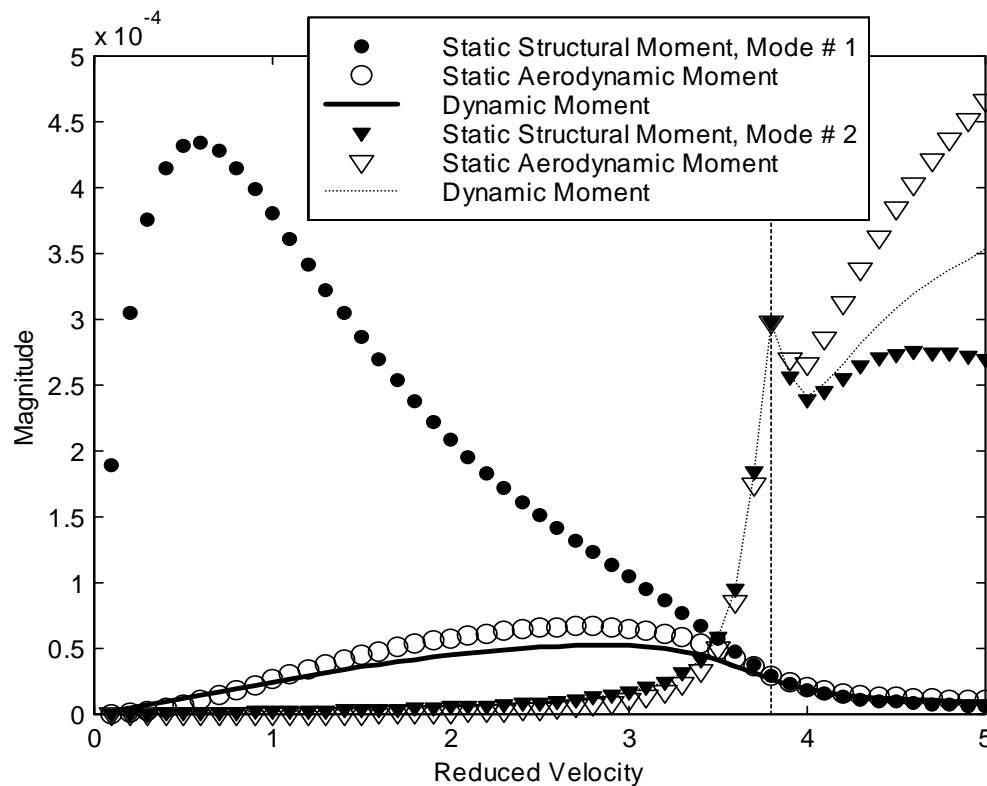


Figure 25 Modal moments, configuration #2

The dynamic modal moments associated with any eigenvector must have equal structural and aerodynamic components as defined in the dynamic equations. This modal quantity is also shown in the figure for both of the modes represented. A difference between the static and dynamic moment is the inclusion of the oscillatory portion of the motion. For the dynamic mode, particularly subcritically, there is a large oscillatory component. This is illustrated by the large difference between the static structural moment for mode 1 and the dynamic moment for the same mode. Another significant difference between the static moment results and the dynamic moment results occurs supercritically. The static equations essentially enforce a neutral stability assumption. Because the static mode, labeled mode 2, is unstable, there is a large difference between the static and dynamic moments.

### Orthogonality between eigenvectors

Comparisons were made between pairs of eigenvectors, employing the techniques demonstrated by Afolabi, Pidaparti and Yang<sup>5</sup>.

The eigenvectors identified in Table 8 were compared, two at a time by finding the phase angle between them. Modes which are in phase, or have 0° separating their orientations, will tend to feed energy into each other and potentially amplify the motion. Modes which are out of phase, or have angles of 180°, will tend to act against each other, canceling out the energy and motion of each other. Orthogonal modes, generally thought to be incapable of exchanging energy from one mode to another, would be at 90° to each other. Near a modal coalescence, a loss of orthogonality could be expected to occur. The angle,  $\theta$ , between the eigenvectors,  $\psi_i$  and  $\psi_j$ , is computed as the inverse cosine of the normalized inner product.

$$\theta_{i,j} = \cos^{-1} \left( \frac{\psi_i \bullet \psi_j}{\|\psi_i\| \|\psi_j\|} \right) \quad \text{Equation 18}$$

For complex modes, inner product is seldom real, resulting in an inability to compute the arccosine. This difficulty is avoided by employing “realification” of the complex eigenvectors. Realification of a complex array is a stacking of the real parts and then the complex parts, turning a vector of length  $n$  into a vector of length  $2n$ . For either the real or the realified complex case, this procedure is essentially finding a weighted average of the phase of all eigenvector components.

In analyzing the current aeroelastic system, the coordinates are not all of comparable physical or mathematical quantities- some being structural dynamic generalized coordinates and some being aerodynamic vorticities. This makes interpretation of the

---

<sup>5</sup> Afolabi, Dare, Ramana M.V. Pidaparti, and Henry Y. T. Yang, *Flutter Prediction Using an Eigenvector Orientation Approach*

results more subtle and difficult. Figure 26 shows the phase angles between the eigenvectors as functions of reduced velocity. All components of the eigenvector were utilized in this comparison.

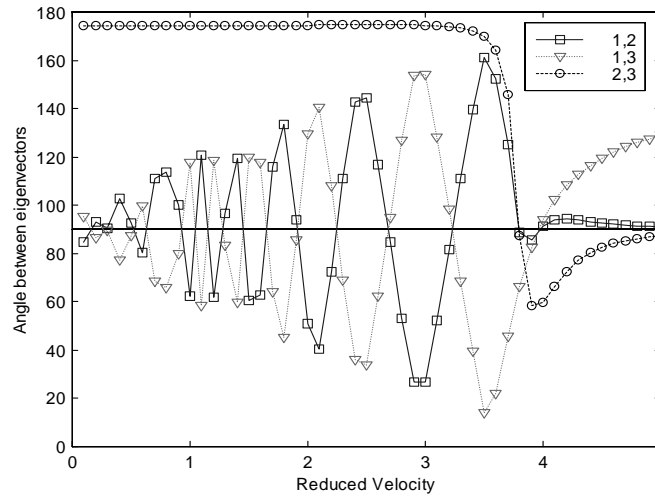


**Figure 26 Angle between eigenvectors as a function of reduced velocity, using all elements of the eigenvector**

The angle between the two real modes' eigenvectors, denoted 2 and 3, is shown in the figure with a dashed line connecting circular symbols. At low velocities, the eigenvectors are nearly out of phase. The angle between the two real modes shows a sudden transition initiated just prior to divergence. At the divergence velocity, the two real eigenvectors are orthogonal; above the divergence velocity, the phase overshoots  $90^\circ$  and then asymptotically reapproaches  $90^\circ$ .

The angles between the real modes and the dynamic mode are oscillatory as reduced velocity increases. The angle between the dynamic mode and the mode, which destabilizes is shown in the figure with a solid line connecting square symbols. The angle between the dynamic mode and the stable aerodynamic-originated mode is indicated by a dotted line connecting triangular symbols. For both comparisons, the frequency of the oscillations decreases and the magnitude increases. The underlying modeling which produces these characteristics is addressed by separately considering the eigenvector in portions corresponding to the wake vorticity components, the wing vorticity components and the structural dynamic generalized coordinates.

The vorticity in the wake is considered first. Details of the vorticity portions of the dynamic mode eigenvector were previously presented for several reduced velocities, Figure 19, Figure 20 and Figure 21. The angles between the eigenvectors were computed as previously, except that only the subset of the eigenvector components corresponding to vorticities in the wake were included. As before, the last wake element has been ignored. Figure 27 shows the angles between subsets of the eigenvectors as functions of reduced velocity. There are oscillatory patterns shown relating the phase angle of the dynamic mode eigenvector to both real eigenvectors. As in the case which utilized all components

of the eigenvectors, the frequency decreases and the magnitude increases as reduced velocity increases. From the detailed eigenvector plots of the dynamic mode, it can be seen that the cycling of the phase is more rapid at the lower velocities. The growing magnitude indicates the same thing. The more cycles that the phase goes through, the smaller the average phase of the vector. For the comparison with the stable real eigenvector (eigenvector 3), the phase angle smoothly oscillates for the entire range of velocity presented. The phase angle between the dynamic mode and the unstable mode, however, undergoes a change near the divergence velocity. The slope of the phase angle curve changes sign. This is attributed to the change in sign of the real mode eigenvector.

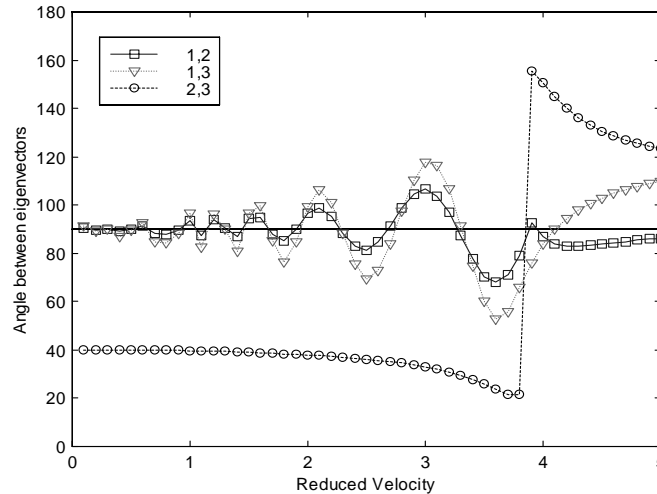


**Figure 27 Angle between eigenvectors as a function of reduced velocity, using wake vorticities without last element**

Lack of orthogonality serves to indicate the potential for energy being passed from one mode into another. The wake portion of the eigenvector does not have a direct impact on the aeroelastic feedback forces generated. To offer insight into this behavior, the wing vorticity and structural dynamic portions of the eigenvectors are examined. Because of the mismatch in physical quantities represented, they are considered separately.

The vorticity on the wing is examined next. The angles between the eigenvectors were computed, as before, except that only the portions of the eigenvectors corresponding to vorticities on the wing were included. Figure 28 shows the angles between subsets of the eigenvectors as functions of reduced velocity. The real modes are seen to be in phase throughout the velocity range presented. The relationships of the dynamic mode to the real modes are nearly identical, as would be expected after examining the phasing between the real modes. Near zero velocity, the dynamic mode is nearly orthogonal to the real modes. This orthogonality is quickly lost as the airspeed is increased. This indicates that the modes can not exchange energy when there is no velocity. From a physical standpoint, this indicates that there is no aeroelastic feedback, or interaction of the structural and aerodynamic entities, when the velocity is low. As the airspeed increases, the angle stays relatively constant. The upslope that starts just prior to

divergence is attributed to redistribution of vorticity between the real modes, which is also indicated by examining the angle between eigenvectors 2 and 3.

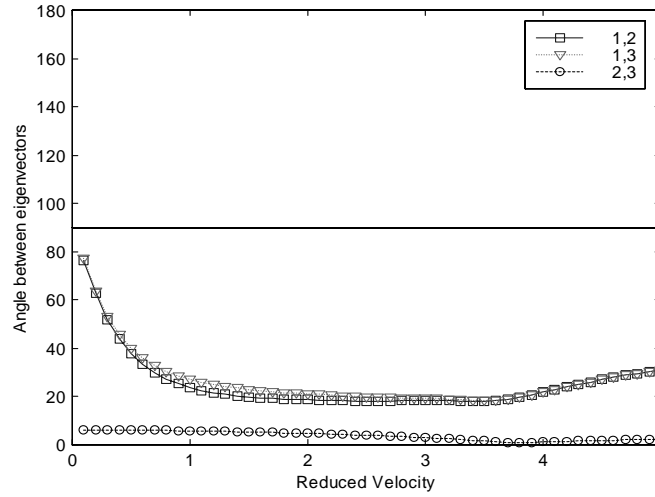


**Figure 28 Angle between eigenvectors as a function of reduced velocity, using wing vorticities only**

The structural dynamic generalized coordinate contributions to the eigenvectors are examined next. The angles between the eigenvectors were computed, using only the portions of the eigenvectors corresponding the structural portion. Figure 29 shows the angles between subsets of the eigenvectors as functions of reduced velocity. It has been mentioned that the eigenvectors were normalized such that the angle of attack generalized coordinate has a phase of  $0^\circ$ . This is true for each eigenvector individually examined. The structural dynamic eigenvector segment consists of this angular displacement and the velocity of this coordinate. For this reason, the angle between the eigenvectors, which is a weighted average for all components of the eigenvector included in the analysis, does not have a phase of  $0^\circ$ . The angle between the real modes, indicated by the dashed line connecting circular symbols, begins at low velocity with the eigenvectors nearly in phase. At divergence, there is a sharp transition, which shows that they are orthogonal at divergence, and are out of phase for velocities above divergence. The orthogonality at divergence indicates that modal energy can not be transferred from the unstable mode and dissipated by the stable real mode. For velocities below the divergence speed, the modes are nearly orthogonal, indicating that little energy is transferred between modes through the structural dynamic participation. As the velocity approaches divergence, the angle between the dynamic mode and the unstable mode changes. The modes start to lose their orthogonality. Just prior to divergence, the separation angle is approximately  $70^\circ$ , so some structural dynamic energy can be exchanged between the modes. At divergence, the modes are orthogonal, so no energy is exchanged between them. Beyond divergence, the modes are tending towards being out of phase with each other, indicating that the modal motions would oppose each other. Meanwhile, the stable real aerodynamic mode and the dynamic mode are becoming more in phase. Coupling between these two modes is highly likely at higher velocities. This coupling can be



observed also from the root locus of the eigenvalues for velocities above divergence. The migration pattern of the dynamic mode eigenvalue seen in Figure 9 is clearly influenced by the presence of the stable real mode.

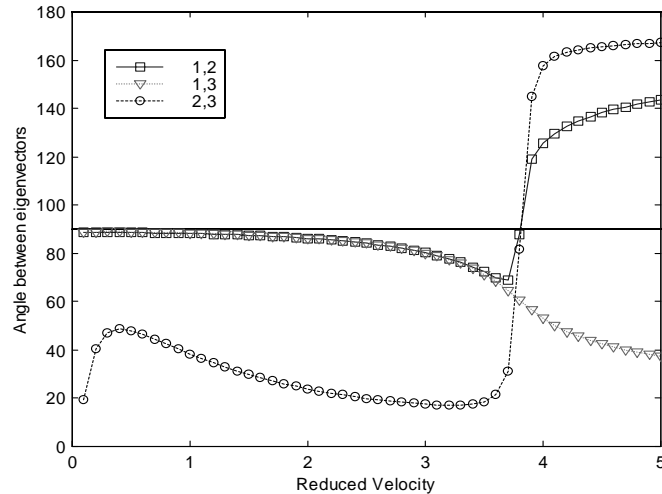


**Figure 29 Angle between eigenvectors as a function of reduced velocity, only the structural dynamic portion of eigenvectors used**

The eigenvectors were scaled such that the angular displacement has a phase of zero. It makes sense then, to examine the structural dynamic portion of the eigenvectors by considering only the contribution of the angular velocity. These results are shown in Figure 30. The phase indicates that, at divergence, the unstable mode's eigenvector phase changes by  $180^\circ$ . The dynamic mode starts orthogonal to the real modes, at  $90^\circ$ . This indicates that the dynamic mode either leads or lags the real modes of the system, such that the modes are orthogonal. As the reduced velocity increases, the phase between the dynamic mode and both real modes tend towards becoming in phase. At divergence, however, the curves separate. The angle between the structural dynamic mode and the unstable mode changes suddenly by  $90^\circ$ . The slope of the curve also changes such that it is now increasing with increasing velocity. As velocity increases, the increasing phase difference indicates that the modes tend towards becoming out of phase; they will no longer interact to accentuate each other's motion. The phase difference between the stable mode and the dynamic mode continues its migration towards  $0^\circ$ , indicating that the modes are becoming more in-phase and the will be more apt to exchange modal energy at post-divergence velocities.

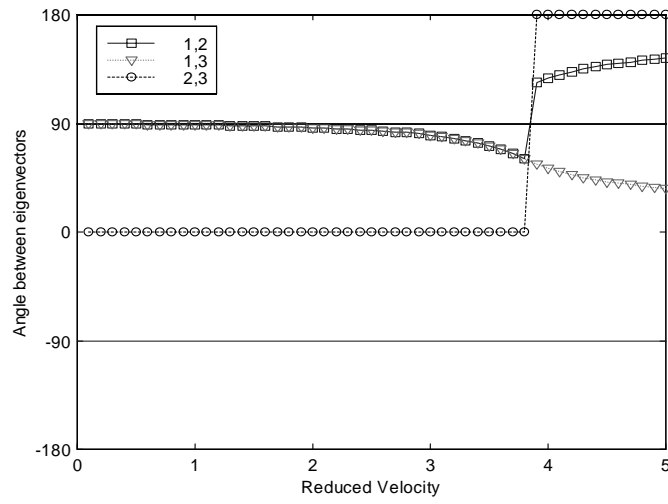


**Figure 30 Angle between eigenvectors as a function of reduced velocity, only angular velocity component**

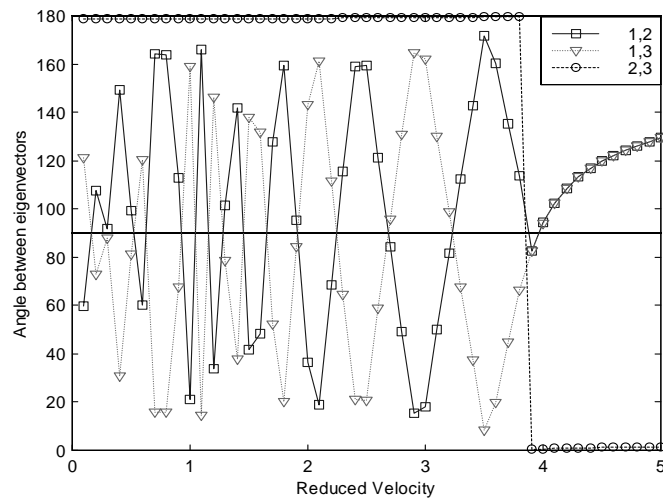


**Figure 31 Angle between eigenvectors as a function of reduced velocity, using only last element of the wake**

## Computational Issues for Simultaneous Solution of Aerodynamic and Structural Equations

### Transformation Compatibility

To incorporate the discrete time aerodynamic model into aeroelastic equations, the structural dynamic model must be cast in discrete time also. The structural dynamic equations contain first and second derivatives that could be approximated using a central difference technique. While this is convenient and easy, this method results in a mismatch of discrete time transformations. Central differencing produces discrete time equations to which a first order Tustin transformation<sup>3</sup>, Equation 19, must be applied to obtain the proper continuous time results.

$$\lambda = \frac{2}{\Delta t} \frac{(z-1)}{(z+1)} \quad \text{Equation 19}$$

The Tustin transformation is equivalent to the first term in a series expansion of the zero order hold transformation presented in equation 2. In these transformations, the sample interval,  $\Delta t$ , establishes the relationship between the discrete time eigenvalues,  $z$ , and the continuous time eigenvalues,  $\lambda$ . The aerodynamic equations which were generated with a zero order hold discretization, are solved simultaneously with the discretized structural dynamic equations. Thus, it is desirable to have structural dynamic equations that would also be correct when a zero order hold transformation is applied. This is easily accomplished through standard discretization techniques<sup>6</sup>. Accepting the mismatch in the transformations results in a phenomenon that resembles aliasing. However, as the time step becomes small, the zero order hold transform and the Tustin transform become approximately equivalent.

### Aliasing

The equations have been constructed in the discrete time domain. Given data at discrete times, a transformation can be utilized to approximate the response in continuous time. There are limitations to discrete time transformation methods; aliasing is the primary concern<sup>3,7</sup>. To avoid aliasing, a continuous time signal must have 2 samples per period of period of the highest frequency to be resolved. The aerodynamic equations arose from the fundamental concept of vorticity being convected downstream at a velocity,  $U$ . The equations are valid only if the relationship  $U=\Delta x/\Delta t$  is maintained. It is thus observed

---

<sup>6</sup> Phillips, Charles L., and H. Troy Nagle, Jr, *Digital Control System Analysis and Design*.

<sup>7</sup> Oppenheim, Alan V., and Ronald W. Schaffer, *Discrete-time Signal Processing*

that the minimum velocity, at which the system may be accurately analyzed, is set by the spatial discretization and the maximum frequency that is important to the problem. Another interpretation is that for frequency and velocity ranges of interest, the minimum number of aerodynamic elements required to avoid aliasing can be approximated. This can serve as a guideline in selecting the spatial discretization required for a given problem. There are additional implications of the discrete time effects when the aerodynamic equations are combined with the structural dynamic equations or control laws.

## **Methods of Stability Analysis**

The aeroelastic stability analyses, which require variation of the velocity, were performed using a single spatial aerodynamic discretization. This was accomplished by adjusting the temporal discretization to produce the proper velocities. There are several complications in performing the analyses in this manner: (1) a separate transformation rule must be applied for each velocity; and (2) interpreting the discrete time eigenvalues is not intuitive. The aerodynamic matrices are unchanging for different velocities, but the matrices which couple them to the structural dynamics are not. The resulting aeroelastic eigenvalues change with each velocity. The migration of the eigenvalues in the discrete time domain is not due solely to the velocity change, but to a combination of velocity and sample rate change.

A brief study was conducted to look at the results when a consistent sample rate was utilized, meaning that as the velocity changed, the spatial discretization changed. This required constructing a new aerodynamic model at each velocity. There was negligible effect on the continuous time eigenvalues. The discrete time eigenvalue pattern associated with the structural dynamic mode changed significantly. It was observed, however, that the discrete time eigenvalue pattern in this case is nearly identical to the pattern produced when the eigenvalues from the nominal analysis method are rediscritized using the consistent sample rate.

## CHAPTER THREE

### EXPERIMENT

An aeroelastic experiment was conducted in the Duke University Engineering wind tunnel facility. The goals of this test were to validate the analytical calculations of non-critical mode characteristics and to explicitly examine the aerodynamic mode divergence phenomenon. Additionally, because analyses show that the dynamic response of the system does not indicate divergence, a secondary goal of the testing was to evaluate different divergence onset prediction methodologies. To these ends, the simplest applicable model that could be devised was designed, fabricated and tested.

#### *Model Design*

The model design process first required that the desirable traits of the model be identified. Thus the non-dimensional parameter space was then examined to identify regions of parameters which would produce the best design. Physical parameter spaces were then examined to determine a configuration that could be built out of realistic materials and tested in the facility available and with reasonable expectations of instrumentation and data processing techniques.

The desirable traits that were utilized in the model design range from the patently obvious to the sublime. It was desirable to have the model shaped like an airfoil. This is an important limitation- the shape restricts the strength, stiffness and inertia combinations which are achievable. It is also desirable that the model be constructed of machinable materials. This is a limitation, particularly in terms of an upper limit on the density and a lower limit on the strength and stiffness of available materials. It was also desired to have a wing structure that would not introduce additional modes into the experiment. This required that the airfoil be rigid in both the chord-wise and span-wise directions.

The facility in which a model is tested places additional limitations on the design space. The model design must diverge at a dynamic pressure that the wind tunnel can reach. To ease mounting and eliminate tip aerodynamic phenomena, it was desirable to have a wing which would span the entire tunnel. To eliminate gravitational effects from the experiment, it was desirable to mount the wing between the floor and ceiling rather than spanning from one sidewall to the other. These two requirements fix the span. It is desirable to avoid tunnel blockage effects. The cross-sectional area of the tunnel, coupled with expected deflection angles of the model, sets an upper limit on the airfoil chord length if blockage is to be avoided.

The above requirements limit the design space before consideration of demonstrating the desired phenomenon are addressed. It is desirable to find a place in the design space which satisfies all of the above constraints and also demonstrates aerodynamic mode divergence. For clarity in identifying that the system has diverged while the dynamic mode persists, the designed model should have a high structural dynamic mode frequency at divergence. Low damping of the dynamic mode at the divergence condition is also desirable. The lower the damping of this mode, the more obvious the modal characteristics will appear. Further, it is desirable to demonstrate, through simple configuration changes to the model, different types of divergent behavior.

The non-dimensional parametric variation database of modal characteristics at divergence was discussed previously. The structural dynamic parameters varied in the database are elastic axis location,  $e/b$ , radius of gyration,  $r_\alpha$ , and mass ratio,  $\mu$ . This database was utilized to identify regions in the parameter space where the divergence mechanism exhibited aerodynamic lag divergence. Additionally, it served to find regions where the damping and frequency characteristics were most desirable.

Dimensional design spaces were also constructed. Although not presented here, the torsional spring stiffness, pitch inertia, mass, semichord and elastic axis location variations were examined. These variations allowed consideration of many of the issues associated with model construction and testing. They served to reduce the design space to a general description of the model. Fundamental characteristics of the configuration chosen were a NACA 0012 airfoil with a chord length of 8 inches, manufactured from aluminum as a thin-walled closed cell with spanwise stiffeners located near the elastic axis. Trailing edge segments made of different materials serve as the mechanism to determine and reconfigure the pitch inertia.

Design-specific variations of physical variables were then examined. There were three physical quantities that were still adjustable within reasonable limits and still produce a model which could be manufactured: torsional spring stiffness, mass of the trailing edge segment, and distance from the trailing edge segment to the center of rotation.

The torsional spring stiffness could be adjusted. As noted in the non-dimensional parametric variation, this produced no effect on the migration pattern of the eigenvalues. The torsional spring stiffness was used to control the magnitude of the frequency of the dynamic mode at the divergence condition. This is a measurement and data processing fidelity issue, not a phenomenon issue. The limitation on increasing the stiffness is the tunnel dynamic pressure capability. Increasing the stiffness increases the frequency, but also the divergence airspeed.

The two remaining design freedoms were simultaneously varied; the results of these variations are shown in Figure 32 and Figure 33. These figures are very similar in shape and magnitude to the sample results presented for the non-dimensional parameter database at a fixed mass ratio, Figures 15 and 16. Figure 32 presents the ratio of the

dynamic mode frequency at the divergence condition to the air-off torsional frequency. The undulating surface is a function of elastic axis position and ratio of the trailing edge mass to the total mass of the system. The solid square shown at the ratio of masses value of 0.01 corresponds to the Plexiglass trailing edge configurations, configurations # 2 and # 3. The solid symbol at the ratio of masses value of .56 represents the Tungsten trailing edge configuration, configuration #1. From this figure, it is anticipated that the two designed inertia configurations will produce different dynamic mode migration.

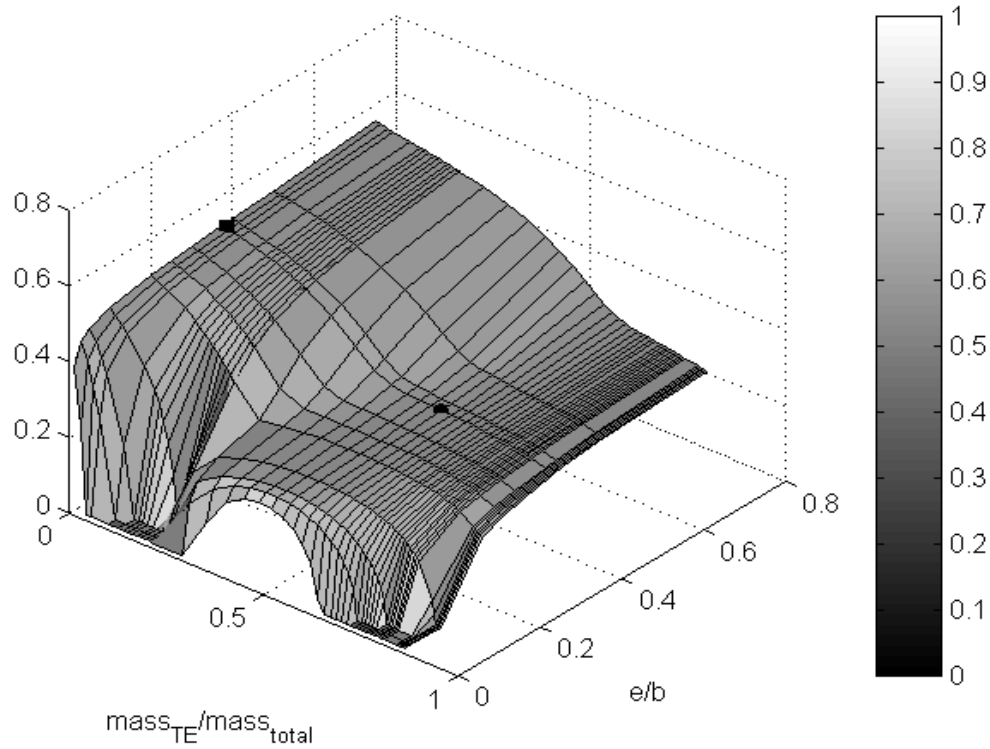


**Figure 32 Physical parameter variation results; ratio of frequency of dynamic mode at divergence to pitch mode natural frequency**

Figure 33 presents the damping of the dynamic mode at the divergence. Again, the surface is a function of elastic axis position and ratio of the trailing edge mass to the total mass of the system.

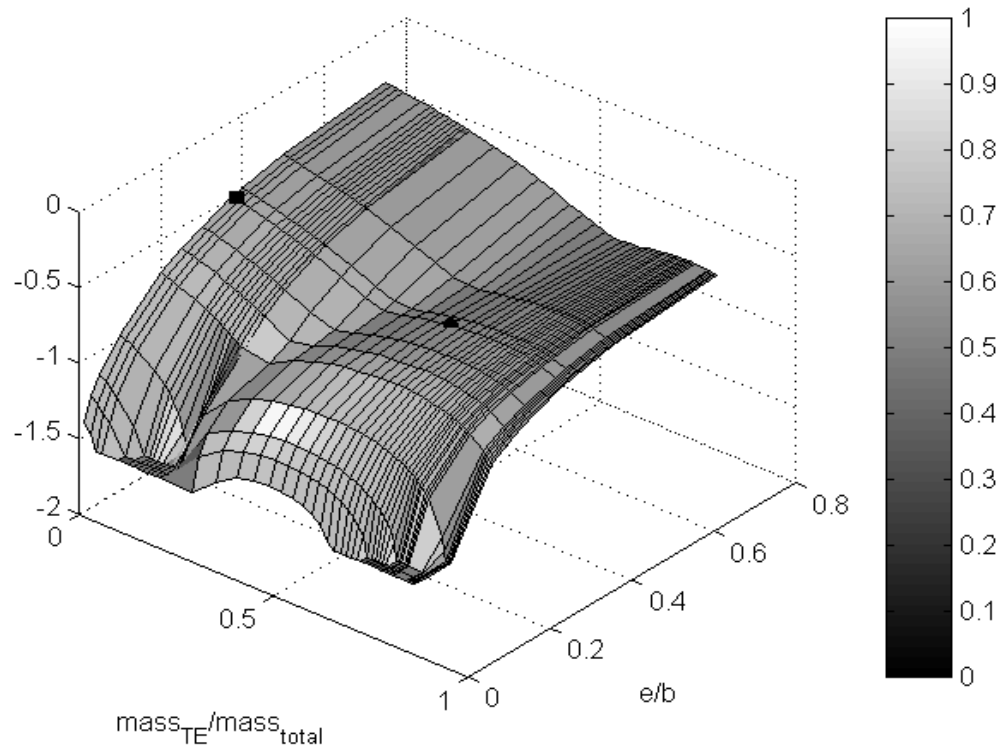


Figure 33 Physical parameter variation results; damping of dynamic mode at divergence condition

### *Configuration Descriptions*

Three configurations of the model were designed for testing. The configurations differ in their torsional stiffness and inertial properties. These properties influence the natural or zero-airspeed structural dynamic frequency. In addition, analyses indicated that the subcritical migration pattern of the dynamic mode eigenvalue is strongly influenced by the inertial properties.

Reconfiguring the model's pitch inertia was accomplished by changing the airfoil trailing edge. This also changes the non-dimensional mass ratio. Configuration #1 employed the Tungsten trailing edge component, while the second and third configurations employed the Plexiglass trailing edge component. These materials were chosen to provide a large difference in the torsional inertias, and thus an observable difference in the non-critical mode behavior. Examining Figure 32 and Figure 33, there are solid symbols shown on the surfaces at the ratio of masses value of .56; these are the expected frequency ratio and damping for the Tungsten trailing edge configuration, configuration #1. The solid squares shown in the figures at the ratio of masses value of 0.01 corresponds to the



Plexiglass trailing edge configurations, configurations # 2 and # 3. The two inertia designs lie on different tiers of the frequency ratio surface. At divergence, the frequency of the tungsten configuration is expected to drop to 29% from of its air off frequency. The frequency of the Plexiglass trailing edge configuration is expected to drop to 53% of the air off frequency when the system destabilizes. Additionally, the dampings are different. The analytical frequency ratios and damping at divergence for the three configurations are given in Table 11. From this data, it is anticipated that models with the two designed inertias will produce discernibly different dynamic mode migrations.

Config #	$\frac{mass_{TrailingEdge}}{mass_{Total}}$	$\omega_{\alpha}$ (air off)	$\omega_D$	$\omega_D / \omega_{\alpha}$	$\zeta_D$
1	0.56	21.2	6.2	0.29	0.51
2	0.01	49.5	26.4	0.53	0.75
3	0.01	87.3	46.4	0.53	0.75

Table 11 Analytical frequency ratios and damping at divergence

Reconfiguring the model stiffness was accomplished by changing the torsional spring and thus the stiffness. The first two configurations used a 1-inch diameter torsional spring with an advertised stiffness of 0.94 lb<sub>f</sub>-in/degree. The third configuration employed a ¾-inch spring line with an advertised stiffness of 3.18 lb<sub>f</sub>-in/deg. The stiffnesses were measured and will be discussed in the experimental results section.

Table 12 provides a summary of the configurations. The dimensional quantities and non-dimensional parameters for each were previously listed in Table 5. Model configuration #2 serves as a comparison configuration to each of the others and will be discussed in much more detail than the other two.

Config #	Trailing Edge Segment		Torsional Spring	
	Material	$\frac{mass_{TE}}{mass_{Total}}$	Diameter	Stiffness (lb <sub>f</sub> -in/deg)
1	Tungsten	0.56	1"	0.90
2	Plexiglass	0.01	1"	0.90
3	Plexiglass	0.01	¾"	2.78

Table 12 Description of wind tunnel model configurations

## ***Hardware***

### **Wind Tunnel Model**

The divergence assessment testbed (*dat*) wind tunnel model consists of a typical section airfoil with a flexible mount system providing a single degree of freedom structural dynamic mode. The only structural dynamic mode of this model is torsional rotation, or angle of attack.

#### **Airfoil Description**

The airfoil section is a NACA 0012 with an 8-inch chord and a span of 21 inches. This spans the entire test section from the floor to ceiling, as shown in Figure 34. The airfoil is an aluminum shell, 1/32 inch thick. To ease fabrication and instrumentation it was made in two sections that join at approximately the mid-span. The internal structure has two spar webs running the entire span to provide bending rigidity and the designed inertial properties. Each of the two span sections consists of internal spars and airfoil which were cut as a single entity from a solid block of aluminum using a wire electro-deposit-machine (EDM). The last 1.125 inches of the airfoil were fabricated separately to provide test configurations with different inertial properties. To effect a large change in inertia, trailing edge segments were fabricated from Plexiglass and from Tungsten. These trailing edges could be easily changed during the test.



**Figure 34** Researcher installing wind tunnel model; airfoil shown with Plexiglass trailing edge segment

### **Mount System**

The mounting system for the *dat* model has a ceiling mechanism and a floor mechanism. Both portions of the mount system are required for mounting the model and holding it in place.

The ceiling mechanism, shown in Figure 35, serves three functions in addition to holding the model in place. The torsional spring is contained in the ceiling mechanism. Sometimes called a barrel spring or a Bendix flexure, the spring provides the stiffness associated with the structural dynamic torsion mode. The ceiling mount also contains a turntable which allows the rigid angle of attack to be set and changed. Mounted between the turntable and the torsional spring is a balance which measures torsional strain.



**Figure 35** Ceiling mechanism of mount system

This mount system was designed and built with couplers to connect the torsional spring to the balance and to the airfoil. Three sets of couplers were fabricated so that springs of various sizes could be easily substituted. This system flexibility allows configuration changes in stiffness during the test.

The floor mount system serves two functions in addition to holding the model in place. The floor mount mechanism is shown from below, looking up at the airfoil and ceiling mount system, Figure 36.



**Figure 36 Floor mount mechanism, viewed from below**

A shaft extends out of the wing through the tunnel floor and is fixed to an angular displacement transducer. This allows the total angle of attack of the wing to be measured including the rigid angle of attack set using the ceiling mount and the elastic increment. Additionally, the sensor wing and pressure reference tubes pass out of the tunnel through this mount system.

#### Torsional stiffness testing of springs

The torsional springs were tested to determine their stiffness constants, as well as evaluate the range of operation and linearity. The springs were inserted into a test fixture which measured the torsional moment and the deflection angle. Weight was applied to the test fixture in a manner which caused one end of the spring to rotate through a deflection angle. The applied weight was increased and data acquired at each weighting until the deflection angle stayed constant. The data set was fit with a linear equation that minimized the error in the least squares sense. The torsional spring stiffness constant is the slope of torsional moment versus deflection angle.

The data for the 1-inch diameter spring is shown in Figure 37, along with a linear fit to the data and the manufacturer's specifications. Several data sets were acquired for each spring. Each data set was curve fit with and without constraining the y-intercept. Curve fits to the data sets produced spring constants between .87 and 1.08 lb<sub>f</sub>-in/degrees. After consideration of pluck test results and inertia measurements, the value to be used in

comparison analyses was set as 0.90 lb<sub>f</sub>-in/degree. The manufacturer's specification for this spring, 0.94 lb<sub>f</sub>-in/degree, falls within the scatter of the measurements and curve fits.

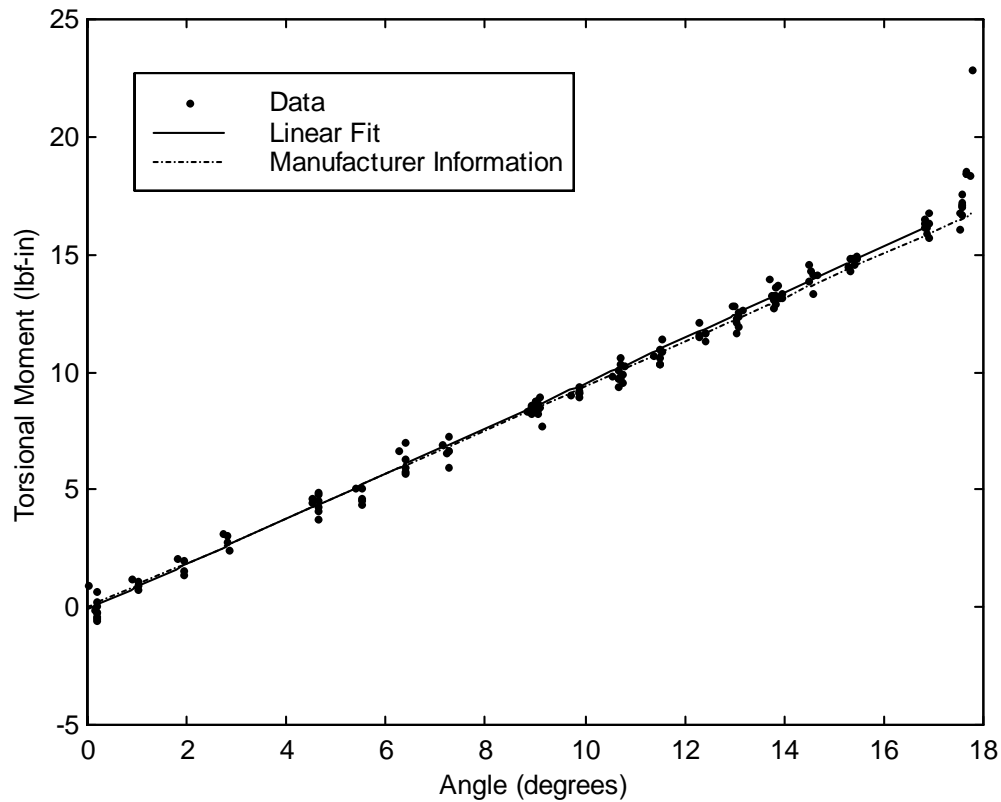


**Figure 37 Stiffness data for 1 inch diameter torsional spring**

The data for the  $\frac{3}{4}$ -inch diameter spring is shown in Figure 38, along with a linear fit to the data and the manufacturer's specifications. Curve fits to the data sets produced spring constants between 2.6 and 2.8 lb<sub>f</sub>-in/degrees. The nominal value for performing comparison analyses was set as 2.78 lb<sub>f</sub>-in/degree. The manufacturer's specification for this spring, 3.18 lb<sub>f</sub>-in/degree, is significantly higher than the measured value. This difference invalidated preliminary estimates of the divergence dynamic pressure. However, the qualitative behavior of the eigenvalues were shown in the analysis to be invariant with respect to torsional stiffness.

Based on the measured data, both springs appear to behave in a linear manner for angular displacements below 18 degrees.

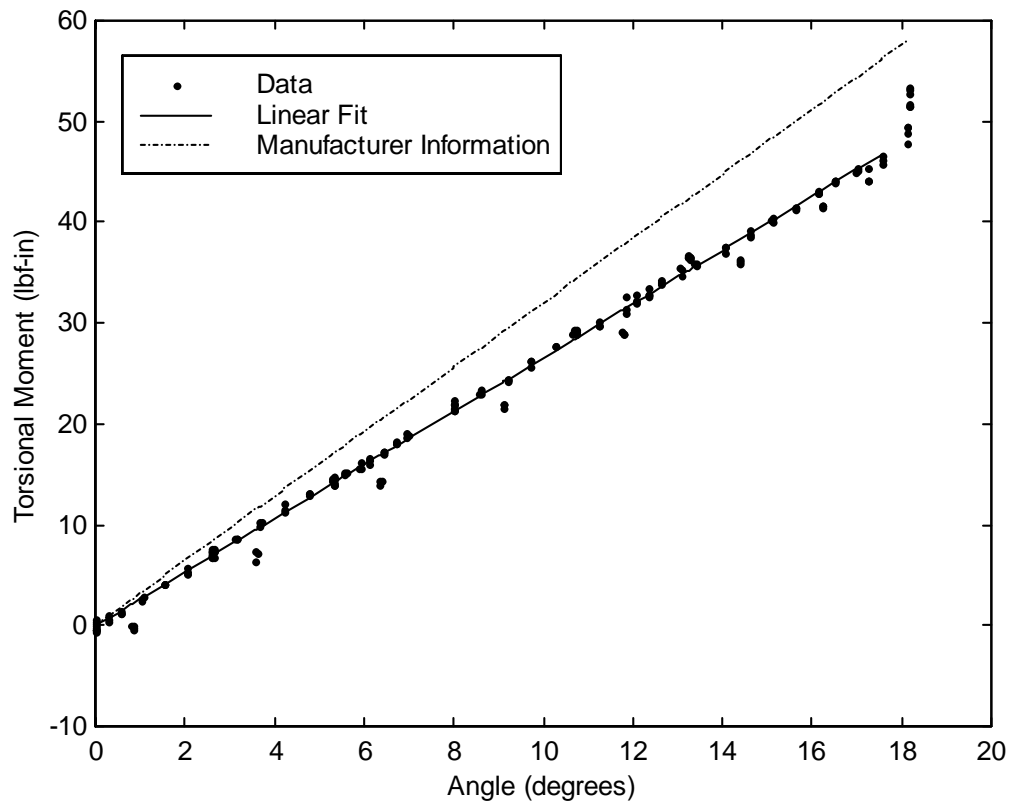


**Figure 38 Stiffness data for 3/4 inch diameter torsional spring**

#### Model Instrumentation

The wind tunnel model was instrumented with the following sensors. A Trans-tek angular displacement transducer was mounted to the bottom shaft of the airfoil. The measurement was made such that the total angle of attack was measured, including the prescribed rigid contribution. A torsional moment sensor connected the angle of attack turntable to the torsional spring coupler. This sensor served the role traditionally played by a balance. A piezoresistive accelerometer was mounted inside the airfoil towards the leading edge. This type of accelerometer is dc-coupled, providing static values, as well as dynamic frequency responses. Unsteady pressure transducers were mounted at the approximate midspan of the airfoil section. One transducer was on the leading edge. Eight others comprise pairs of top- and bottom- mounted pairs. These eight transducers were mounted at the 5%, 15%, 30% and 52% chord locations, respectively.

#### Facility Description

This test was conducted in the wind tunnel facility at Duke University. Two gust vanes were installed vertically in the tunnel, ahead of the model. Each gust vane system

consists of a fixed airfoil and a slotted cylinder. The slotted cylinders were placed just aft of the gust vane airfoils. Each cylinder was mounted to a shaft. The shaft was held by rotating bearings in the ceiling and floor. Beneath the wind tunnel floor, the shafts were connected by a gear and belt system to a motor. Via this motor, the cylinders were rotated. Voltage supplied to the motor governs the motor speed and thus the rotational frequency of the slotted cylinder. Through this mechanism, aerodynamic forcing of the test article was achieved.

### Data Acquisition System

The data was acquired using a portable, self-contained system. The signals were input to signal conditioners, the type of which depends on the sensor. The signal conditioners sent voltages to a National Instruments DAQ 700 card which was inserted into the game card slot of a laptop computer.

The DAQCard-700 is a Type II PCMCIA card with 12-bit analog to digital conversion.<sup>1</sup> It can acquire data from 16 single-ended analog input channels with a maximum sample rate of the card is 100 kilosamples per second. The card has DC input coupling, enabling static measurements. A FIFO buffer contains the data during multiple analog to digital conversions to prevent data loss. An onboard counter/timer generates the sample interval clock. For this study, multichannel acquisition with continuous scanning was the mode of operation, taking one reading per sample interval, always in the same channel order, starting with the highest channel number.

The data acquisition system was driven by virtual instruments designed in Labview, a National Instruments software interface to their data acquisition products.

### *Experimental Data Acquired*

Wind tunnel test data was acquired to investigate experimentally system behavior and validate analytical results. Specifically, data was acquired: 1) to find the divergence dynamic pressure; 2) to examine the modal characteristics of non-critical modes, both subcritically and at the divergence condition; 3) to examine the eigenvector behavior. A secondary goal of acquiring and analyzing this data was to evaluate standard experimental divergence onset prediction methods. Addressing these goals required that several different experimental methods be employed for acquiring data.

---

<sup>1</sup> DAQCard-700 User's Manual: Multifunction I/O Board for the PCMCIA BUS

The first type of data acquired was system response to turbulence occurring naturally in the tunnel. Initial divergence testing was performed by increasing the dynamic pressure or velocity of the airstream. Stability or instability of the system was observed; data was acquired. The majority of the turbulence-excited data was acquired at fixed wind tunnel velocity. These data are referred to in this text as velocity stabilized points.

Forced response data was also acquired. One method employed to excite the system was applying a pluck or a rap to the mount system, as shown in Figure 39. A portion of the mount system accessible from outside the tunnel was connected to the moving portion of the torsional spring. Applying a force to the bottom coupler was equivalent to rapping the airfoil. Data was acquired as the model was plucked or rapped; the model response was recorded as the motion decayed, or grew in the case of unstable systems.



**Figure 39 Administering a pluck to the model**

The second method of forcing the system was to employ the gust vanes, which were described previously. While the pluck test method utilizes the structure to apply the forcing function, the gust method acts through aerodynamic forces. Two types of gust excitations were used to acquire data. The first type of excitation used was a sweep of the frequency range of interest, starting at the high frequency end and progressing to low frequency. The second type of excitation provided by the gust vanes was rotation of the cylinder at a fixed frequency, dwelling at a single frequency. The latter method is referred to in this text as the sine dwell method of excitation.

### ***Data Processing***

The measured data was utilized to glean insights into the system behavior. Examining different system characteristics required that the data be processed in several ways.

Identifying the divergence condition was accomplished by observing the system stability as the dynamic pressure was increased. Additionally, the divergence onset was predicted using several methods which are classically employed in experiments. Because it is a contention of this work that the dynamic mode persists at a nonzero frequency as the instability is reached, it is interesting to contrast the results obtained from static and dynamic prediction techniques. The static methods used were load monitoring, angle of



attack ratio monitoring, and the Southwell method. The dynamic methods employed were frequency tracking and inverse amplitude tracking.

Identifying modal characteristics was accomplished by scrutinizing the time history data. Frequency domain analyses and the logarithmic decrement technique of determining damping were utilized. The frequency domain analyses include analyzing the Fourier transformations, the power spectral density functions and approximated transfer functions.

### ***Experimental Results***

#### **Configuration #2**

The experimental data for wind tunnel model configuration # 2 is presented first. Configuration # 2 has the 1-inch diameter torsional spring and has the Plexiglass trailing edge. This configuration has lower torsional inertia than the Tungsten configuration, model configuration #1, but has the same torsional stiffness. This configuration has lower torsional stiffness than the  $\frac{3}{4}$  inch spring configuration, model configuration # 3, but has the same torsional inertia. Thus this configuration serves as a comparison configuration to each of the others. Results will be presented and discussed in the following order: determination of the divergence condition, subcritical techniques for predicting divergence onset, system behavior at divergence, and subcritical modal characteristics.

#### **Divergence dynamic pressure**

Divergence testing was conducted by setting the zero airspeed angle of attack,  $\alpha_0$ , which is referred to as the rigid angle of attack, as close to zero as possible. The divergence dynamic pressure was determined by increasing the velocity and recording data as the system became unstable. A time history showing the divergence of this configuration is shown in Figure 40. The dynamic pressure was being slowly increased until the angle of attack increased dramatically and suddenly. This was declared as the divergence dynamic pressure, 5.1 psf (244 N/m<sup>2</sup>). The time history shows that the model oscillates about a new angle of attack position, which is not at the hard stop of the spring. It is speculated that the airfoil has reached an angle of attack where flow has separated and stall has occurred. This issue and the ensuing behavior of the system are further discussed at the end of this section on experimental results.

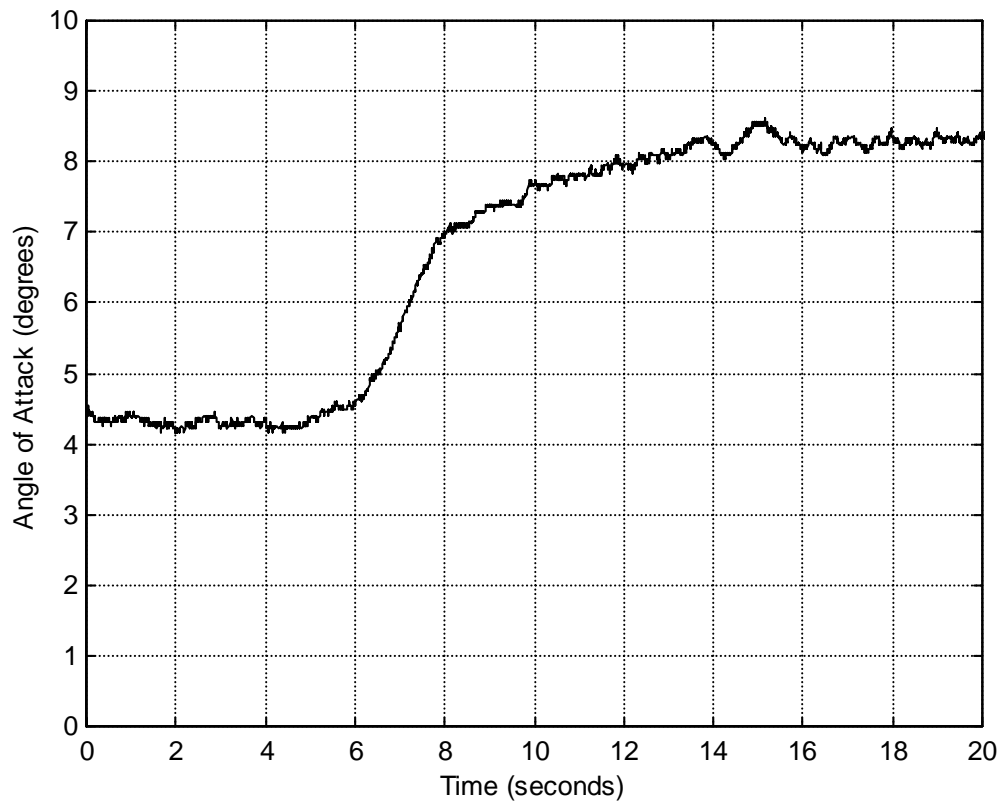


**Figure 40 Divergence of wind tunnel model configuration #2**

### **Divergence prediction using subcritical data**

Five methods of experimentally predicting divergence onset were utilized in this work. Three methods which examine the static properties and two dynamic response methods of analyzing data were applied.

Static load monitoring is a fundamental method of predicting divergence. This method depends on the monitored load becoming large as divergence is approached. The slope of the moment versus dynamic pressure curve is the key parameter. This slope changes dramatically in the neighborhood of divergence. In this experiment, the torsional spring moment is the monitored load. In applying this method, data sets are acquired at several rigid angles of attack. For each rigid angle of attack, data was recorded at regular intervals of dynamic pressure. Data for each angle is treated as a data set. The data is shown in Figure 42. The legend indicates the rigid angle of attack for each of the traces in the figure.

Two data sets were acquired for rigid angles of attack very near zero degrees as shown in Figure 41. For these data sets, the torsional moment is very small until just before the divergence condition is reached; the load is seen to increase dramatically at this point. The steep slope indicates that divergence is imminent.

Data is also presented for non-zero rigid angles of attack. The terminations points of these curves show the last dynamic pressure before the system became unstable for each rigid angle of attack. A method for estimating these destabilizing dynamic pressures will be presented in the discussion section. The increase in load with changing dynamic pressure is more gradual for larger  $\alpha_0$ . The structural moment is directly proportional to the elastic increment in the angle of attack. Examination of the static equilibrium equations for this system shows that the elastic increment is an amplification of  $\alpha_0$ .

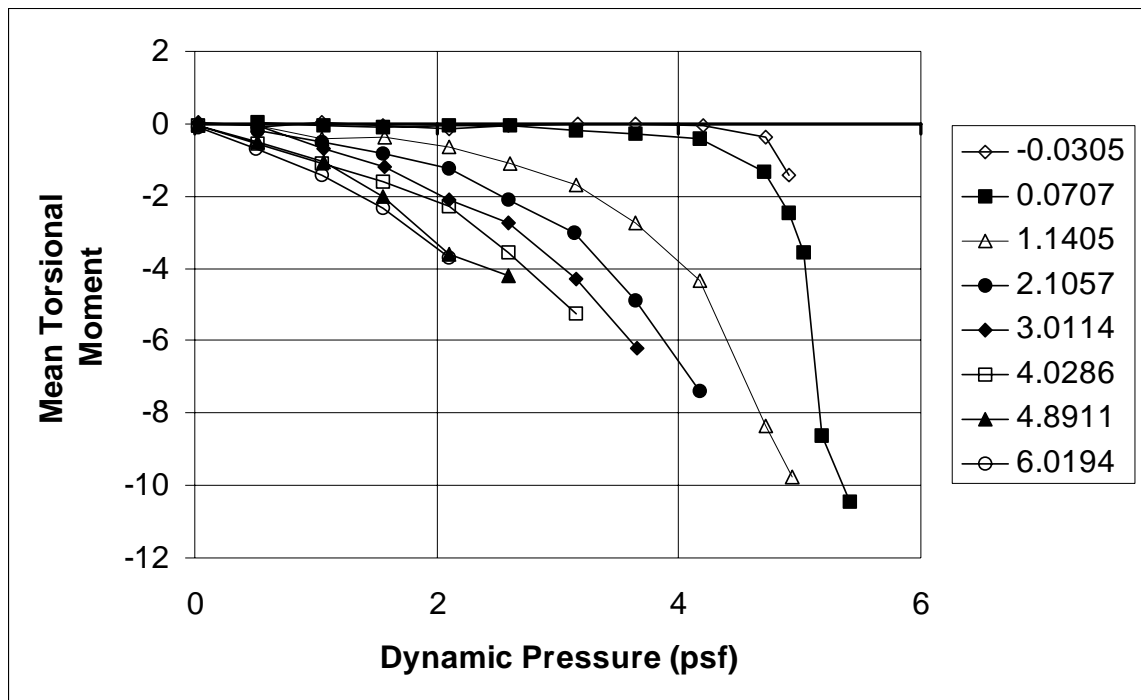


Figure 41 Strain monitoring for predicting divergence onset

The second method of predicting the onset of divergence is examining the angle of attack as the dynamic pressure is increased. Divergence is classically defined by the angle of attack becoming infinitely large, or the inverse of the angle becoming zero. Figure 42 shows the inverse angles of attack data. The data has been normalized by the rigid angle; this normalization collapses the data to a single line.

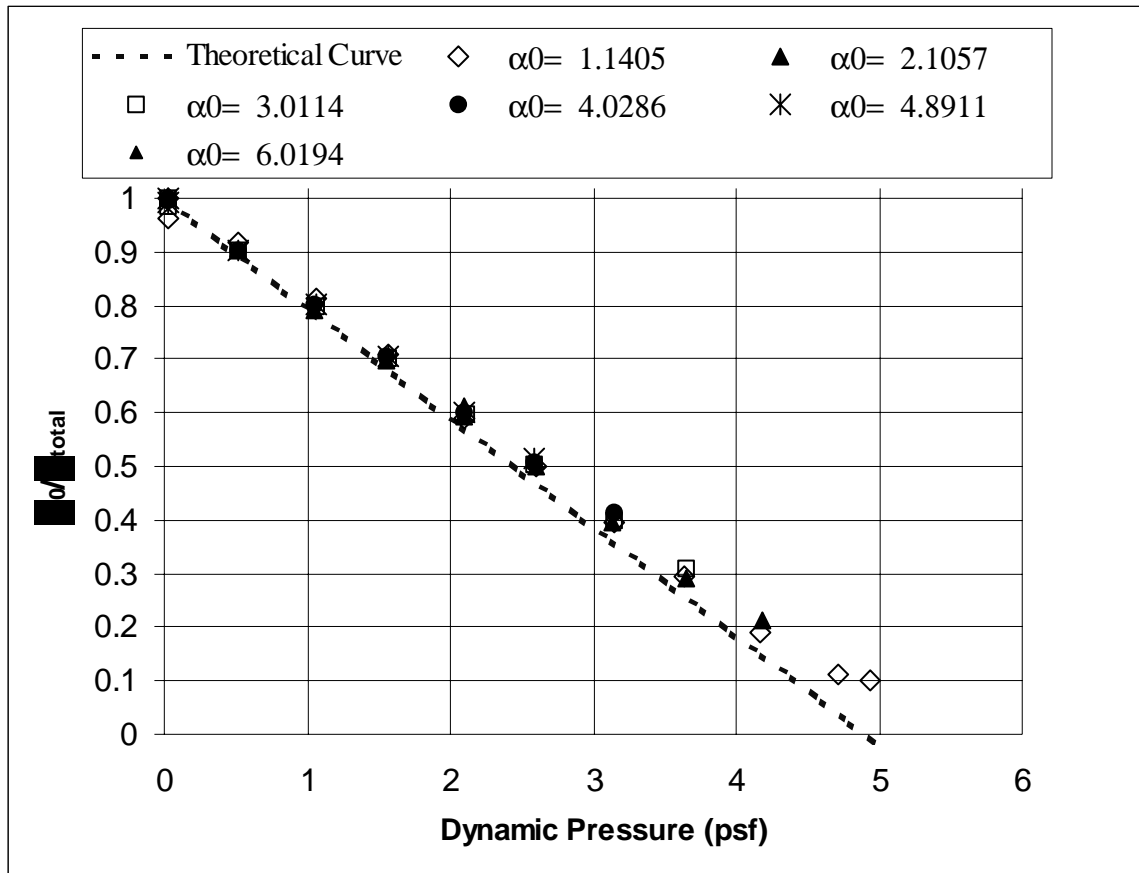


Figure 42 Predicting divergence using angle of attack ratio

A linear fit through the experimental data produces a divergence dynamic pressure of 5 psf. The theoretical curve, which employs the measured value of torsional stiffness produces a divergence dynamic pressure of 4.6 psf. The experimental prediction using this method is 9% higher than the theoretical result. The disagreement between analysis and experiment is resolved by utilizing a measured value of lift coefficient instead of the ideal of  $2\pi$ . Using  $C_{L\alpha} = 5.7$  1/radians produces a divergence dynamic pressure of 5.08 psf.

The two static methods used previously are combined in the Southwell method. To apply the method, the static load is measured at fixed dynamic pressures for various rigid angles of attack. The data at each dynamic pressure constitutes a single data set. A linear fit is made to each data set, plotting static moment versus angle of attack. The data is shown in this manner in Figure 43. The slope of each line is denoted,  $\lambda$ . Divergence occurs at the dynamic pressure which makes the slope of these data infinite.

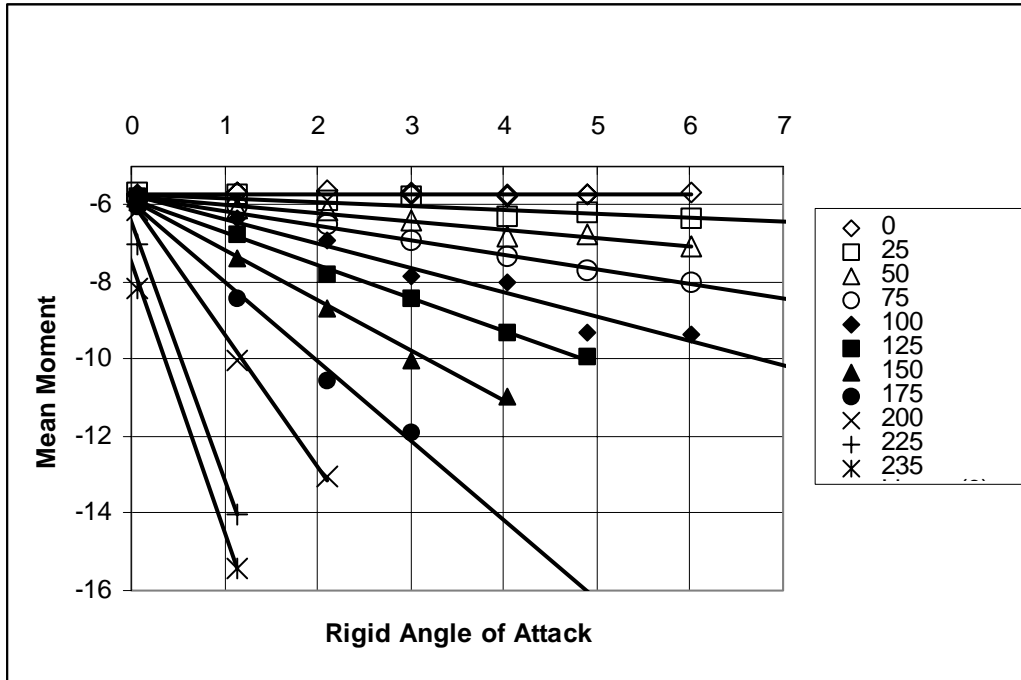


Figure 43 Intermediate Southwell plot

The data sets are combined into a single plot. The slope,  $\lambda$ , is plotted versus itself, normalized by the dynamic pressure. The slope of this line predicts the divergence dynamic pressure. Figure 44 shows the data for this configuration, with a slope of 5.5 psf.

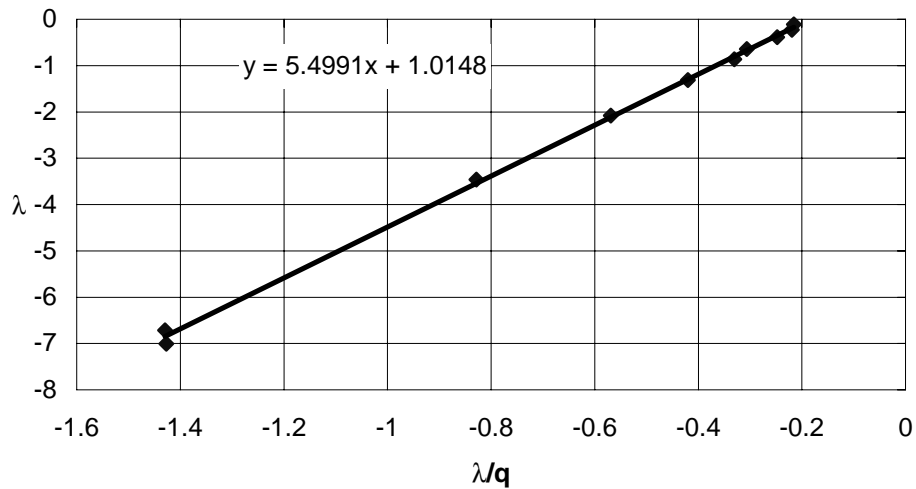


Figure 44 Southwell method for predicting divergence onset

During a divergence onset test, the Southwell method is applied as the dynamic pressure data is acquired. Figure 45 shows the prediction of the Southwell method as additional

data is considered in the linear fit. Using only data below 2.1 psf, the divergence prediction of 5.2 is fairly close to the final divergence prediction which utilized data up to 5.2 psf.

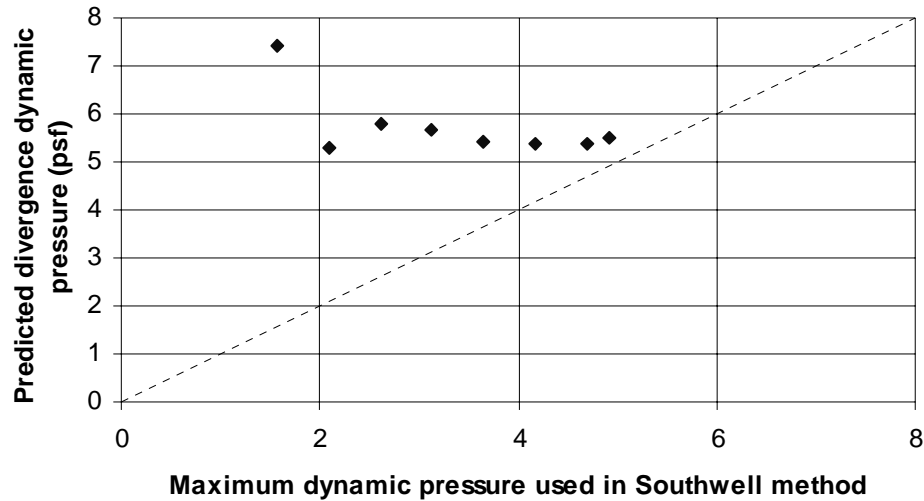


Figure 45 Southwell method results using increasing amounts of data

Dynamic methods were also applied to predict divergence. Divergence is classically considered to occur as the torsional mode frequency drops to zero and then statically destabilizes. One classical method of predicting the onset of divergence is to monitor the torsional mode frequency migration, anticipating that it will go to zero prior to divergence. Figure 46 shows the system frequency extracted from subcritical data as the dynamic pressure is varied. The Fourier transformation of the angle of attack response was computed for data generated when frequency sweeps were input to the gust vanes. At divergence, the frequency is still greater than 3 Hz for this configuration.

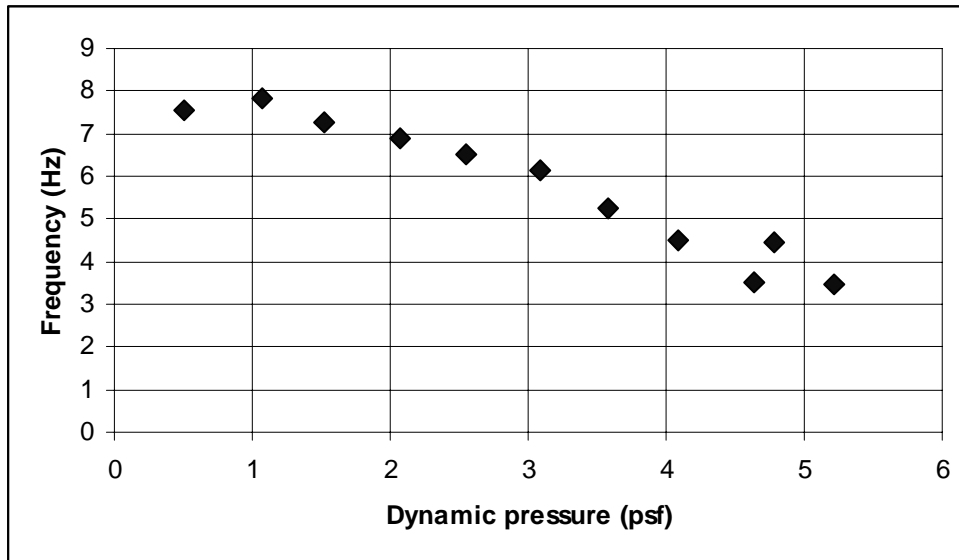


Figure 46 Frequency tracking to predict divergence

A second method that relies on the same data and analytical techniques as the frequency tracking method. The amplitude of the system response is anticipated to become large as divergence is encountered. Rather than utilizing the static response as was done previously in the load monitoring method, the amplitude of the modal response is tracked. Figure 47 shows this data. The amplitude is actually seen to decrease until the last data point before divergence.

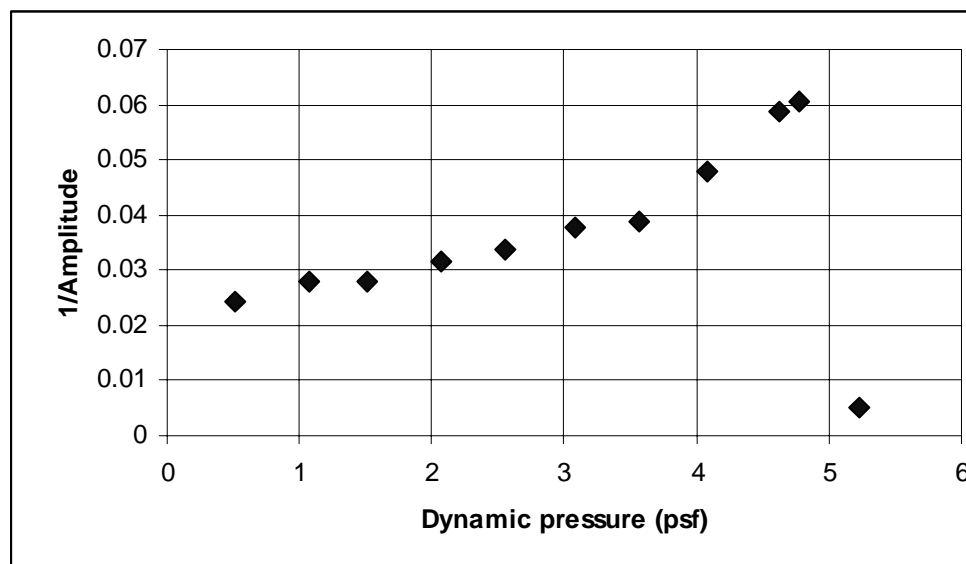


Figure 47 Inverse amplitude of the power spectral density of the angle of attack response

## Extracting modal characteristics

One of the primary concerns of this study is tracking the modal characteristics of the aeroelastic system as the dynamic pressure increases towards the divergence condition. Identification of the torsional mode frequency and damping was accomplished by employing different excitation, measurement and data processing techniques.

The structural damping of the system without any aerodynamic forces acting can be determined by considering the decay of the response due to a rap or a pluck. A pluck was applied to the model, as shown in Figure 39 and the logarithmic decrement method was used to analyze the data.

The logarithmic decrement is a well-documented method for calculating the damping of a system<sup>2</sup>. Applying the method is dependent upon having a time history of a decaying response where several cycles of the decaying motion are evident. Air off pluck test data is shown in Figure 48. The time history shows the angle of attack displacement as a pluck is administered to the model and the motion decays. The circular symbols indicate the values which were used in the damping calculation.

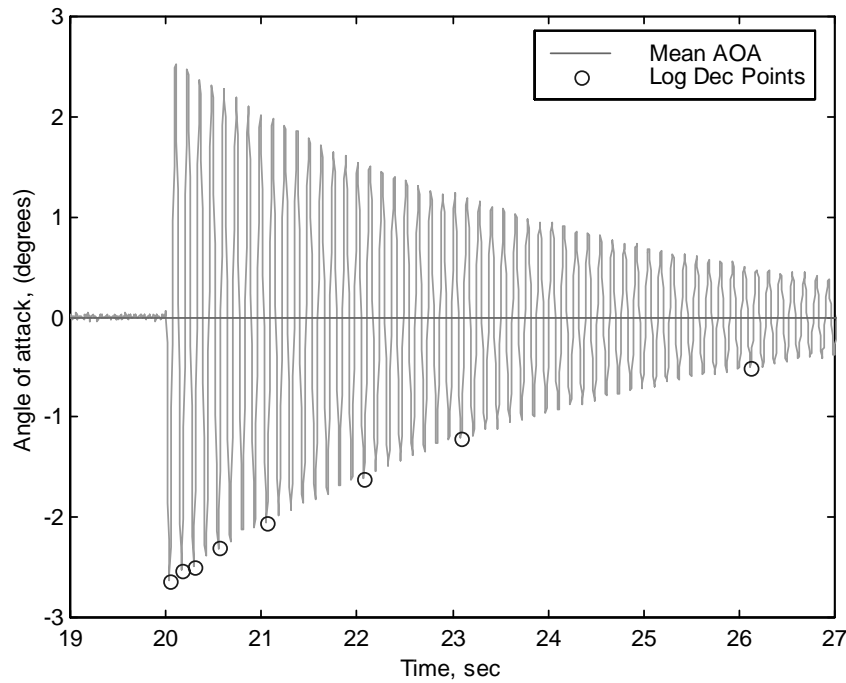


**Figure 48** Extracting logarithmic decrement data from angle of attack time history, air off data for configuration # 2

The logarithmic decrement,  $\delta$ , is calculated using Equation 20 which then produces a damping value from Equation 21. The amplitudes of the 0<sup>th</sup> and N<sup>th</sup> cycles are denoted

---

<sup>2</sup> Clough, Ray W., and Joseph Penzien, *Dynamics of Structures*,



by  $a$  in this equation. The real part of an eigenvalue can be calculated from the damping and the frequency, as shown in Equation 22.

$$\delta = \frac{\log\left(\frac{a_N}{a_0}\right)}{N_{cycles}} \quad \text{Equation 20}$$

$$\zeta = \frac{\delta}{\sqrt{4\pi^2 + \delta^2}} \quad \text{Equation 21}$$

$$\text{Re} = \frac{-\sin(\zeta)\omega}{\sqrt{1 - \sin^2(\zeta)}} \quad \text{Equation 22}$$

Data was acquired and analyzed in this manner for subcritical dynamic pressures. Figure 49 presents the results of numerous applications of the logarithmic decrement method. The damping and frequency information were converted to real and imaginary components representative of a single mode. The real part is plotted as a function of the dynamic pressure. Results from individual time histories are shown as small open circles. The larger solid circles are the average results at each dynamic pressure. While the damping is well defined and repeatable at low dynamic pressures, the uncertainty at the higher dynamic pressures becomes quite significant.

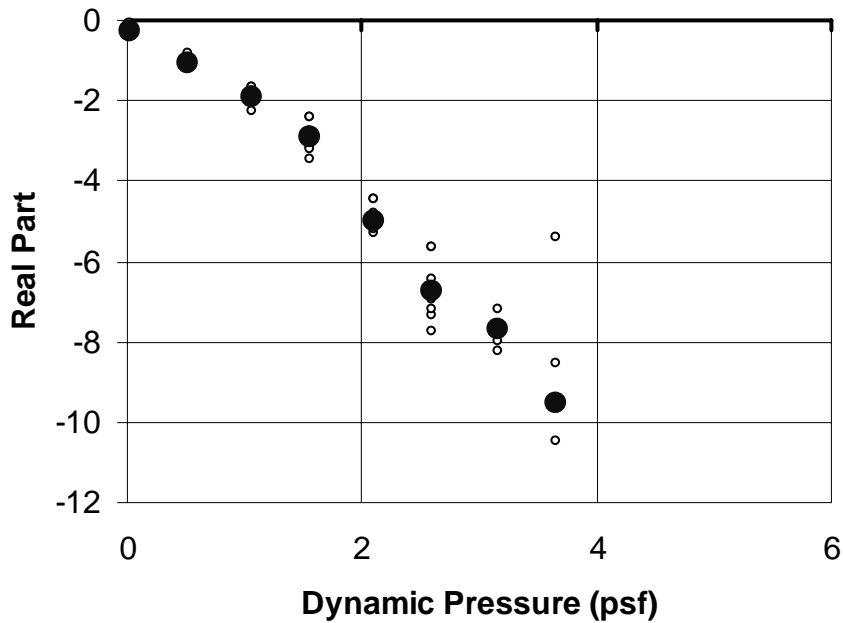
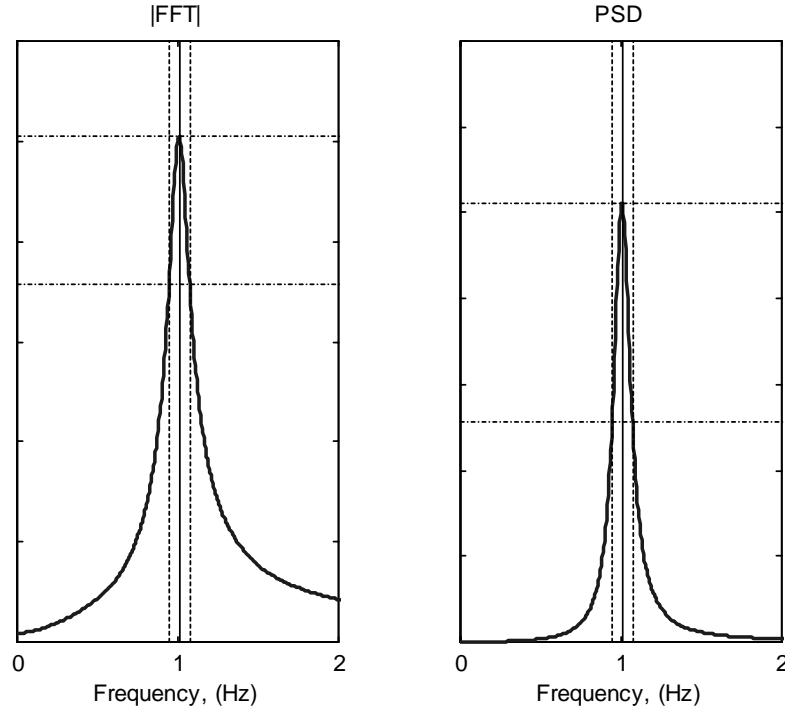


Figure 49 Logarithmic decrement results; large symbols are average values for each dynamic pressure

Frequency domain analysis is an important tool in identifying the modal characteristics of a system. By performing a Fourier transformation on a set of data, dominant frequencies of the system become evident. Damping can also be gleaned from data examined in this manner. The frequency of the system is determined by the maximum amplitude. Extracting the damping requires that one find the amplitude of the peak and then the frequencies where the amplitude is reduced by a factor of  $\sqrt{2}$ , these frequencies are referred to as the half power points. Figure 50 illustrates the quantities required to perform these calculations. This method was applied when data across the frequency range of concern could be obtained in a single time history, as in the case of the frequency sweep excitations.



**Figure 50 Frequency domain representations for extracting modal parameter data**

Figure 51 shows the Fourier transformation of the angle of attack data acquired at 1.52 psf for configuration # 2. This data was produced by exciting the system with a frequency sweep signal to the gust vanes. From this plot, the maximum amplitude was found to be 766 at a frequency of 7.3 (45.6 rads/sec). The half power points were found to be 6.75 Hz and 7.6 Hz. The difference between these frequencies, denoted  $\Delta\omega$ , is 0.85 Hz. The damping is calculated using Equation 23, resulting in a value of  $\zeta = 0.059$ , or an eigenvalue with real part  $-2.67$ .

$$\zeta = \frac{\Delta\omega}{2\omega} \quad \text{Equation 23}$$

This half power method was also utilized in real-time. A sine dwell excitation was sent to the gust vanes. The frequency of the excitation was tuned until the center frequency was determined. The amplitude was recorded and the half amplitude was determined. The frequency was then retuned to determine the half power points. In addition to recording these important values, time histories were recorded as the model was excited at each of these three frequencies. When these time histories were processed, they were found to be slightly inconsistent with the real-time determination of the half power points. The recorded and processed data was utilized in the final computations pertinent to the real-time half power method.

A variation of the Fourier transformation method uses the power spectral density function, PSD. The PSD is the normalized square of the Fourier transformation. The normalization allows frequency data extracted from different time length and sample rate data to be compared. Because the PSD is essentially the squared frequency content, the half power points are assessed at the peak amplitude/2. The right side of Figure 50 illustrates the required quantities to apply this technique. It is identical in calculation to the Fourier transform method.

This method was applied for velocities in the vicinity of divergence. Very near the dynamic pressure at which the system destabilized, sine dwell excitations had to be used to impart enough energy to the dynamic mode. Analysis of each time history produced a single point on a frequency domain plot.

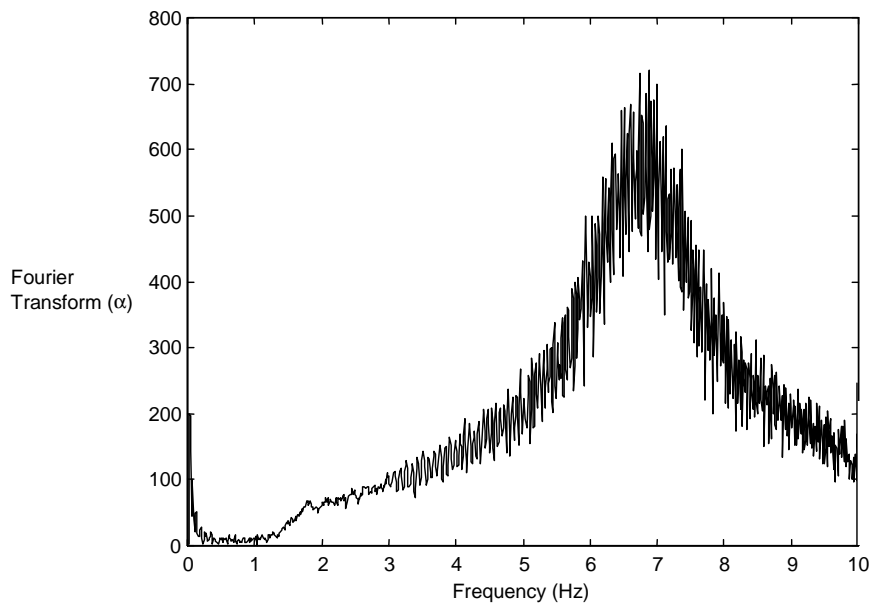


Figure 51 Amplitude of Fourier transformation of angle of attack; Configuration # 2, dynamic pressure 1.52 psf

The transfer function is another frequency domain interpretation which can be utilized to extract modal information. A transfer function requires an input, or excitation, signal in addition to the response signal. The actual excitation, the pressure field induced by the gust vanes on the wing is not available. The dynamic pressure of the tunnel, however, can be utilized in some sense as the excitation. Ewins<sup>3</sup> suggests plotting the real part of the transfer function as a function of frequency. This is done using sine dwell data to produce each point.

---

<sup>3</sup> Ewins, D. J., Modal Testing: *Theory and Practice*

The objective of the logarithmic decrement analysis and the frequency domain analyses were to determine the subcritical modal characteristics of the system as the dynamic pressure was increased towards divergence. The results of these techniques, applied to configuration #2, are summarized in Figures 52, 53 and 54. The damping and frequency information have been converted to the real and imaginary parts of an eigenvalue assuming that they were representative of a single mode.

Figure 52 shows the real part as a function of dynamic pressure for the different methods. This is indicative of the damping of the system. Seven sets of data are shown in the figure. All data sets indicate that the damping of the system is mainly due to the aerodynamics. The structural damping, indicated near zero airspeed is very small by comparison. All methods show the modal damping increasing as the dynamic pressure increases until divergence is reached. The individual curves are discussed below.

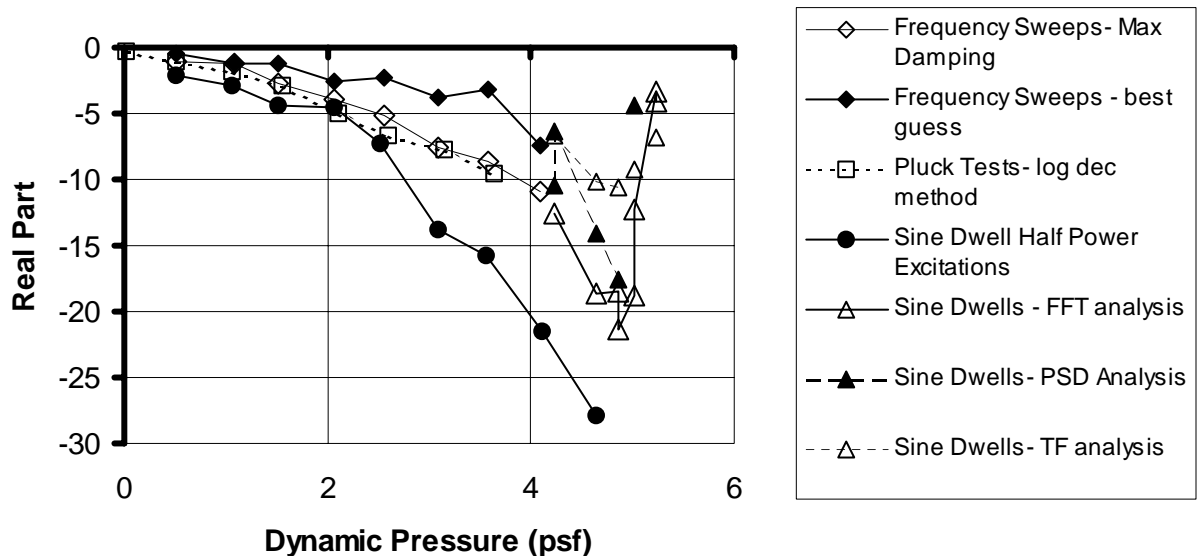


Figure 52 Real part of measured modal data as functions of dynamic pressure, Configuration # 2

The frequency sweep data was processed using the Fourier transform method. Because the frequency sweeps did not impart enough modal energy to the model near divergence, the results are only shown for dynamic pressures below 4.1 psf. These subcritical results show a monotonic increase in the magnitude of the real part as dynamic pressure increases. The data labeled as “maximum damping” corresponds to using the outside edges of the modal peak to determine the half power frequencies. The data labeled “best guess” corresponds to faring a curve through the scatter of the frequency data. The line

faring is approximately equivalent to processing a shorter time segment, which increases the Fourier transform frequency spacing. The “best guess” produced lowest values of damping across the dynamic pressure range. These values, which were more subjectively determined than the maximum damping values, produced more variability in the results. The “maximum damping” interpretation of the frequency sweep data lies nearly on top of the logarithmic decrement results.

The logarithmic decrement results, shown in the figure by open squares, are the average values at each dynamic pressure, which were shown in Figure 49. The logarithmic decrement results are the only results available for the air off condition. The results show very low structural damping; for this configuration it was measured as  $\zeta = 0.0053$ . Translated into the real part of an eigenvalue whose frequency is 49.5 radians/second, this corresponds to a real part of  $-0.26$ . A very orderly march to higher damping is charted by this data, which is available only at dynamic pressures below 3.6 psf.

The largest damping values were obtained by the real-time half power method. This data was taken up to 4.6 psf and provides a very smooth trend in the damping values.

In the vicinity of divergence, the sine dwell data was analyzed using the frequency domain methods. These analyses provide interesting trends. The Fourier transform results, shown by open triangles connected by a solid line, begin near where the frequency sweep data ended. The data continue to decrease until a dynamic pressure of 5 psf is exceeded. The values decrease as dynamic pressure is further increased. The power spectral density method and the transfer function method yield similar trends.

The frequency of the dynamic mode is shown in Figure 53. All methods show the same trend. The structural dynamic frequency, determined from time histories is 49.5 radians/second, (7.9 Hz). The frequency decreases as the dynamic pressure and thus the aerodynamic coupling increase. All results lie on top of each other except for the analyses of the sine dwell data. These data were acquired near divergence and have some scatter in the results. Regardless of the method, however, the frequency of the dynamic mode is determined to be not lower than 20 radians/second (3.2 Hz) at the divergence condition. The dynamic mode is clearly shown to persist at a non-zero frequency at the divergence condition.

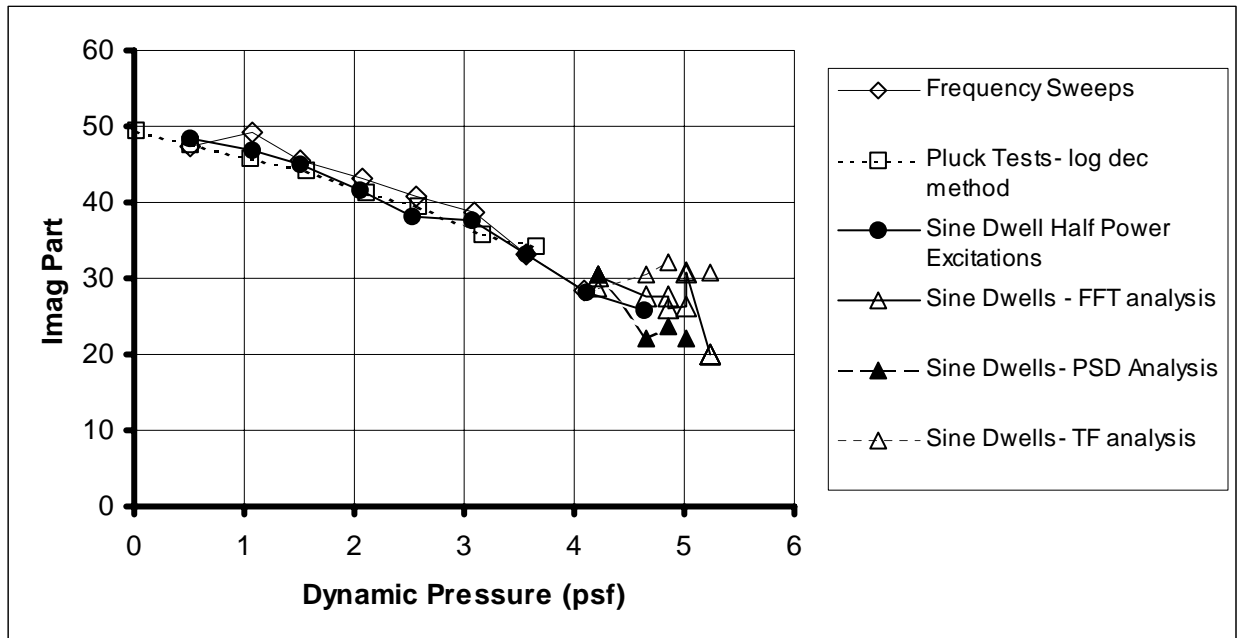


Figure 53 Imaginary part of measured modal data as functions of dynamic pressure, Configuration # 2

The subcritical modal data is also presented in a root locus format, Figure 54. The sine dwell results have been removed from this chart for purposes of clarity. The four traces shown, which are not individually identified, correspond to the pluck test results analyzed using the logarithmic decrement technique, the real-time half power results and the two interpretations of the frequency sweep data analyzed with the Fourier transform. All of the traces begin in the neighborhood of the air-off value at  $-0.26 + j49.5$  and migrate generally downward and to the left as dynamic pressure increases.

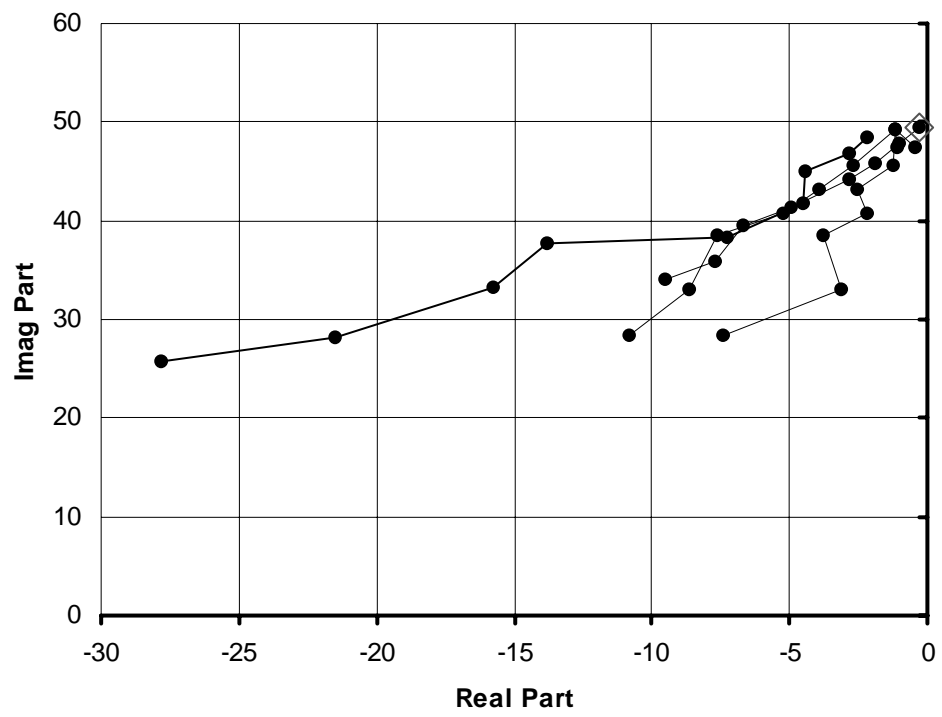


Figure 54 Root locus of experimental data as dynamic pressure is varied



### Configuration #1

The experimental data for wind tunnel model configuration # 1 is now presented. Configuration # 1 has the 1-inch diameter torsional spring and has the Tungsten trailing edge. The Tungsten trailing edge produces a higher torsional inertia than for the other configurations.

Divergence testing was conducted exactly as for configuration #2. The zero airspeed angle of attack was set as close to zero as possible. The divergence dynamic pressure was increased slowly until the angle of attack increased dramatically and suddenly, as shown in the time history of Figure 55. This was declared as the divergence dynamic pressure, 5.14 psf ( $246 \text{ N/m}^2$ ), which is nearly identical to the divergence condition for configuration #2. Based on analysis, this was the anticipated result.

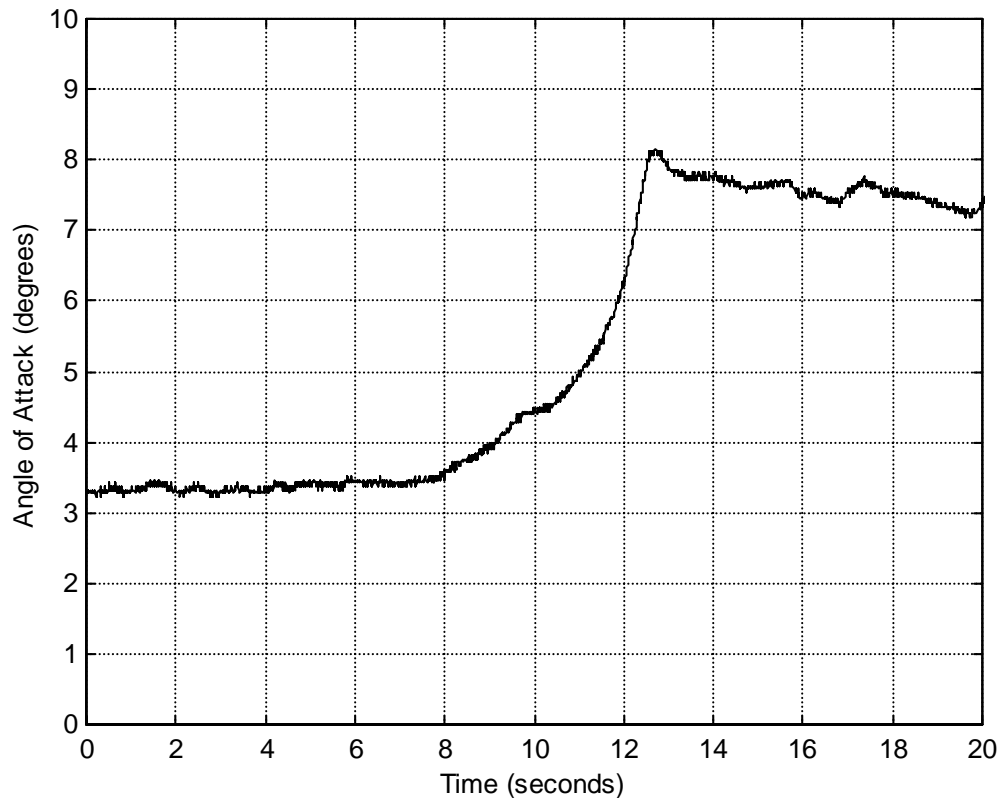


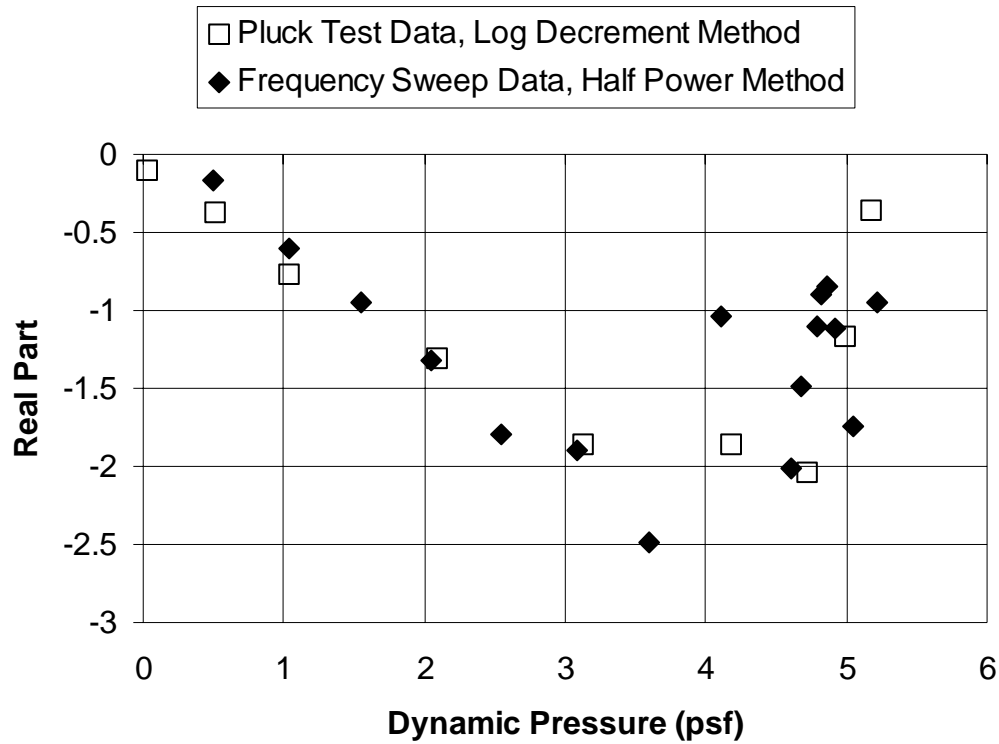
**Figure 55 Divergence of wind tunnel model configuration #1**

The subcritical methods of predicting divergence onset were each applied for this configuration. The data are similar to that presented for configuration #2 and are omitted here. The Southwell method was shown to be the most reliable prediction technique in analyzing the data for configuration #2. For configuration #1, a divergence condition of

5.1 psf was determined. This prediction required that data be known up to 3.13 psf, or 61% of the predicted divergence dynamic pressure. Using data at a higher dynamic pressure was found to detract from the accuracy of the prediction, as nonlinear effects began to influence the data.

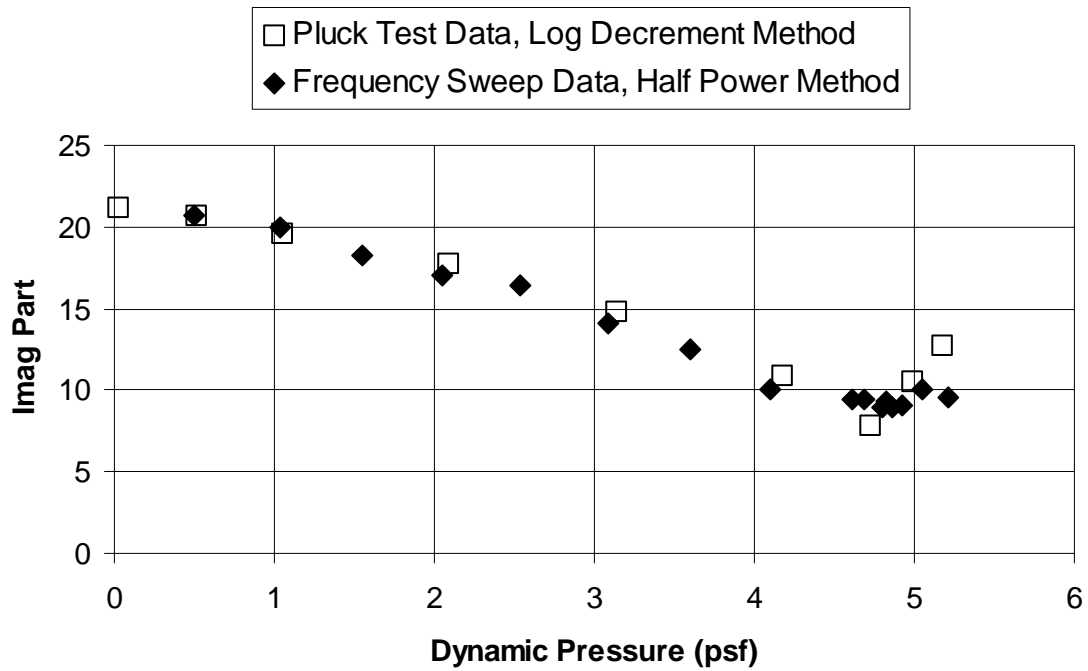
The subcritical modal characteristics of this configuration were determined, as for the previous configuration, as the dynamic pressure was increased towards divergence. The results of these techniques, applied to configuration #1, are summarized in Figures 56, 57 and 58. The damping and frequency information have been converted to the real and imaginary assuming that they were representative of a single mode. Only two methods were used to acquire and analyze the data for this configuration: the logarithmic decrement technique and the half power method applied to frequency sweeps.

Figure 56 shows the real part as a function of dynamic pressure. As with configuration #2, all data sets indicate that the damping of the system is mainly due to the aerodynamics. The logarithmic decrement results are shown in the figures by open squares. The air off results show very low structural damping; for this configuration it was measured as  $\zeta = 0.0046$ , a very low value by comparison. The half power method results are shown in the figures by solid diamonds. Both methods show the modal damping increasing as the dynamic pressure increases for subcritical conditions below 4 psf. The measured damping tends towards zero near the divergence dynamic pressure. This issue is further addressed in the discussion section of this paper.



**Figure 56 Real part of measured eigenvalues, Configuration # 1**

The frequency of the dynamic mode is shown in Figure 57. The structural dynamic frequency of the air off pitch mode was determined as 21.2 radians/second, (3.4 Hz). The logarithmic decrement and half power method show the same trends for increasing airspeed. The frequency decreases as the dynamic pressure and thus the aerodynamic coupling increase. The frequency of the dynamic mode is determined to be not lower than 7 radians/second (1.25 Hz) at the divergence condition. The dynamic mode is clearly shown to persist at a non-zero frequency at the divergence condition.



**Figure 57 Imaginary part of measured eigenvalues, Configuration # 1**

The subcritical modal data is also presented in a root locus format, Figure 58. The traces shown correspond to the pluck test results analyzed using the logarithmic decrement technique and the frequency sweep data analyzed with the Fourier transform. All of the traces begin in the neighborhood of the air-off value at  $-0.1 + j21.2$  and migrate generally downward and to the left as dynamic pressure increases. Near divergence, they resemble a left-to-right scribbling due to the uncertainty in determining the damping value.

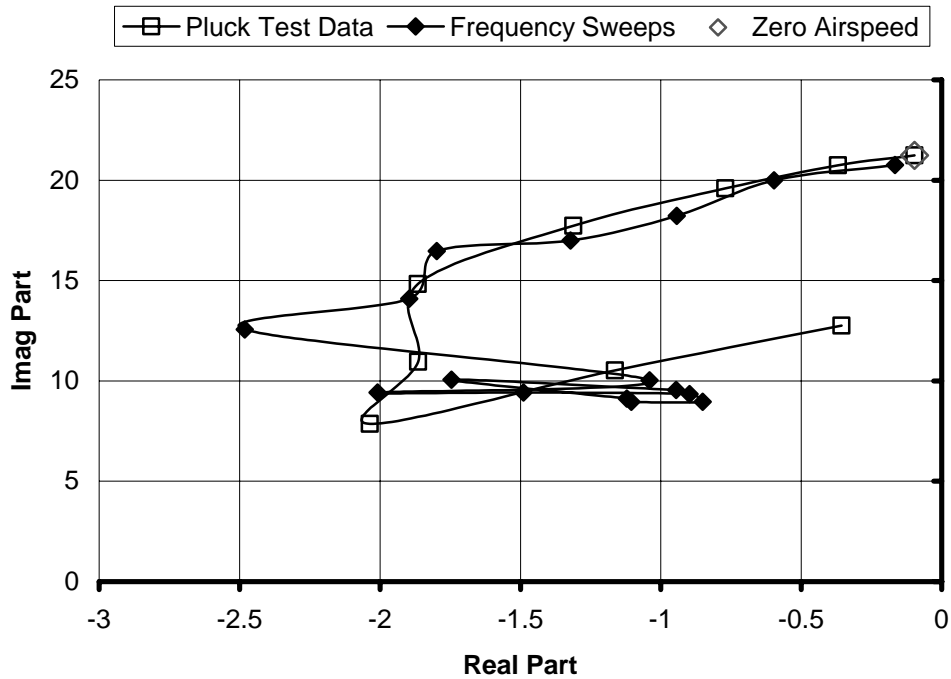
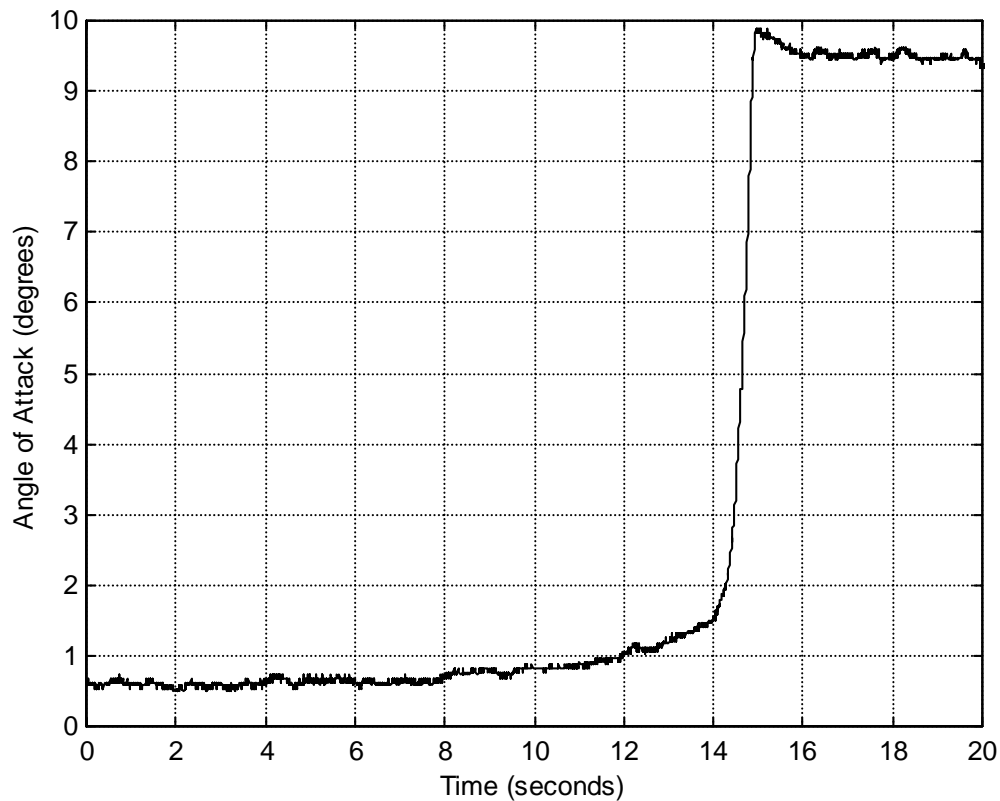


Figure 58 Root locus using experimental data, Configuration # 1

### Configuration #3

The experimental data for wind tunnel model configuration # 3 is presented next. Configuration # 3 has the  $\frac{3}{4}$  -inch diameter torsional spring and has the Plexiglass trailing edge. The inertial characteristics are identical to configuration #2. The torsional stiffness has been changed. As previously mentioned, changing the torsional stiffness is not anticipated to affect the dynamic characteristics of the system; in the analysis, the eigenvalue migration pattern remains identical. Although the nondimensional root locus remains the same, the dimensional natural frequency of the pitch mode increases as does the dynamic pressure which produces divergence.

Divergence testing was conducted exactly as for configuration #2. The zero airspeed angle of attack was set as close to zero as possible. The divergence dynamic pressure was increased slowly until the angle of attack increased dramatically and suddenly, as shown by the angle of attack time history, Figure 59. This was declared as the divergence dynamic pressure, 15.2 psf ( $730 \text{ N/m}^2$ ).



**Figure 59 Divergence of wind tunnel model configuration #3**

The subcritical methods of predicting divergence onset were each applied for this configuration. For this configuration, the Southwell method predicted a divergence condition of 15.8 psf. Although the prediction is fairly close to the divergence dynamic pressure observed directly, the nonlinear effects influenced this data more significantly than the previous configurations. The linear approximation to the data, utilized in the Southwell method, did not fit the data well. As the range of dynamic pressures included in the data set analyzed increased, the predicted divergence dynamic pressure also increased.

The subcritical modal characteristics of this configuration were determined, as for the previous configurations, as the dynamic pressure was increased towards divergence. The results of these techniques, applied to configuration #3, are summarized in Figures 60, 61 and 62. The damping and frequency information have been converted to the real and imaginary assuming that they were representative of a single mode. The damping and frequency traces presented are computed using the methods described pertaining to configuration #2.

Figure 60 shows the real part as a function of dynamic pressure. As with configuration #2, all data sets indicate that the damping of the system is mainly due to the

aerodynamics. The logarithmic decrement results are shown in the figures by open squares. The air off results show very low structural damping; for this configuration it was measured as  $\zeta = 0.0035$ . Results from the other various methods are shown by the symbols indicated in the legends. All methods show the modal damping increasing as the dynamic pressure increases. Additionally, the data show that the dynamic mode is stable throughout the range of dynamic pressure, including at the divergence condition.

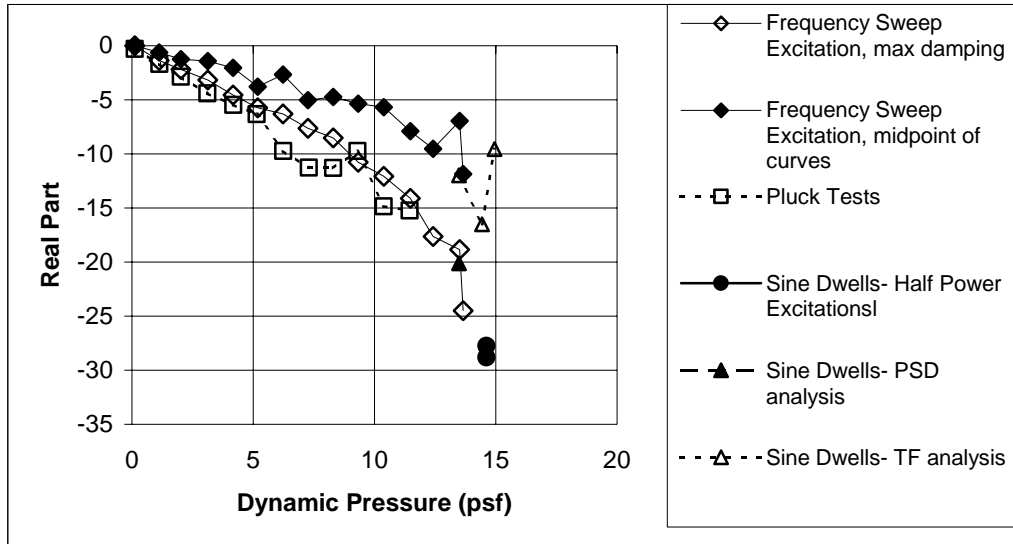


**Figure 60 Real part of measured eigenvalues, Configuration # 3**

The measured frequency of the dynamic mode is shown in Figure 61. The structural dynamic frequency of the air off pitch mode was determined as 87.15 radians/second, (13.9 Hz). All methods show the same trends for increasing airspeed. The frequency decreases as the dynamic pressure and thus the aerodynamic coupling increase. At divergence, the frequency of the dynamic mode is determined to be not lower than 36 radians/second (5.8 Hz) at the divergence condition. The dynamic mode is clearly shown to persist at a non-zero frequency at the divergence condition.

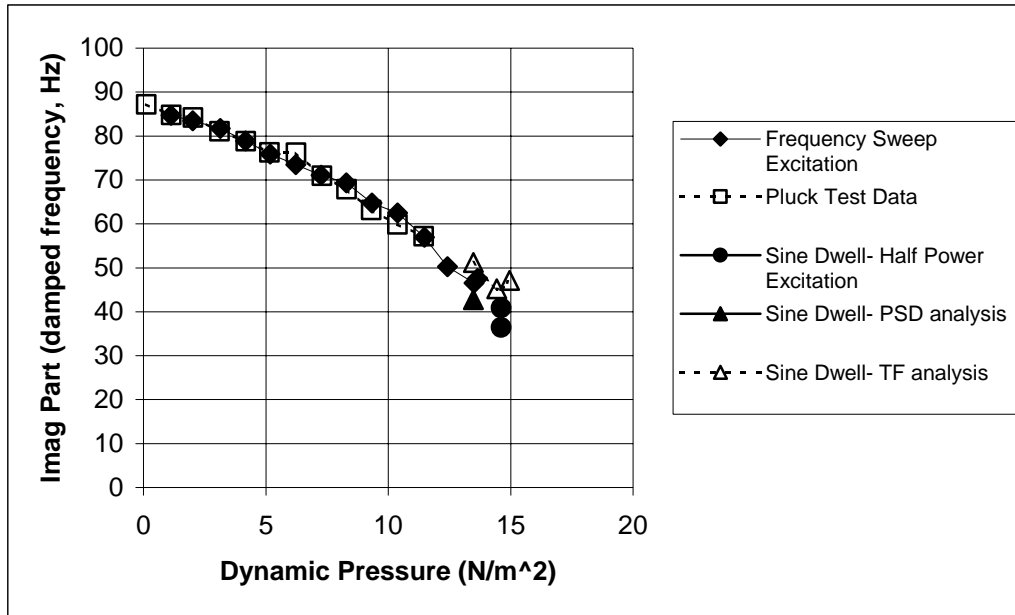


Figure 61 Imaginary part of measured eigenvalues, Configuration # 3

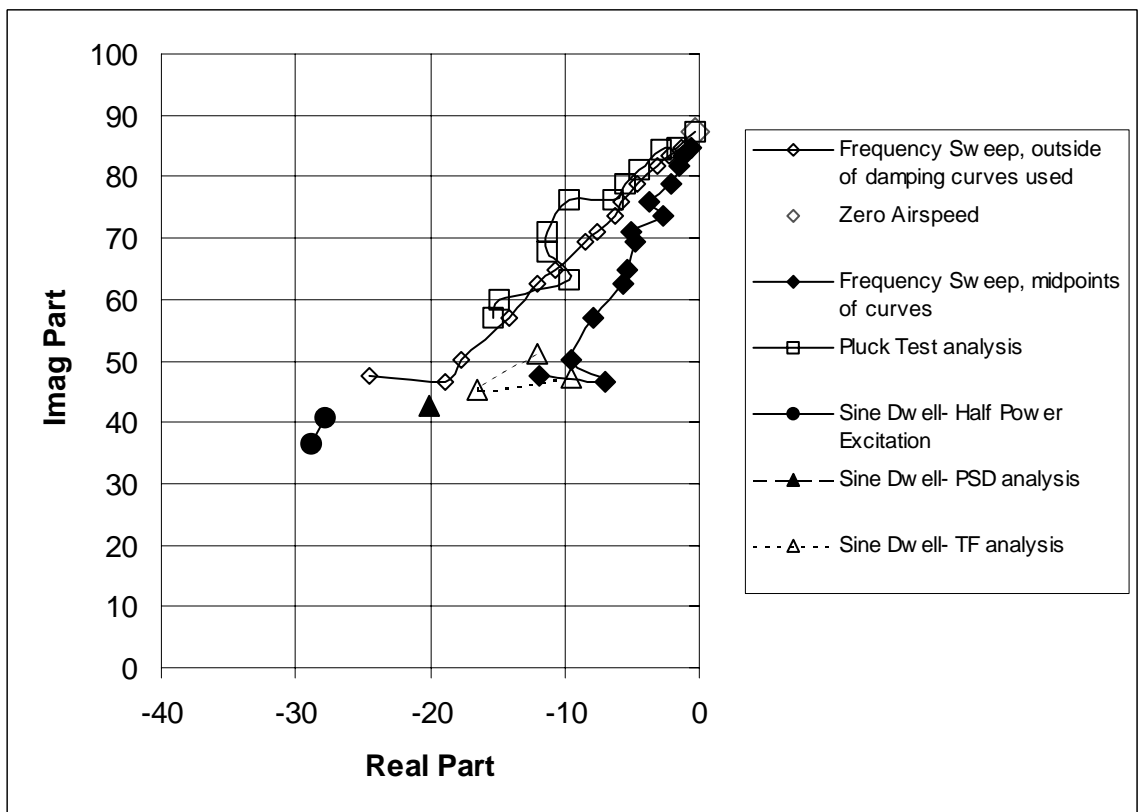


Figure 62 Root locus as a function of dynamic pressure, Configuration # 3



The subcritical modal data is also presented in a root locus format, Figure 62. All of the traces begin in the neighborhood of the air-off pitch mode eigenvalue,  $-0.3 + j87.1$ , and migrate generally downward and to the left as dynamic pressure increases. The trend shown in this figure is for the dynamic mode damping to increase dramatically in the neighborhood of the divergence dynamic pressure.

#### Hard Limit Instabilities

Time histories of each configuration at their respective divergence dynamic pressures have been presented, Figures 40, 55, and 59. Each figure shows that divergence resulted in the model sitting at an angle of attack where the airfoil has stalled. Data was acquired for velocities beyond these divergence conditions until further destabilization resulted in the model hitting the hard stops of the torsional spring. An example of this is shown for configuration #2 in Figure 63; the angle of attack time histories is presented. Beginning at 15.8 seconds into the time history, the character of the motion changes dramatically. Destabilization, characterized by the onset of this dramatic motion, occurred at a dynamic pressure of 5.59 psf ( $268 \text{ N/m}^2$ ).

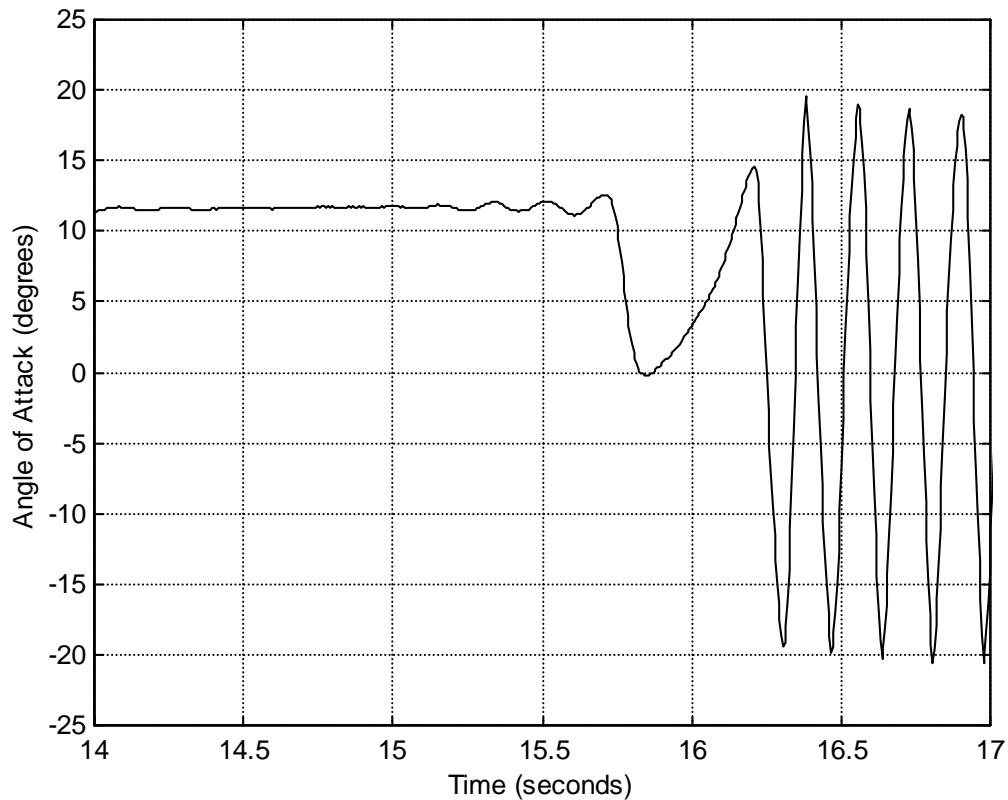


Figure 63 Hard limit instability encountered as dynamic pressure is increased, (Configuration #2)

A second example is shown in Figure 64; this data was acquired while the tunnel condition is held constant at 5.53 psf. This data shown in both time histories indicates

that the system destabilizes in a static sense, while dynamic motion persists. Examination of the data using an expanded scale, Figure 65, shows the dynamic oscillations of the torsional motion at 4.9 Hz as the system becomes statically unstable.

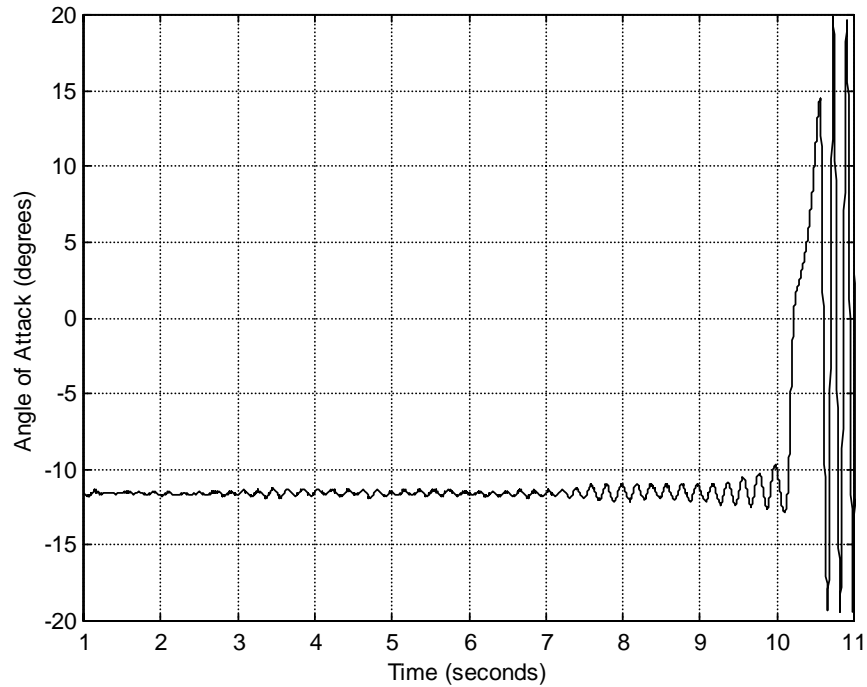


Figure 64 Divergence encountered while at constant dynamic pressure

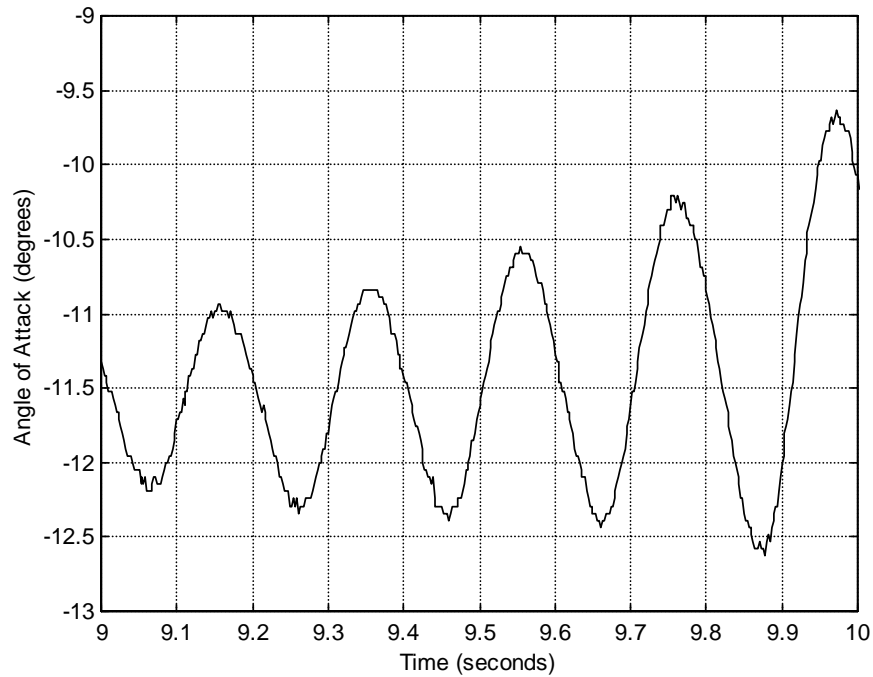
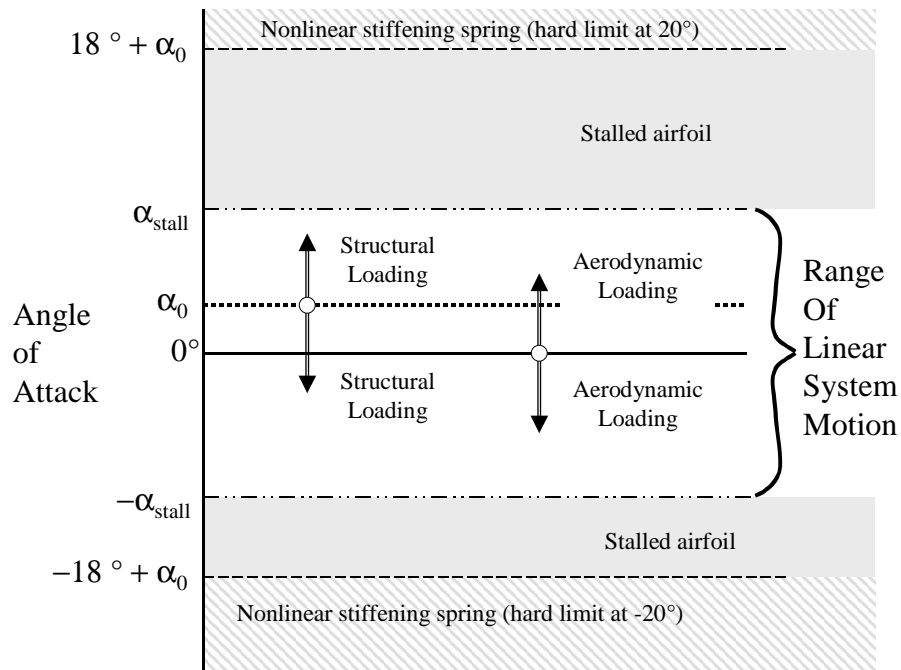


Figure 65 Divergence encountered while at constant dynamic pressure, expanded scale

The time histories presented above appear to have different character, despite the same configuration being at approximately the same condition. The system behavior has to be examined in the light of nonlinearities and regions of aerodynamic and structural loading and unloading. Figure 66 addresses this issue. Shown in the figure are regions where structural and aerodynamic nonlinearities affect the system. The torsional springs have been shown to have limits on the linear behavior at approximately  $18^\circ$ . This deflection limit is relative to the neutral position of the spring. Because the rigid angle of attack was set by rotating both ends of the barrel spring, the neutral position is equivalent to the rigid angle of attack,  $\alpha_0$ . All structural loading or unloading is relative to the neutral position of the spring. The system also appears to be subject to an aerodynamic nonlinearity as the flow separates and stall is encountered. Stall initiates at an angle substantially below the structural limit; effects were observed as low as  $8^\circ$ . The stalled airfoil stabilizes at angles as high as  $11\frac{1}{2}^\circ$ . Aerodynamic loading or unloading is relative to the symmetric position of the wing,  $0^\circ$ . These regions determine and explain the behavior of the system observed in the time histories.



**Figure 66 Regions of behavior for the airfoil**

Consider the time history shown in Figure 55. Prior to the destabilization, shown to begin at 15.7 seconds, the linear system has already diverged. Because the airfoil is sitting at approximately  $11\frac{1}{2}^\circ$ , aerodynamic stall has effectively decreased the lift curve slope; in a simplistic static sense, this can be thought of as a decrease in (negative) aerodynamic stiffness. A decrease in negative aerodynamic stiffness raises the dynamic pressure at which the system destabilizes. Thus the nonlinear system appears

stable at a dynamic pressure which exceeds the linear system divergence condition. At 15.7 seconds, the system possesses enough aerodynamic energy such that the nonlinear system becomes unstable. Because the airfoil is stalled only as it oscillates in one direction (in this case, toward larger angles), the motion is forced towards zero. As the system destabilizes, the airfoil reenters the linear aerodynamic range. The airfoil has enough momentum to approach zero, which is the aerodynamically and structurally unloaded position, since the airfoil is at zero degrees rigid angle of attack. The system is now at an unstable equilibrium point. Pursuant motion may be to either the positive or the negative side. In the case of Figure 55, the linear range system diverges in the same direction that it just came from. In the case of Figure 64, the system diverges in the opposite direction. In the second case, the system may have been at a higher energy level, the system possessing more momentum as it unloaded, overshooting the neutral stability point and encouraging divergence in the opposite direction. In both of these cases, when the system hits the nonlinear region again, sufficient energy has been added to the system so that the hard stops of the torsional spring are hit; oscillations from one stop to the other ensue.

Similar data is presented pertinent to configuration # 1. For this configuration, the onset of the instability is gentler than that observed for configuration #2. Additionally, the system does not hit the hard stops of the spring until after several oscillations from one nonlinear range to the other.

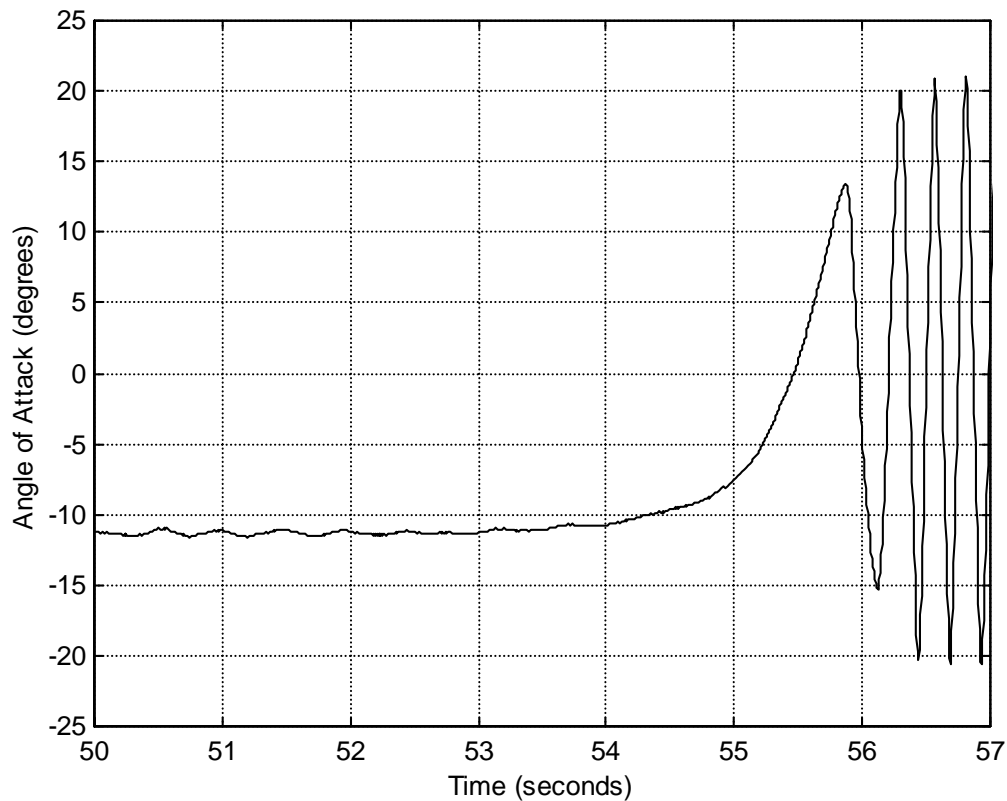


**Figure 67 Nonlinear system divergence for configuration 1 at constant dynamic pressure**

Results for configuration #3 are shown in Figure 68. This are particularly interesting data because the nonlinear system is barely unstable and appears to damp slightly instead of gaining energy with each oscillation. Prior to 15 seconds, the airfoil is sitting at  $11\frac{1}{2}^\circ$  angle of attack. The dynamic mode oscillations grow in amplitude, pushing the airfoil deeper into the stall region. At 15.75 seconds, the system destabilizes in a static sense. The angle of attack changes monotonically until the nonlinear aerodynamic region on the negative side is encountered. The nonlinear system diverges again to the positive side and then returns again to the negative side. Unlike in the previous cases, the system does not have enough momentum to oscillate to the hard stops of the spring. Instead, the motion damps slightly. By the second time the system hits the negative side, the momentum is no longer sufficient to propel the airfoil through zero. As in the first case discussed, it is now equally likely to diverge to either the positive or the negative side. Returning to the negative side, the airfoil settles again at the stalled angle of  $11\frac{1}{2}^\circ$ .

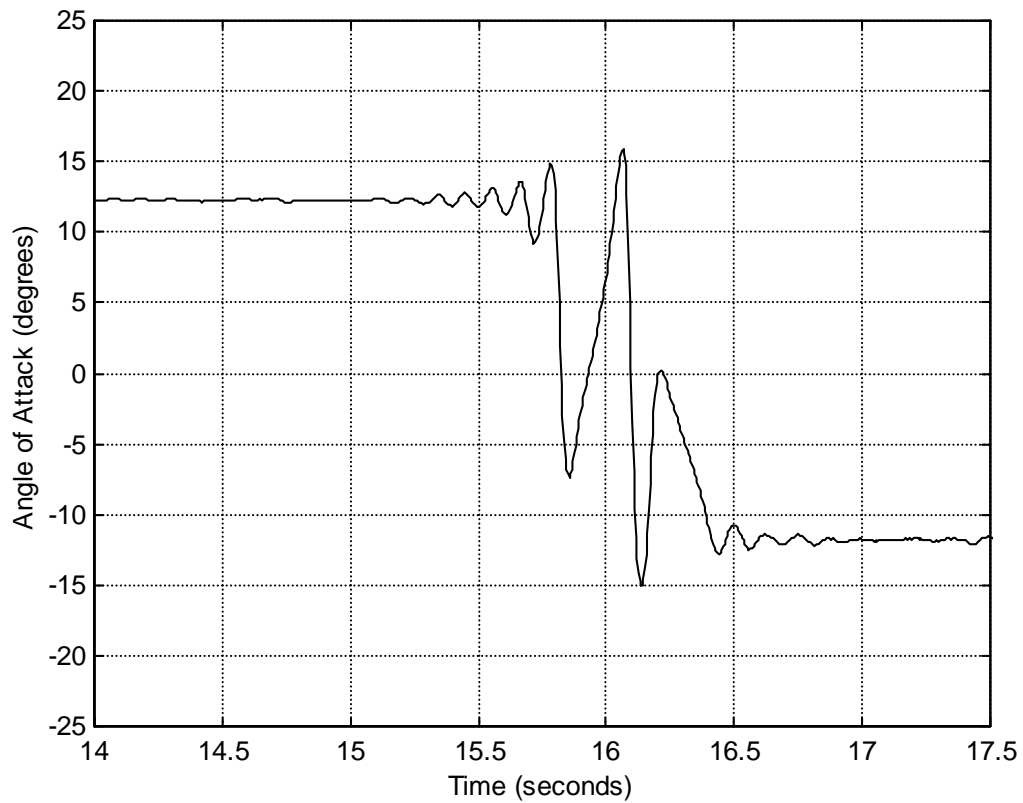


**Figure 68 Nonlinear system divergence for configuration 3, tab 976, as velocity is slowly increased until divergence condition**

### **Dynamic mode characteristics at the instability condition**

The time history data presented previously pertained to the system when the rigid angle of attack was very close to zero degrees. The characteristics of the system at the instability condition appear different when the airfoil is set at a substantial nonzero rigid angle of attack. Data is presented in Figure 69 as the configuration #2 destabilizes at three different rigid angles of attack.

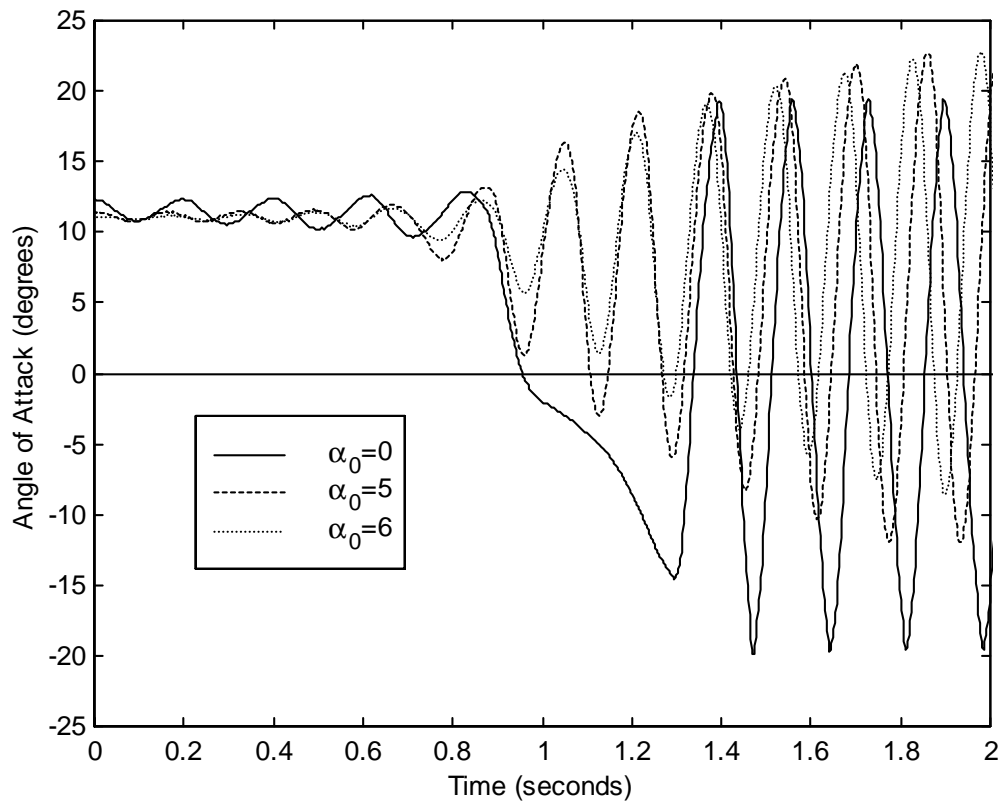


Figure 69 Instability encountered for several values of rigid angle of attack, Configuration #2

The oscillatory behavior appears in the data more prominently for the non-zero rigid body angles of attack,  $5^\circ$  and  $6^\circ$  versus  $0^\circ$ . It is important to note that setting the rigid angle of attack at a non-zero angle causes the system to diverge at a lower dynamic pressure. Each of the lines plotted in Figure 69 is for a different dynamic pressure. The data at  $5^\circ$  angle of attack was acquired at a dynamic pressure of 3.13 psf. The modal frequency is measured as 6.0 Hz. For the same dynamic pressure, the dynamic mode frequency of the system at  $0^\circ$  was measured between 5.7 and 6.1 Hz, depending upon the data reduction technique. The frequency of the system at instability for the  $6^\circ$  rigid angle of attack is 6.2 Hz. The dynamic pressure is 2.55 psf. At a dynamic pressure of 2.55 psf, the  $0^\circ$  rigid angle of attack data yielded a frequency between 6.3 and 6.5 Hz.

The nonzero angle of attack data must be considered in light of the nonlinear regions discussed above. There is additional complexity in the system because the structure's equilibrium point is different than the aerodynamic stall equilibrium point. Consider the above data for a rigid angle of attack of  $5^\circ$ . The unstable behavior initiates at approximately 0.5 seconds as the dynamic mode oscillations grow in magnitude. As time progresses, the oscillations are shown to cross the zero angle of attack, without moving into the nonlinear effects on the negative side, and then returning to the positive stalled

side. This behavior exists due to the disparity in the structural and aerodynamic neutral stability points. As the airfoil oscillates towards  $5^\circ$ , the system is unloading structurally and aerodynamically. Once it passes  $5^\circ$ , it is becoming structurally loaded such that the torsional spring force acts to pull it back towards  $5^\circ$ . The aerodynamic forces are still dissipating until the system oscillates beyond  $0^\circ$ . This data set was acquired substantially below the instability dynamic pressure of the system at  $0^\circ$  rigid angle of attack. The structural restorative moment capability exceeds the aerodynamic moment imparted at the low angles of attack. The system is therefore pulled towards the structural equilibrium point,  $5^\circ$ . The system oscillates back to the stall angle of attack as a larger aerodynamic moment is produced by the airfoil at a now larger angle of attack.

Similar data is presented for configuration #1 and #3 in Figure 71 and Figure 70, respectively.

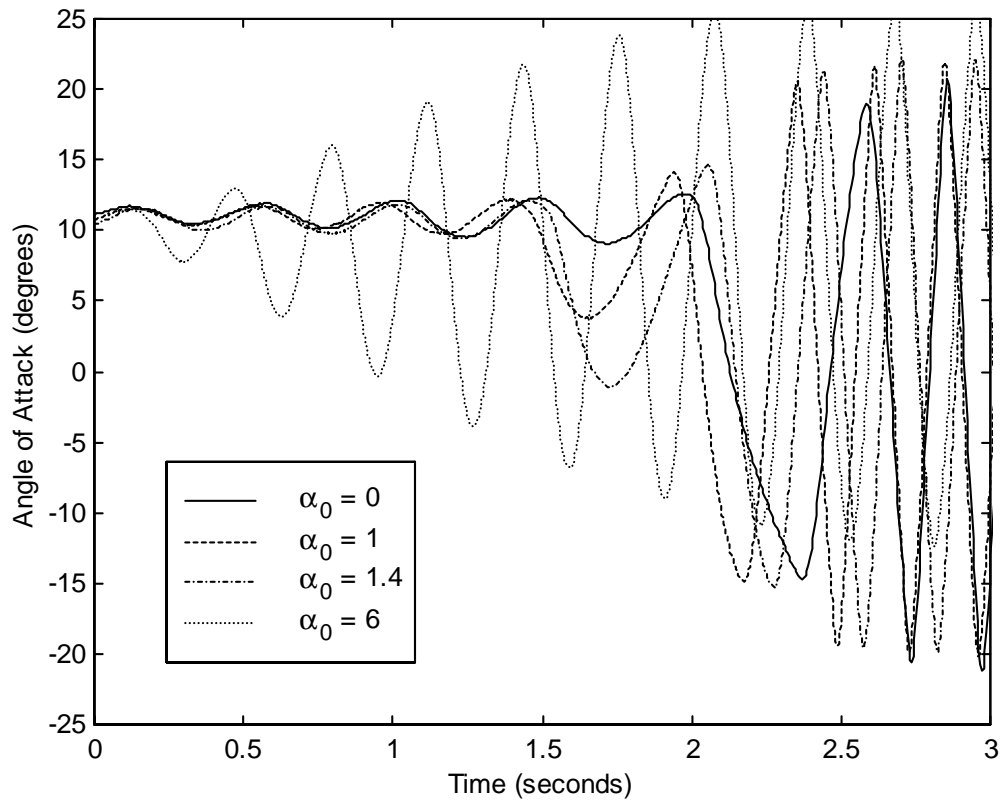


**Figure 70** Instability encountered for several values of rigid angle of attack, each at a different dynamic pressure, Configuration #1



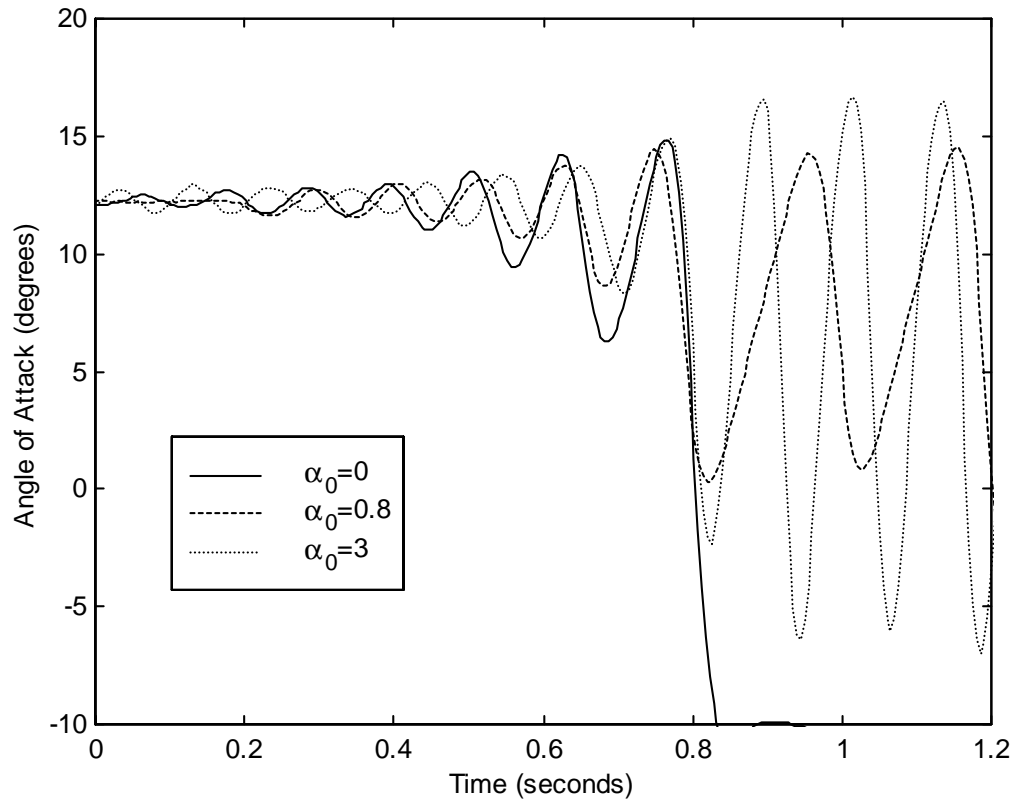


**Figure 71** Instability encountered for several values of rigid angle of attack, each at a different dynamic pressure, Configuration #3

Frequency ratios for the wind tunnel model configurations are compared in Table 13.

Config #	$\omega_\alpha$ (air off) ( $f_\alpha$ , Hz)	$\omega_D$ ( $f_D$ , Hz)	$\omega_D / \omega_\alpha$	$\omega_H$ (at hard instability condition) ( $f_D$ , Hz)	$\omega_H / \omega_\alpha$	$\frac{mass_{TrailingEdge}}{mass_{Total}}$
1	21.4 (3.4)	8.9 (1.42)	0.42	15.7 (2.5)	0.74	0.56
2	49.5 (7.9)	22.0 (3.5)	0.44	30.8 (4.9)	0.62	0.01
3	88.0 (14.0)	45.2 (7.2)	0.51	56.5 (9.0)	0.64	0.01

**Table 13** Frequency ratios of experimental data

## Discussion of Experimental Methods

### **Divergence Prediction Methods**

Divergence onset determination using the load monitoring method requires that data be acquired very near divergence. Interpretation of data taken well below divergence and examined in this way does not easily yield the divergence condition. When using load monitoring, it appears best to use a small, nearly zero rigid angle of attack. The load is proportional to the elastic increment on angle of attack. This quantity is itself an amplification of the rigid angle of attack. The amplification factor becomes very large, theoretically goes to infinity, near divergence. As observed in the data for larger rigid angles of attack, there is a steady, gradual rise in the moment. This is the effect of applying an increasing dynamic pressure to a lifting surface at a non-zero angle of attack.

### **Modal Characteristics Determination Methods**

Several methods were utilized to identify modal characteristics. It is not possible to completely isolate a single aeroelastic mode's behavior in an experimental setting. Thus, the measurements of the dynamic mode properties contain some content from the static mode of the system.

The logarithmic decrement method is a simple way to calculate damping for systems where the damping is low. The time histories produce consistent values in these cases, where many cycles can be included inherently in the data processing. The air off data presented is a good example of this situation. More highly damped systems, however produce a limited number of oscillations. In the case of the plexiglass trailing edge configurations, there were often only one or two cycles of decaying motion to analyze, even at very low airspeeds.

It was difficult to extract information using the logarithmic decrement method in the vicinity of divergence. Taking several data sets or using different segments of a time history produced very different values of damping. The overall system response is a combination of all of the system modes. Thus the time history's damping is not a modal damping. Logarithmic decrement results can only be interpreted as modal damping if a single mode is dominating the response. Near divergence, it is speculated that two modes are contributing- a stable dynamic mode and a barely stable real mode. The calculated damping could be the damping of one mode or the other, or more likely could indicate a value in between them.

To utilize the logarithmic decrement technique, a disturbance must be applied to the mode. As divergence is neared, the force with which a pluck is administered must be reduced. Up to a certain dynamic pressure a very severe pluck can be used. This produces more usable cycles of data. In these subcritical data sets, it is speculated that the dominant damping effect is produced by the dynamic mode. Very near the

divergence condition, it was difficult to pluck the model without destabilizing the system. The dominant damping effect here is speculated to be that of the static mode of aerodynamic origin which is very near instability.

The analysis of the logarithmic decrement data taken alone might lead one to consider this a case of single degree of freedom flutter, where the dynamic mode destabilizes. The additional data and analyses, however, do not support this interpretation.

An advantage to analyzing the data with frequency domain techniques is that the transformation process sorts the information by frequency, separating the information by mode. The damping and frequency information pertinent to one mode is distinct from the others, as long as the modes are well separated. The main driver in testing configuration 3 was to raise the frequency of the dynamic mode at divergence so that the peak could be fully distinguished. The modal frequency of configurations 1 and 2 was low enough near divergence, that it is speculated that there could be substantial “leakage” from the static information into the of the dynamic mode measurements.

The frequency domain techniques encountered difficulties near divergence. At velocities well below divergence, a frequency sweep to the gust vanes provided the system with sufficient excitation to give clean peaks in the frequency domain. There are several issues to overcome in applying these methods near divergence. The first is how to impart enough energy into the dynamic mode of the system. The frequency sweeps were effective to a dynamic pressure that is very near the soft or linear divergence condition. Above this, sine dwell excitations had to be employed.

In doing the sine dwells, the tunnel condition had to be maintained over along period of time. Tunnel drift is thought to have produced a change in dynamic pressure, affecting the consistence of a set of sine dwell data. Changes in the dynamic pressure affect not only the amplitude of the response at a given frequency, but also shifts the modal frequency. Inability to hold tunnel condition is thought to be partly responsible for the data scatter associated with analysis of the sine dwell data.

An additional issue with the frequency domain results is extraction of the important parameters from the plot. The faring of the line through the data is subjective and becomes more crucial for highly damped systems.

## CHAPTER FOUR

### COMPARISON OF ANALYSIS AND EXPERIMENT

The analytical and experimental results, previously presented in this paper, are compared for each of the three wind tunnel model configurations. The subcritical eigenvalues of the dynamic modes are compared, as well as divergence conditions.

Configuration # 2, which is described in detail in Table 4, had the lower pitch stiffness and the lower pitch inertia. This configuration is considered first. The imaginary part, frequency, of the eigenvalue associated with the dynamic mode is plotted as a function of dynamic pressure in Figure 72. Analytical results are indicated by the small “x’s”, while experimental data are indicated by the larger symbols. Experimental data acquired using different methods are represented by the different symbols. Five modes are shown from the analysis. Two complex aerodynamic modes are shown; they originate at low frequency and spring rapidly to a high frequency. They do not play a role in determining either the stability nor the subcritical characteristics of the dynamic mode of interest. Two real modes that originate in the aerodynamic model are overplotted on the real axis. The mode which originates as the structural dynamic mode starts at the natural frequency of the torsion mode, 49.5 rads/sec and migrates to a lower frequency as the aeroelastic coupling comes into play. The analytical results and experimental data agree very well. Both analysis and experiment indicate that the frequency of the dynamic mode is substantially non-zero at the divergence condition. The divergence dynamic pressure predicted by the analysis is 4.6 psf. The wind tunnel model diverged at 5.1 psf and hit the hard limit instability at 5.6 psf.

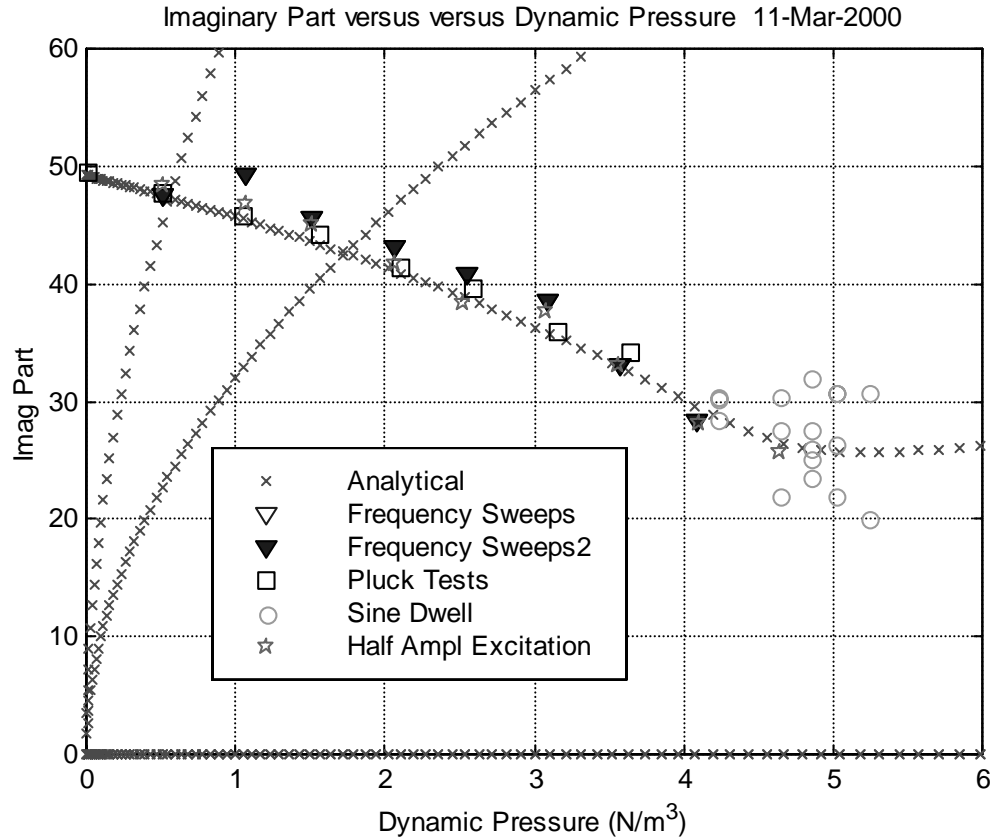


**Figure 72 Comparison of analytical and experimental results for configuration # 2, frequency of system behavior as a function of dynamic pressure**

The real part, indicative of the damping, of the dynamic mode eigenvalue is plotted as a function of dynamic pressure in Figure 73. Five modes are shown from the analysis. Two of the modes originate at zero and drop rapidly. These are complex aerodynamic modes which become very highly damped. The mode which destabilizes is a real mode which originated in the aerodynamic model. The mode which originates as the structural dynamic mode starts near zero and monotonically decreases throughout the dynamic pressure range presented. The fifth mode present from the analysis originated as the second real aerodynamic eigenvalue. The subcritical trends in the experimental curves follow the trend of the dynamic mode. Near divergence, between 4 and 5.6 psf, there is substantial scatter in the experimental determination of damping. The damping values generally lie between the analytical value for the dynamic mode and the stable aerodynamic mode. While the experiment and analysis are not in perfect quantitative agreement, both indicate that the dynamic mode is stable at the divergence dynamic pressure.

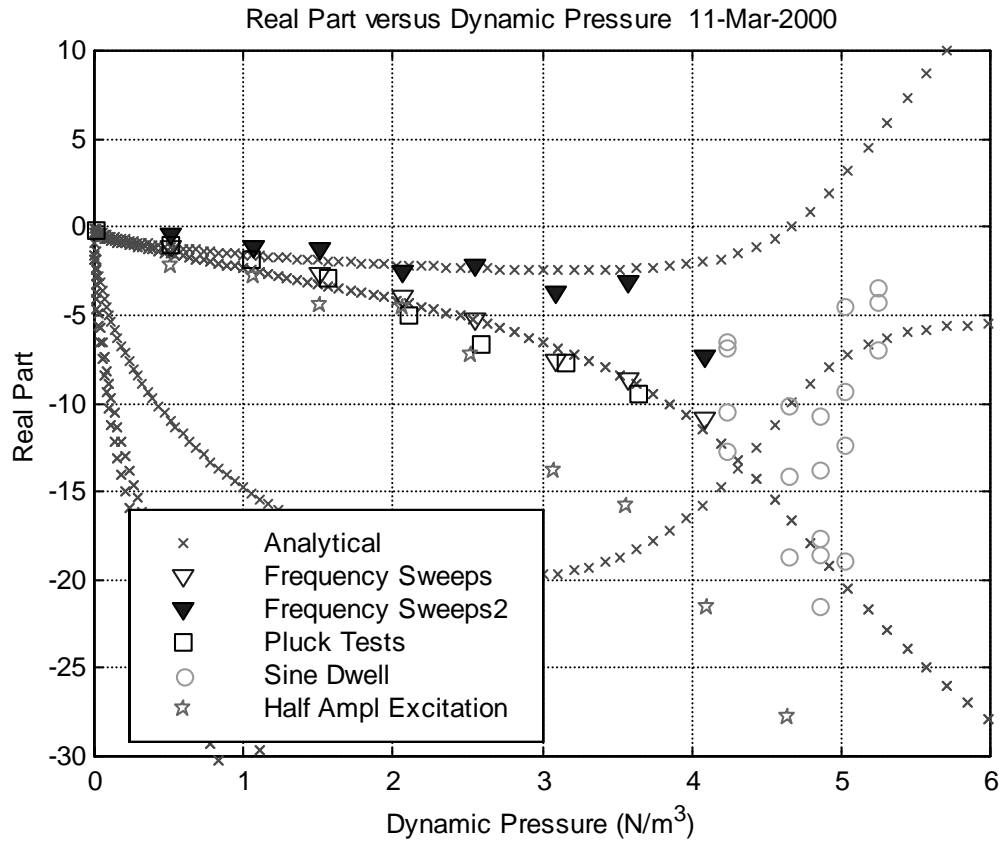


**Figure 73 Comparison of analytical and experimental results for configuration # 2, damping behavior as a function of dynamic pressure**

The real and imaginary parts are combined in a root locus plot in Figure 74. For clarity, the complex aerodynamic modes have been removed from the chart. As the reduced velocity or dynamic pressure increases, the data progress generally downward and to the left.

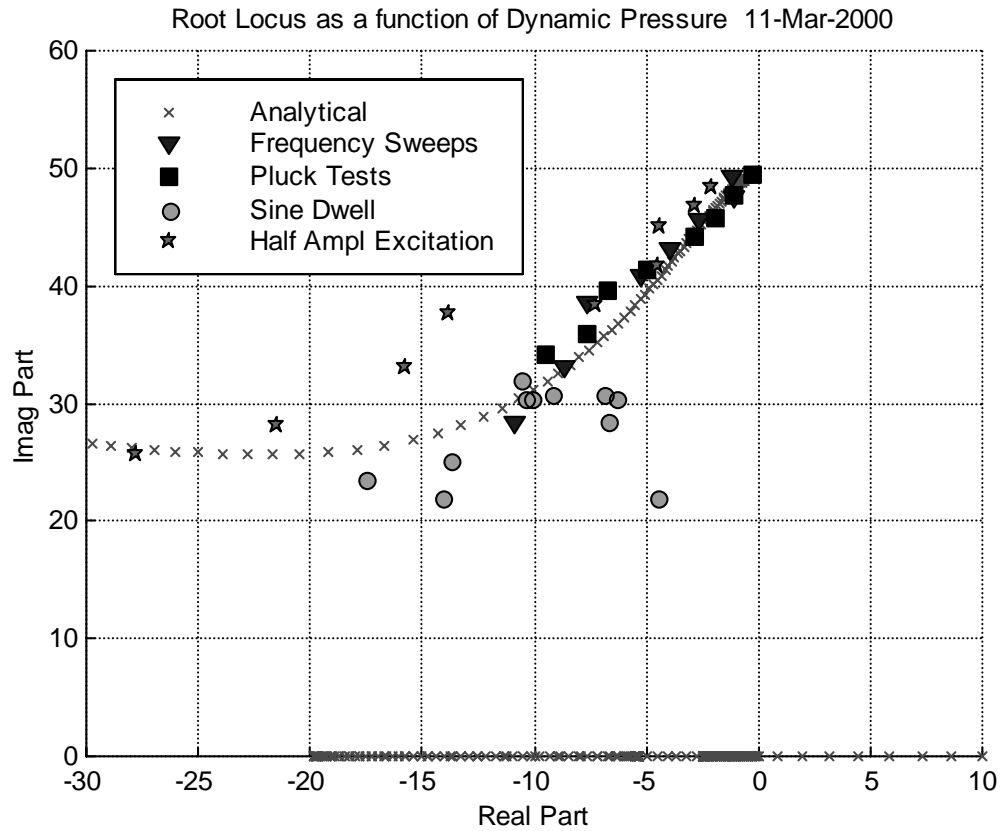


**Figure 74 Comparison of analytical and experimental results for configuration # 2, root locus as dynamic pressure is varied**

The dynamic pressure and frequency results for configuration # 2 are summarized in Table 14.

	Dynamic Pressure	Frequency	
	(psf)	(rads/sec)	(Hz)
Analysis:			
Air-off characteristics	0	49.5	7.9
Divergence	4.6	26.4	4.2
Experiment:			
Air-off characteristics	0	49.6	7.9
Linear System Divergence	5.1	22.0	3.5
Hard Limit Instability	5.6	30.8	4.9
Southwell method results	5.5		

**Table 14 Comparison of analysis and experimental values for configuration # 2**

Configuration # 1 is considered next. Again, the analytical results and experimental data agree well. In the vicinity of the divergence dynamic pressure, the experimental frequency increases, departing from the analytically predicted frequency. Both analysis and experiment indicate that the frequency of the dynamic mode is substantially non-zero at the divergence condition. The divergence dynamic pressure predicted by the analysis is 4.6 psf. The wind tunnel model diverged at 5.1 psf and hit the hard limit instability at 5.5 psf.

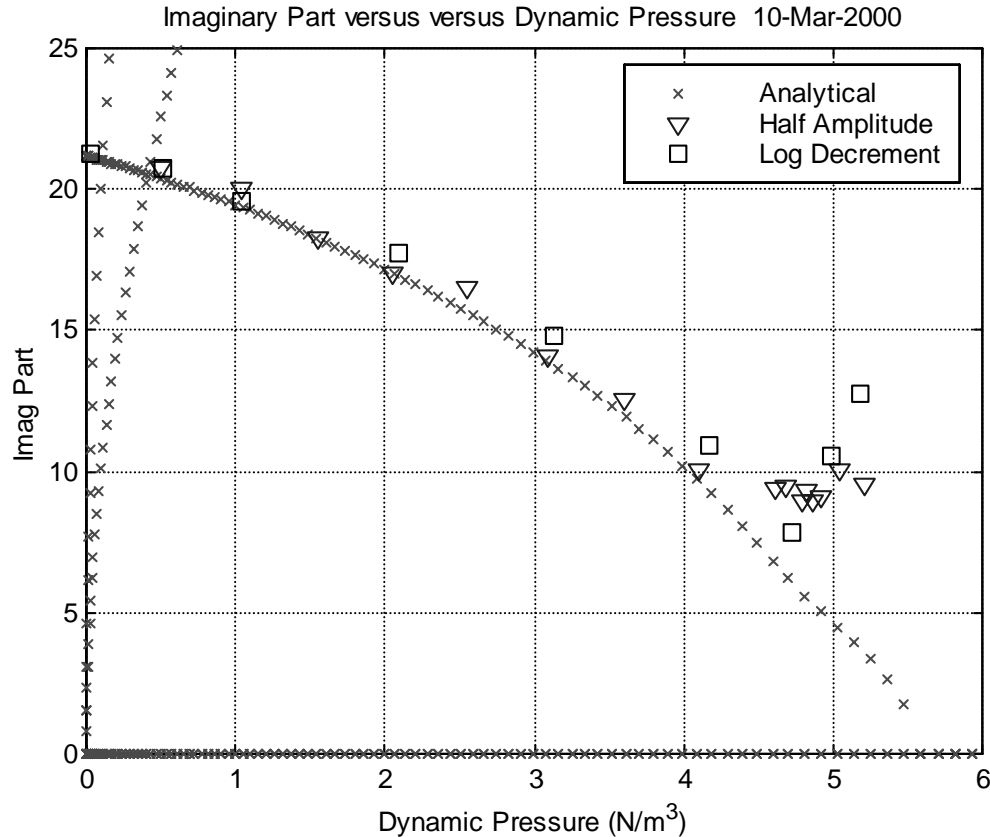
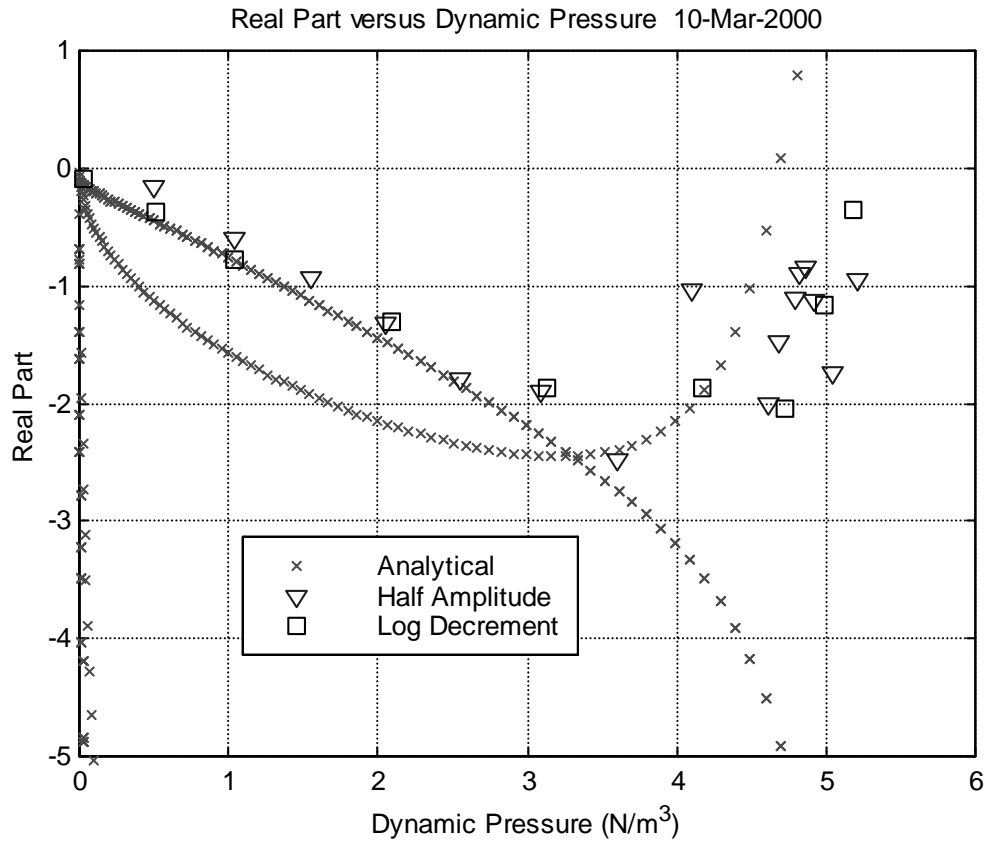


Figure 75 Comparison of analytical and experimental results for configuration # 1, imaginary part as a function of dynamic pressure

The real part, indicative of the damping, of the dynamic mode eigenvalue is plotted as a function of dynamic pressure in Figure 76. For subcritical conditions below 4 psf the shapes of the experimental data agree very well with the analytical dynamic mode. Near divergence, between 4 and 5.6 psf, the measured damping values appear to follow the real root of aerodynamic origin, which destabilizes.





**Figure 76 Comparison of analytical and experimental results for configuration #1, real part as a function of dynamic pressure**

The real and imaginary parts are combined in a root locus plot in Figure 77. As the reduced velocity or dynamic pressure increases, the data progress generally downward and to the left.

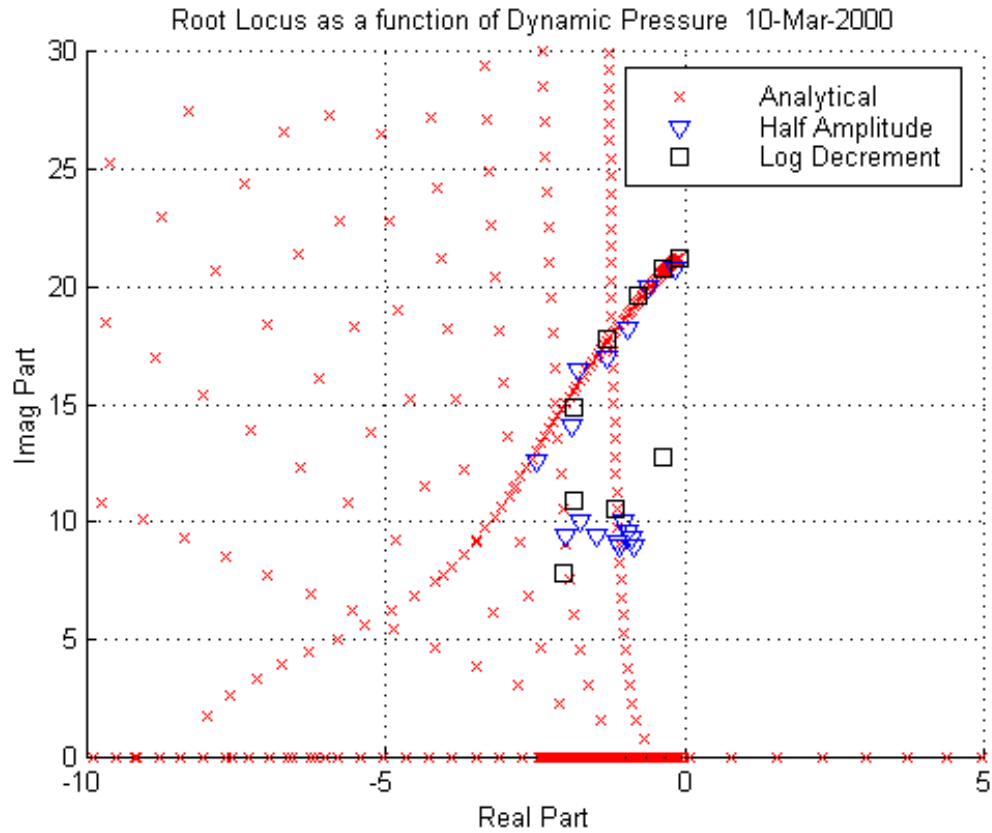


**Figure 77 Comparison of analytical and experimental results for configuration #1, root locus as a function of dynamic pressure**

The dynamic pressure and frequency results for configuration # 1 are summarized in Table 15.

	Dynamic Pressure (psf)	Frequency	
		(rads/sec)	(Hz)
<b>Analysis:</b>			
Air-off characteristics	0	21.2	3.4
Divergence	4.6	6.2	1.0
<b>Experiment:</b>			
Air-off characteristics	0	21.4	3.4
Linear System Divergence	5.1	9.0	1.4
Hard Limit Instability	5.5	13.2	2.1
Southwell method results	5.1		

**Table 15 Comparison of analysis and experimental values for configuration # 1**

Configuration # 3 is now examined. The frequency results, shown in Figure 78 demonstrate the best agreement between theory and experiment of the three configurations. The analytical results and experimental data lie on top of one another throughout the dynamic pressure range, except right at divergence. In the vicinity of the divergence dynamic pressure, there is a small amount of scatter in the measured frequencies. The experimental values mainly fall slightly below the analytical calculations. Both analysis and experiment indicate that the frequency of the dynamic mode is approximately 45 radians/second (7.2 Hz) at the divergence condition. The divergence dynamic pressure predicted by the analysis is 14.3 psf. The wind tunnel model diverged at 15.2 psf and hit the hard limit instability at 16 psf.

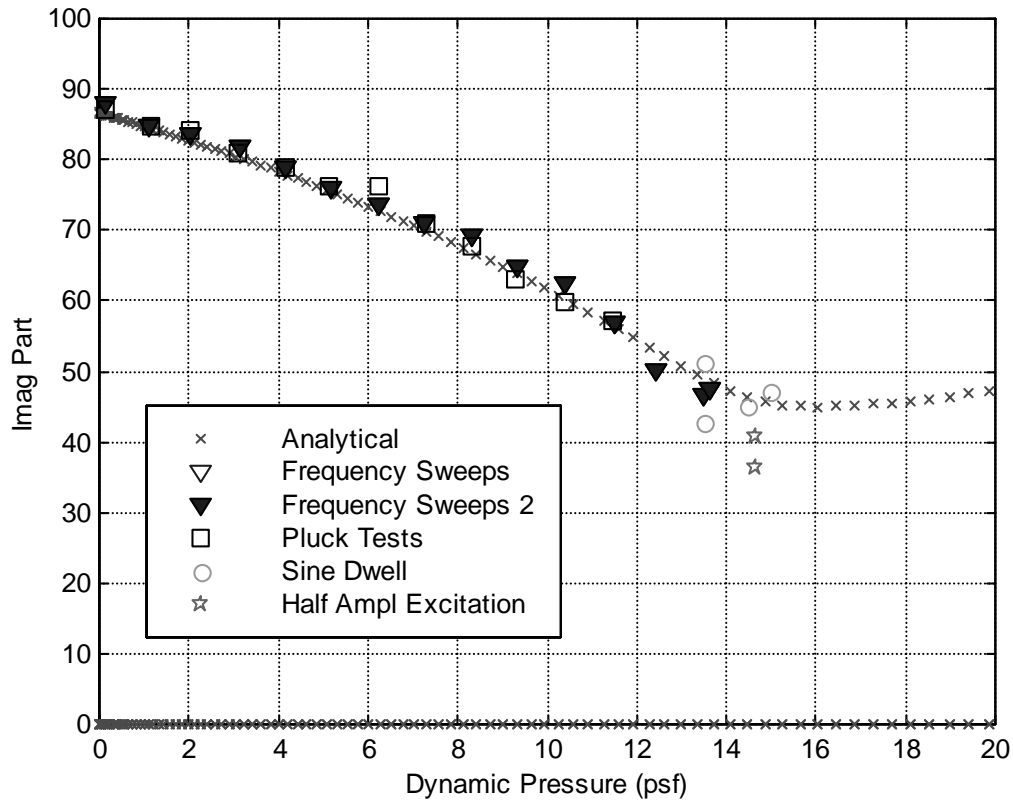


**Figure 78 Comparison of analytical and experimental results for configuration # 3; frequency versus dynamic pressure**

The real part, indicative of the damping, of the dynamic mode eigenvalue is plotted as a function of dynamic pressure in Figure 79. Three modes are shown from the analysis. The mode which destabilizes is a real mode which originated in the aerodynamic model. The mode which originates as the structural dynamic mode starts near zero and monotonically decreases throughout the dynamic pressure range presented. The third mode shown originated as the second real aerodynamic eigenvalue. The trends in the experimental curves follow the trend of the dynamic mode. In the vicinity of divergence, between 13 and 14.6 psf, the damping values could be interpreted as being representative

of any of the three modes shown from the analysis. Both analysis and experiment indicate that the dynamic mode is stable at the divergence dynamic pressure.

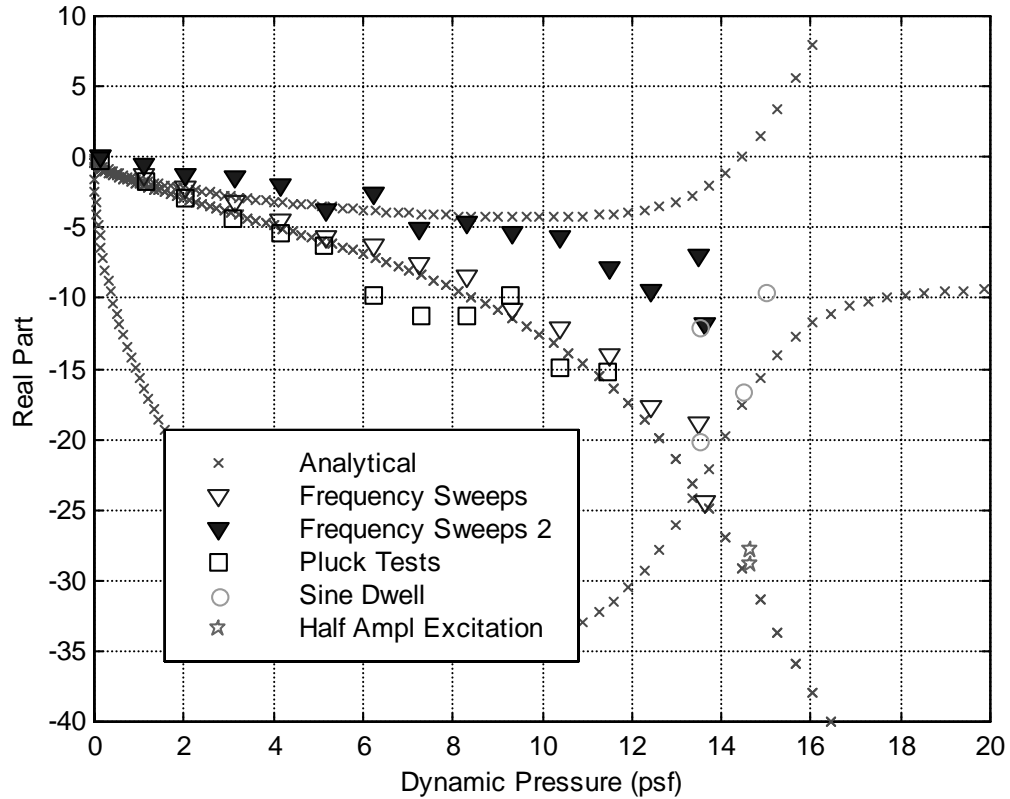


**Figure 79 Comparison of analytical and experimental results for configuration # 3; damping characteristic versus dynamic pressure**

The real and imaginary parts are combined in a root locus plot in Figure 80. For clarity, the complex aerodynamic modes have been removed from the chart. As the reduced velocity or dynamic pressure increases, the data progress generally downward and to the left.

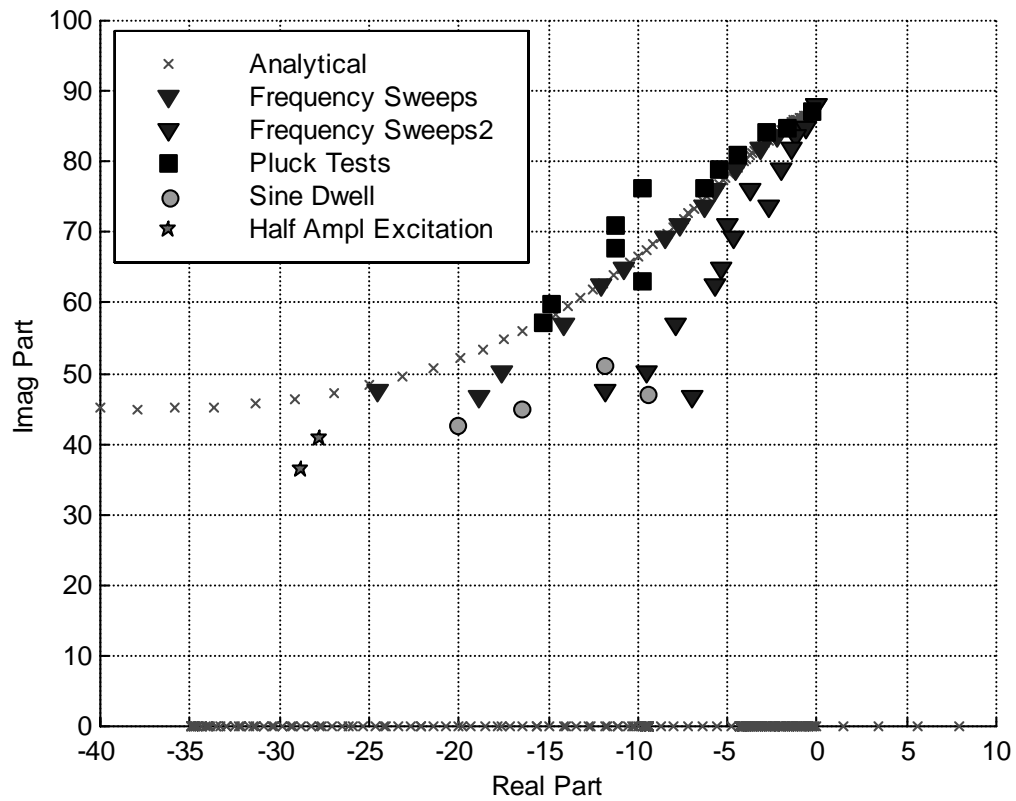


**Figure 80 Comparison of analytical and experimental results for configuration # 3; root locus as dynamic pressure is varied**

The dynamic pressure and frequency results for configuration # 3 are summarized in Table 16.

	Dynamic Pressure	Frequency	
	(psf)	(rads/sec)	(Hz)
<b>Analysis:</b>			
Air-off characteristics	0	87.3	13.9
Divergence	14.3	46.5	7.4
<b>Experiment:</b>			
Air-off characteristics	0	88.0	14.0
Linear divergence	15.2	45.2	7.2
Hard instability point	16.0	56.5	9.0
Southwell method results	15.0		

**Table 16 Comparison of analysis and experimental values for configuration # 3**

## CHAPTER FIVE

### SUMMARY OF RESULTS

#### *Aeroelastic Analysis Results*

Discrete time eigenanalyses of the aeroelastic systems revealed a static instability originating in an aerodynamic mode and also the characteristics of a noncritical structural dynamic mode for the aeroelastic systems examined. The analytical calculations of the divergence dynamic pressure agreed exactly with those predicted by the static equilibrium equations.

A database generated by varying the relevant nondimensional parameters revealed that the variation of dynamic mode frequency and damping at the divergence condition was a complex function of elastic axis position, radius of gyration and mass ratio. The dependence on torsional mode frequency was shown to be merely one of scaling. The parametric variations revealed that there are regions within the parameter space where divergence occurs and the dynamic mode becomes a real mode. The predominant category of behavior, however, for the family of configurations studied was shown to be a persistence of the dynamic mode, originating from the structural dynamics, at a non-zero frequency as the system diverges.

Additional insight into the modeling and physics associated with system behavior can be gained by examining the eigenvectors. The aerodynamic eigenmodes contain the essential information of the aerodynamic model. Two static aerodynamic modes exist which resemble the static pressure distribution over the wing elements. The complex aerodynamic modes are oscillatory wake modes, each at a constant frequency.

The dynamic mode eigenvector of the aeroelastic analysis yields information regarding the stability of the system. The vorticity participation factors can be analyzed to produce the modal frequency and damping. The degree of aeroelastic coupling is indicated by the amount of vorticity in the wing portion of the vorticity distribution contained in the eigenvectors. As velocity increases, the magnitude of the vorticities on the wing increases up to a maximum at the divergence condition.

The static mode of the aeroelastic system that diverges resembles a pressure coefficient distribution over the airfoil, similar to the real aerodynamic modes. All of the wake vorticity lies in the last element at low velocities. As velocity increases, all of the wake elements begin to participate in the mode. Near divergence, the participation of the last wake element drops sharply. The sign of the vorticity on this element changes, becoming out of phase with the airfoil vorticity and indicating a change in stability of the mode.

The modal vorticity ratios indicate the relative participation of the aerodynamics and structure in each mode. Subcritically, the traditional divergent configurations have dynamic modes which contain a large degree of aerodynamic participation. By contrast, the configurations studied here that diverge but also have a persistent non-zero frequency dynamic mode have modal vorticity ratios that reflect relatively low participation of the aerodynamics in that mode.

Eigenvector orthogonality studies showed that the physical mismatch in eigenvector quantities requires that each portion's orthogonality be considered separately. The wake vorticity portion of the dynamic aeroelastic mode eigenvector behave as if the aerodynamics are being forced at the modal frequency. Oscillations in the wake vorticities show up strongly in the eigenvector phasing if all components of the eigenvector are used in the comparison. The vorticity on the wing and the structural dynamics considered separately both showed that near zero flow velocity, the dynamic mode is nearly orthogonal to the real aerodynamic-originated modes. This reinforces the idea that there is no coupling between the structure and the aerodynamics until the system is subjected to a substantial flow velocity. This orthogonality is quickly lost as the airspeed is increased. As the velocity approaches divergence, the angle between the dynamic mode and the unstable mode changes. The modes start to lose their orthogonality, allowing energy transference between the modes.

### *Experimental Results*

All three experimental configurations diverged in the wind tunnel. The divergence dynamic pressure for configurations 1 and 2 was predicted by analysis to be identical and was measured to be nearly the same. The physical difference between these two configurations was that the first had the Tungsten trailing edge sections, while the second had the Plexiglass trailing edge. Classical steady divergence analysis and the analysis presented in this study indicate that the divergence dynamic pressure is independent of the inertial characteristics of the system. The experimental data agrees with this conclusion. Instability of each system was encountered at a slightly higher dynamic pressure than the linear theory predicted for divergence.

The three configurations tested all show the continued presence of the structural dynamic originated mode at non-zero frequency when the system becomes statically unstable. This was indicated by the time histories as well as frequency domain analysis.

The three configurations can be compared in terms of the instability onset. The onset of instability becomes more sudden and violent for typical sections with low inertias. This was experienced in the testing and can be observed by comparing time histories of destabilization, as well as by examining the divergence onset prediction results. For the

first configuration, with large torsional inertia provided by the Tungsten trailing edge, a gentle onset was encountered.

The destabilizing data at nonzero rigid angles of attack provide compelling evidence that the behavior of the dynamic mode is not a strong function of the static stability of the system. The frequency of the motion as the system destabilizes is close to the frequency that the mode possesses at zero angle of attack for the same dynamic pressure.

Data was also acquired for test conditions in excess of the linear system divergence dynamic pressure. At an angle of attack, between  $8^\circ$  and  $11\frac{1}{2}^\circ$ , the airfoil reached aerodynamic stall. An effect of stalling the airfoil was a reduction of the effective aerodynamic moment; dramatic yet understandable nonlinear behavior was thereby produced.



## CHAPTER SIX

### CONCLUSIONS & SUGGESTED FUTURE WORK

The analyses and experiment presented show that aeroelastic divergence can occur without a structural dynamic mode losing its oscillatory nature and becoming static. The aeroelastic coupling of the static aerodynamic and structural properties that produces divergence does not require the dynamic system behavior to cease. Aeroelastic changes in the dynamic mode behavior are governed not only by the stiffness, but by damping and inertial properties.

Typical section analysis and wind tunnel experiments demonstrated divergence, destabilization in a static sense, but at the same time demonstrated that a dynamic mode was still present in the system. These analytical and experimental results challenge the basic assumption that divergence occurs as a structural dynamic mode becomes static. It has been demonstrated that utilizing dynamic mode tracking to predict divergence onset experimentally is inadvisable. The combined aerodynamic and structural stiffness is shown to go to zero, but the dynamic mode frequency is shown to not necessarily disappear as the divergence condition is reached.

From this simple analysis and experiment, many possibilities open up for future research. In this work, a typical section with a single pitch structural freedom was employed. Suggested future investigations include extending the structural degrees of freedom to include the plunge mode. Inclusion of the plunge mode could simulate inclusion of rigid body or fuselage plunge motion. Study of a wing configuration would be a logical and useful extension also.

The nonlinear behavior which was observed in the present experiment also provides an opportunity for follow-on work. A more rigorous investigation of the behavior from a phase plane and energy level standpoint might offer interesting results. Additionally, a theoretical investigation of the stall behavior is suggested, perhaps utilizing the ONERA aerodynamic stall model<sup>1</sup>.

The analytical method of utilizing a discrete time aerodynamic model could potentially be extended to include doublet lattice aerodynamics. As a workhorse in the aeroelastic community, an analysis using doublet lattice in this fashion would provide direct comparison with current common analysis practices. Insight into the differences between roots produced by eigenanalysis and Pade approximation could be gained.

Experimentally, a simple extension of this work would be to make incremental changes in inertial properties in order to produce configurations where traditional divergence

---

<sup>1</sup> Tang, D. M., and E. H. Dowell, *Comments on the ONERA Stall Aerodynamic Model and its Impact on Aeroelastic Stability*

occurs. The current model would require relocation of the axis of rotation closer to the center of pressure and addition of mass, external to the airflow.

Acquisition and processing of unsteady pressure data offers additional research opportunities. The analytically determined eigenvector study has offered some insight into the phase relationship between the structural displacement and velocity and the vorticity distribution. The vorticity or pressure distribution, measured in an experiment, could provide additional insights. Potentially, pressure data could be examined and proper orthogonal decomposition techniques applied to examine aerodynamic modal participation in overall system response.

## APPENDIX A

### EQUATIONS OF MOTION

#### NOMENCLATURE

A	Aerodynamic matrix
ab	Distance from midchord to elastic axis
B	Aerodynamic matrix
b	Semi-chord
C	Aeroelastic force matrix
$C_1$	Intermediate calculation matrix, defined in equation 46
$C_2$	Intermediate calculation vector, defined in equation 47
$C_\alpha$	Pitch mode damping
D	Structural dynamic matrix
E	Downwash matrix
e	Elastic axis position, measured positive aft from the center of pressure
f	Aerodynamic load vector
I	Integral expression, see equation 40
$I_\alpha$	Torsional inertia
$J_1$	Intermediate structural dynamic matrix, defined in equation 54
$J_2$	Intermediate structural dynamic matrix, defined in equation 54
M	Number of aerodynamic elements on the wing
m	Mass
N	Total number of aerodynamic elements
n	Time step number
q	Generalized structural coordinates
q	Dynamic pressure
$r_\alpha$	Radius of gyration
$t_1$	Intermediate calculation vector, defined in equation 44
$t_2$	Intermediate calculation vector, defined in equation 45
U	Velocity
V	Reduced velocity, ( $V=U/\omega_\alpha b$ )
w	Downwash
x	Vector of locations of vortices in the aerodynamic model; chord-wise location
z	Discrete time eigenvalue
$\Delta t$	Time step size, temporal discretization
$\Delta x$	Aerodynamic element size, spatial discretization
$\Gamma$	Vorticity vector
K	Aerodynamic kernel function
$K_\alpha$	Torsional stiffness

$M$	Moment
$\alpha$	Aerodynamic relaxation factor
$\alpha$	Angle of attack
$\lambda$	Continuous time eigenvalue
$\mu$	Mass ratio
$\rho$	Density of air
$\omega_\alpha$	Frequency of torsional mode (radians/second)
$\xi$	Vector of locations of collocation points in the aerodynamic model
$\zeta$	Damping

### *Superscripts*

$n$	time step number
-----	------------------

### *Subscripts*

$\alpha$	Pertaining to the torsional degree of freedom
$\infty$	Freestream
$0$	Steady quantity
$1$	Unsteady quantity
$a$	Airfoil motion quantity
$EA$	Quantity at the elastic axis
$i,j$	Designation for an element of a matrix which lies in the $i$ th row, $j$ th column
$k$	$k$ th aerodynamic element
$M$	The $M$ th aerodynamic element
wake	Quantity in the wake
wing	Quantity on the wing

### *Aerodynamic equations*

The aerodynamic model was constructed by considering time-marching relationships as the vorticity develops on the wing and in the wake. For this study, the airfoil is modeled as a 2-dimensional flat plate. The airfoil and the wake are divided into segments, referred to as aerodynamic elements.

The vortex lattice aerodynamics are generated by placing vortices of strengths to be determined at points on the airfoil and in the wake. Control points, usually located aft of the vortex locations, are points where the boundary conditions must be satisfied. Typical placement is for the vortices to be located at the  $1/4$ -chord point of an aerodynamic element. The control points are typically placed at the  $3/4$ -chord locations of the elements.

There are 3 basic relationships contained in the vortex lattice equations, detailed in the following paragraphs, which are combined to form a matrix equation.

The velocity induced by the discrete vortices is set equal to the downwash caused by the airfoil's motion, Equation 24.

$$w_i^{n+1} = \sum_{j=1}^N K_{ij} \Gamma_j^{n+1} \quad \text{Equation 24}$$

$$i = 1, \dots, M$$

The kernel function,  $K_{ij}$ , relates the vorticity at point  $j$ ,  $\Gamma_j$ , to the downwash generated at point  $i$ ,  $w_i$ . For an isolated flat-plate airfoil in two-dimensional incompressible flow is given in Equation 25.

$$K_{ij} = \frac{1}{2\pi(x_i - \xi_j)} \quad \text{Equation 25}$$

Applying Kelvin's theorem generates the second basic relationship. Quoting Hall<sup>1</sup> "unsteady vorticity is shed into the wake; its strength is proportional to the time rate of change of circulation about the airfoil. If the time step is taken to be equal to the time it takes the vorticity to convect from one vortex station to the next, then the strength of the first vortex point in the wake at the time  $n+1$  is given by (Equation 26)"

$$\Gamma_{M+1}^{n+1} = - \sum_{j=1}^M (\Gamma_j^{n+1} - \Gamma_j^n) \quad \text{Equation 26}$$

Once the vorticity has been shed into the wake, it is convected in the wake at the freestream velocity. Convection provides the final relationship utilized in constructing the aerodynamic equations. Fixing the time step such that  $\Delta t = U \Delta x$ , this convection is described by Equation 27.

$$\Gamma_i^{n+1} = \Gamma_{i-1}^n \quad \text{Equation 27}$$

$$, i = (M + 2), (N - 1)$$

Because the wake is modeled with a finite length, the convection relationship for last vortex element must be treated specifically. "Otherwise, the starting vortex would disappear abruptly when it reached the end of the computational wake, producing a

---

<sup>1</sup> Hall, Kenneth C., *Eigenanalysis of Unsteady Flows about Airfoils, Cascades and Wing*

discontinuous change in the induced wash at the airfoil. To alleviate this difficulty, ... the vorticity is allowed to dissipate smoothly by using a relation factor, (Equation 28).”

$$\Gamma_i^{n+1} = \Gamma_{i-1}^n + \alpha \Gamma_i^n \quad \text{Equation 28}$$

$$, i = N$$

The equations are combined into the matrix expression, Equation 29. The Kernel function relationship between the vorticities on the wing and wake and downwashes on the wing form the first M rows of the equations. Kelvin’s theorem is seen as the (M+1) row. Convection in the wake appears in rows M+1 through N.

$$\begin{bmatrix} K_{11} & K_{12} & \dots & K_{1M} & K_{1(M+1)} & K_{1(M+2)} & \dots & \dots & K_{1N} \\ K_{21} & K_{22} & \dots & K_{2M} & K_{2(M+1)} & K_{2(M+2)} & \dots & \dots & K_{2N} \\ \vdots & \vdots & \ddots & \vdots & \vdots & \vdots & \ddots & \vdots & \vdots \\ K_{M1} & K_{M2} & \dots & K_{MM} & K_{M(M+1)} & K_{M(M+2)} & \dots & \dots & K_{MN} \\ 1 & 1 & \dots & 1 & 1 & 0 & 0 & 0 & 0 \\ 0 & 0 & \dots & 0 & 0 & 1 & 0 & 0 & 0 \\ \vdots & \vdots & \vdots & \vdots & \vdots & 0 & \ddots & \ddots & \vdots \\ \vdots & \vdots & \vdots & \vdots & \vdots & \vdots & \ddots & 1 & 0 \\ 0 & 0 & 0 & 0 & 0 & 0 & \dots & 0 & 1 \end{bmatrix} \begin{bmatrix} \gamma_{wing}(x_1) \\ \gamma_{wing}(x_2) \\ \vdots \\ \gamma_{wing}(x_M) \\ \gamma_{wake}(x_{M+1}) \\ \gamma_{wake}(x_{M+2}) \\ \vdots \\ \gamma_{wake}(x_N) \end{bmatrix}^{n+1} +$$

$$\begin{bmatrix} 0 & \dots & \dots & 0 & 0 & 0 & \dots & \dots & 0 \\ 0 & \dots & \dots & 0 & 0 & 0 & \dots & \dots & 0 \\ \vdots & \vdots & \vdots & \vdots & \vdots & \vdots & \vdots & \vdots & \vdots \\ 0 & 0 & 0 & 0 & 0 & 0 & 0 & 0 & 0 \\ -1 & \dots & \dots & -1 & 0 & 0 & \dots & \dots & 0 \\ 0 & \dots & \dots & 0 & -1 & 0 & 0 & 0 & 0 \\ \vdots & \vdots & \vdots & \vdots & 0 & -1 & \ddots & \ddots & \vdots \\ \vdots & \vdots & \vdots & \vdots & \vdots & \ddots & \ddots & 0 & 0 \\ 0 & \dots & \dots & 0 & 0 & \dots & 0 & -1 & -\alpha \end{bmatrix} \begin{bmatrix} \gamma_{wing}(x_1) \\ \gamma_{wing}(x_2) \\ \vdots \\ \gamma_{wing}(x_M) \\ \gamma_{wake}(x_{M+1}) \\ \gamma_{wake}(x_{M+2}) \\ \vdots \\ \gamma_{wake}(x_N) \end{bmatrix}^n = \begin{bmatrix} w(x_1) \\ w(x_2) \\ \vdots \\ w(x_M) \\ 0 \\ 0 \\ \vdots \\ 0 \end{bmatrix}^{n+1}$$

$$\text{Equation 29}$$

Rewriting Equation 29 in general terms produces Equation 30.

$$[A]\{\Gamma\}^{n+1} + [B]\{\Gamma\}^n = \{w\}^{n+1} \quad \text{Equation 30}$$

### *Aerodynamic moment equations*

The moment about the elastic axis generated by the aerodynamics is calculated using the integral expression in Equation 31. The distribution of vortex strength per unit length in the chord-wise direction is specified as  $\gamma(\xi)$ . The distance from the elastic axis to the mid-chord of the typical section, measured negative aft, is specified as  $ab$ .

$$M_{EA}(t) = \int_{-b}^b \rho(x - ab) \left[ U\gamma(x, t) + \frac{d}{dt} \int_{-b}^x \gamma(\xi, t) d\xi \right] dx \quad \text{Equation 31}$$

The moment equation is spatially discretized; approximations to the spatial integrals are made. In doing so, the vorticity,  $\gamma(\xi_k)$ , of each aerodynamic element is used. The moment arm for the force generated by each element's vorticity is the distance from the vortex location to the elastic axis.

The integral is broken apart into the steady and unsteady portions, denoted  $M_0$  and  $M_1$ , respectively as shown in Equation 32 and Equation 33.

$$M_0(t) = \int_{-b}^b \rho(x - ab) U \gamma(x, t) dx \quad \text{Equation 32}$$

$$M_1(t) = \int_{-b}^b \rho(x - ab) \left[ \frac{d}{dt} \int_{-b}^x \gamma(\xi, t) d\xi \right] dx \quad \text{Equation 33}$$

The moment at a given time,  $(n+1/2)\Delta t$ , is the sum of the steady and unsteady parts at that time, Equation 34.

$$M_{EA}((n + 1/2)\Delta t) = M_0((n + 1/2)\Delta t) + M_1((n + 1/2)\Delta t) \quad \text{Equation 34}$$

It is desired to express the moment in terms of the vortex strength distribution at integer time steps. Before proceeding, the notational convention exhibited in Equation 35 is introduced. The superscript represents the time step and the subscript represents the spatial element location.

$$\gamma(\xi_k, (n + 1/2)\Delta t) \equiv \gamma_k^{n+1/2} \quad \text{Equation 35}$$

The vortex strength at a location on the wing is then approximated at time  $(n + 1/2)\Delta t$  as the average of the value for the preceding and following time steps, Equation 36.

$$\gamma(x)^{n+1/2} \equiv \frac{\gamma(x)^n + \gamma(x)^{n+1}}{2} \quad \text{Equation 36}$$

The steady portion of the moment is approximated using a weighted summation of the vortex strength distribution on the airfoil as shown in Equation 37. The vortex associated with the  $k^{\text{th}}$  aerodynamic element is located at  $\xi_k$ . This is the location relative to the midchord and  $ab$  is the distance from the midchord to the elastic axis. Note that the control or downwash point of each aerodynamic element,  $x_k$ , is located half an element aft of the vortex location,  $x_k = \xi_k + \frac{1}{2} \Delta x$ . The moment arm for each vortex utilizes the vortex location. The moment computation, however, is evaluated for the downwash locations. This seeming incompatibility is necessitated by the equations to which the moment expression is coupled in forming the governing aeroelastic system equations.

$$M_0^{n+1/2} \equiv -U\rho\Delta x \sum_{k=1}^M (\xi_k - ab) \gamma_k^n \quad \text{Equation 37}$$

The summation is implemented as a vector product as shown in Equation 38.

$$M_0^{n+1/2} = -U\rho\Delta x [(\xi_1 - ab) \ (\xi_2 - ab) \ \dots \ (\xi_M - ab)] \{ \gamma_{wing} \}^n \quad \text{Equation 38}$$

The unsteady portion of the moment equation, Equation 39, is next evaluated at the time under consideration. In addition to the vortex strengths varying with time, there is a derivative expression which must be considered.

$$M_1^{n+1/2} = \int_{-b}^b \rho(x - ab) \left[ \frac{d}{dt} \int_{-b}^x \gamma(\xi) d\xi \right]^{n+1/2} dx \quad \text{Equation 39}$$

The internal integral at time  $n$ , evaluated at the downwash point of the  $k^{\text{th}}$  aerodynamic element is represented as  $I_k^n$ . The integral takes on a different value for each aerodynamic element, as the upper limit of integration is the chord-wise location of the control point for a given element. The integral expression can be approximated as a summation of contributions from each aerodynamic element, as shown in Equation 40. The contribution from each element is the elemental vortex strength multiplied by the length of the element which is upstream of the downwash point under consideration. That is, if an element is ahead of the element under consideration, its entire length is utilized in the calculation. If an element is behind the element under consideration, none of its strength is used in the calculation, so it is multiplied by zero. Three-fourths of the element being considered lies upstream of the downwash point, so  $\frac{3}{4}$  of that element's length is utilized in the summation. The summation is also presented in the form of a matrix multiplication suitable for implementation.



$$I_k^n = \int_{-b}^{x_k} \gamma(\xi) d\xi \cong \left(\frac{3}{4} \Delta x\right) \gamma_k^n + \Delta x \sum_{j=1}^{(k-1)} \gamma_j^n = \Delta x \begin{bmatrix} 1 & \frac{3}{4} & 0 & \dots & 0 \end{bmatrix}_{(1,k-1)} \{ \gamma_{wing} \}^n$$

Equation 40

The time derivative of the integral expression is approximated using the central difference theorem, Equation 41.

$$\left( \frac{dI}{dt} \right)^{n+1/2} \cong \left( \frac{\Delta I}{\Delta t} \right)^{n+1/2} = \frac{I^{n+1} - I^n}{\Delta t}$$

Equation 41

The unsteady portion of the moment is approximated by a double summation, Equation 42, where one of the summations is included in the evaluation of the integral expression.

$$M_1^{n+1/2} = \rho \Delta x \sum_{k=1}^M (\xi_k - ab) \left( \frac{I_k^{n+1} - I_k^n}{\Delta t} \right)$$

Equation 42

This can be written as a matrix product, Equation 43.

$$M_1^{n+1/2} \cong \rho U_\infty \begin{bmatrix} (\xi_1 - ab) & (\xi_2 - ab) & \dots & (\xi_M - ab) \end{bmatrix} \begin{bmatrix} \frac{3}{4} & 0 & \dots & 0 \\ 1 & \frac{3}{4} & \ddots & \vdots \\ \vdots & \ddots & \ddots & 0 \\ 1 & \dots & 1 & \frac{3}{4} \end{bmatrix} \left( \{ \gamma_{wing} \}^{n+1} - \{ \gamma_{wing} \}^n \right)$$

Equation 43

Implementing the calculations for the steady and unsteady moments can be combined utilizing the following matrix products, Equation 44 through Equation 47.

$$t_1 = \frac{\rho}{2} \begin{bmatrix} (\xi_1 - ab) & (\xi_2 - ab) & \dots & (\xi_M - ab) \end{bmatrix}$$

Equation 44

$$t_2 = \rho \begin{bmatrix} (\xi_1 - ab) & (\xi_2 - ab) & \dots & (\xi_M - ab) \end{bmatrix} \begin{bmatrix} \frac{3}{4} & 0 & \dots & 0 \\ 1 & \frac{3}{4} & \ddots & \vdots \\ \vdots & \ddots & \ddots & 0 \\ 1 & \dots & 1 & \frac{3}{4} \end{bmatrix}$$

Equation 45

Zero padding is required to make the dimensions such that the matrices fit into the aeroelastic system equations.

$$C_1 = -\frac{U_\infty}{mb^2} \begin{bmatrix} 0_{\langle 1, N_e \rangle} & 0_{\langle 1, N \rangle} \\ (t_1 - t_2) & 0_{\langle 1, N-M \rangle} \end{bmatrix} \quad \text{Equation 46}$$

$$C_2 = -\frac{U_\infty}{mb^2} \begin{bmatrix} 0_{\langle 1, N_e \rangle} & 0_{\langle 1, N \rangle} \\ (t_1 + t_2) & 0_{\langle 1, N-M \rangle} \end{bmatrix} \quad \text{Equation 47}$$

The dimensions of the coupling equations necessitate the formation of a vector expression where the aerodynamic moment equation is the second row.

$$f^{n+1/2} = \begin{Bmatrix} 0 \\ M_{ea} \end{Bmatrix}^{n+1/2} \quad \text{Equation 48}$$

A vector containing all of the vortex strengths is defined in Equation 49.

$$\Gamma^n = \left\{ \begin{Bmatrix} \gamma_1^n \\ \vdots \\ \gamma_N^n \end{Bmatrix} \right\} = \begin{Bmatrix} \gamma_1 \\ \vdots \\ \gamma_N \end{Bmatrix}^n \quad \text{Equation 49}$$

The general form of the aerodynamic moment equation is then shown in Equation 50. It is noted again that the first row is a zero element and only the wing elements of the vorticity distribution are utilized in computing the aerodynamic moment.

$$f^{n+1/2} = C_2 \Gamma^{n+1} + C_1 \Gamma^n \quad \text{Equation 50}$$

### *Structural Dynamic Equations*

The equations of motion for a typical section with a single pitch degree of freedom, possessing inertia, damping and stiffness characteristics, and subjected to an aerodynamic moment are given in Equation 51.

$$I_\alpha \{\ddot{\alpha}\} + C_\alpha \{\dot{\alpha}\} + K_\alpha \{\alpha\} = M_y \quad \text{Equation 51}$$

To write the equation in terms of nondimensional quantities, Equation 51 is divided by mass and semi-chord squared.

$$r_{\alpha} \{\ddot{\alpha}\} + \frac{C_{\alpha}}{mb^2} \{\dot{\alpha}\} + r_{\alpha}^2 \omega_{\alpha}^2 \{\alpha\} = \frac{M_y}{mb^2} \quad \text{Equation 52}$$

Equation 52 can be rewritten as a set of first order equations.

$$\begin{bmatrix} 1 & 0 \\ 0 & r_{\alpha}^2 \end{bmatrix} \begin{Bmatrix} \dot{\alpha} \\ \ddot{\alpha} \end{Bmatrix} + \begin{bmatrix} 0 & -1 \\ r_{\alpha}^2 \omega_{\alpha}^2 & \frac{C_{\alpha}}{mb^2} \end{bmatrix} \begin{Bmatrix} \alpha \\ \dot{\alpha} \end{Bmatrix} - \begin{Bmatrix} 0 \\ \frac{M_y}{mb^2} \end{Bmatrix} = \begin{Bmatrix} 0 \\ 0 \end{Bmatrix} \quad \text{Equation 53}$$

The above matrices and vectors are redefined in Equation 54.

$$[J_2] \{\dot{q}\} + [J_1] \{q\} + \{f\} = \{0\} \quad \text{Equation 54}$$

The time derivative of the generalized structural coordinate at a given time,  $(n+1/2)\Delta t$ , can be expressed approximately using the central difference theorem, Equation 55.

$$\left\{ \frac{dq}{dt} \right\}^{n+1/2} \cong \left\{ \frac{\Delta q}{\Delta t} \right\}^{n+1/2} = \frac{\{q\}^{n+1} - \{q\}^n}{\Delta t} \quad \text{Equation 55}$$

The generalized structural coordinate can be approximately using the central difference theorem.

$$\{q\}^{n+1/2} \cong \frac{1}{2} (\{q\}^{n+1} + \{q\}^n) \quad \text{Equation 56}$$

The first order equations can be written for a specific instant in time. Writing them at time  $(n+1/2)\Delta t$  and employing the central difference approximations shown in Equations 55 and 56 leads to Equation 57.

$$\left[ \frac{J_2}{\Delta t} + \frac{J_1}{2} \right] \{q\}^{n+1} + \left[ \frac{-J_2}{\Delta t} + \frac{J_1}{2} \right] \{q\}^n + \{f\}^{n+1/2} = \{0\} \quad \text{Equation 57}$$

This is now in the general form represented in the main text of the paper.

$$D_2 q^{n+1} + D_1 q^n + f^{n+1} = 0 \quad \text{Equation 58}$$

### ***Downwash Equations***

The downwash is defined as the vertical component of velocity on the airfoil,  $w_a$ , positive downward. Using the velocity potential function,  $\phi$ , the downwash can be expressed in

terms of temporal and spatial derivatives. The vertical displacement,  $z$ , is defined as positive upward.

$$w_a = -\frac{\partial \phi}{\partial z} = -\frac{\partial z_a}{\partial t} - U_\infty \frac{\partial z_a}{\partial x} \quad \text{Equation 59}$$

The vertical motion of the airfoil,  $z_a$ , is a function of both spatial coordinate,  $x$ , and time,  $t$ . The motion can be represented in terms of a spatial mode shape,  $\Phi(x)$ , and a temporal generalized coordinate,  $\xi(t)$ .

$$z_a(x, t) = \Phi(x) \xi(t) \quad \text{Equation 60}$$

The downwash expression can then be written as Equation 61, where the negative signs have been incorporated into the mode shapes.

$$w_a = \Phi(x) \frac{\partial \xi(t)}{\partial t} + U_\infty \frac{\partial \Phi(x)}{\partial x} \xi(t) \quad \text{Equation 61}$$

The generalized coordinates and their derivatives with respect to time can be written as a single vector.

$$\{q\} = \begin{Bmatrix} \xi(t) \\ \frac{\partial \xi(t)}{\partial t} \end{Bmatrix} \quad \text{Equation 62}$$

The downwash equation can be written in first order form.

$$w_a = \begin{bmatrix} U_\infty \frac{d\Phi(x)}{dx} & \Phi(x) \end{bmatrix} \{q\} \quad \text{Equation 63}$$

Specifically, for the pitch degree of freedom, the vertical displacement of a typical section is given in Equation 64. The displacement at a point on the airfoil is a function of its location,  $x$ , measured relative to the center of rotation. The sign convention utilized is positive distance is forward of the center of rotation and angle of attack is positive nose-up.

$$z_a = -x\alpha \quad \text{Equation 64}$$

$$\Phi(x) = -x \quad \text{Equation 65}$$

$$\xi(t) = \alpha \quad \text{Equation 66}$$

The downwash equation, written for a single point on the wing, in general form is given in Equation 67.

$$w_a = [-U_\infty \quad -x] \{q\} \quad \text{Equation 67}$$

Formally, the generalized coordinate vector is comprised of the structural generalized coordinate and its first derivative with respect to time. For the case of the pitch only typical section the generalized coordinate is the angle of attack.

$$\{q\} = \begin{Bmatrix} \xi \\ \dot{\xi} \end{Bmatrix} = \begin{Bmatrix} \alpha \\ \dot{\alpha} \end{Bmatrix} \quad \text{Equation 68}$$

The downwash equations can be written in the general form presented in the main text.

$$w^n = E q^n \quad \text{Equation 69}$$

## APPENDIX B

### EIGENVECTOR INVARIANCE UNDER TRANSFORMATION

#### NOMENCLATURE

A	State matrix
B	A general matrix
C	Jordan form matrix
F	Matrix which is similar to B
P	A general matrix
R	Transformation matrix
s	Laplace variable
t	Time
T	Time step size
X(s)	Laplace domain representation of state variable vector
x(t)	Vector of state variables
y	Substitution variable for state vector, see equation 89
z	Unit delay operator, discrete time eigenvalue
$\Phi$	State transition matrix
$\beta$	Eigenvalues of B matrix
$\lambda$	Continuous time eigenvalue
$\xi$	Eigenvector

#### SUBSCRIPTS

A, B, C, F	Pertaining to matrix A, B, C, or F
c	Continuous time quantity
d	Discrete time quantity
$e^{AT}$	Pertaining to discrete time matrix, $e^{AT}$

Theorem: The eigenvectors for the associated continuous and discrete time state space systems are equal.

Proof.

- Let the continuous time state space equations for the unforced system be given by Equation 70.

$$\dot{x}(t) = Ax(t)$$

*Equation 70*

A solution can be obtained by utilizing the Laplace transform, Equation 71, where  $X(0)$  is the state of the system at the initial condition.

$$sX(s) - X(0) = AX(s) \quad \text{Equation 71}$$

The system of equations can be rearranged as in Equation 72.

$$X(s) = [Is - A]^{-1} X(0) \quad \text{Equation 72}$$

Define the state transition matrix at a time  $t$ ,  $\Phi_c(t)$ , as in Equation 73.

$$\Phi_c(t) = L^{-1} \{ [Is - A]^{-1} \} = I + At + \frac{1}{2!} A^2 t^2 + \frac{1}{3!} A^3 t^3 + \dots \quad \text{Equation 73}$$

Rewriting in summation notation produces Equation 74.

$$\Phi_c(t) = \sum_{k=0}^{\infty} \frac{A^k t^k}{k!} = e^{At} \quad \text{Equation 74}$$

$$x(t) = \Phi_c(t) x(0) \quad \text{Equation 75}$$

A non-zero initial time can be accommodated in these equations,

$$x(t) = \Phi_c(t - t_0) x(t_0) \quad \text{Equation 76}$$

$$\Phi_c(t - t_0) = \sum_{k=0}^{\infty} \frac{A_c^k (t - t_0)^k}{k!} \quad \text{Equation 77}$$

- To obtain the discrete time model with a time step size of  $T$  seconds, Equation 77 can be evaluated at time  $t = nT + T$ , with  $t_0 = nT$ .

$$x(nT + T) = \Phi_c(nT + T - nT) x(nT) \quad \text{Equation 78}$$

$$\mathbf{x}((n+1)T) = \Phi_c(T)\mathbf{x}(nT) \quad \text{Equation 79}$$

In discrete time notation, the time step size is generally omitted.

$$\mathbf{x}[n+1] = \Phi_c(T)\mathbf{x}[n] \quad \text{Equation 80}$$

The discrete time state space equations for the unforced system are given by Equation 81.

$$\mathbf{x}(n+1) = \mathbf{A}_d \mathbf{x}(n) \quad \text{Equation 81}$$

Comparing Equation 80 Equation 81, the continuous and discrete time system matrices are related as in Equation 82.

$$\mathbf{A}_d = e^{AT} = \Phi_c(T) = \sum_{k=0}^{\infty} \frac{T^k}{k!} \mathbf{A}^k \quad \text{Equation 82}$$

The discrete time equations can thus be written as Equation 83.

$$\mathbf{x}(n+1) = e^{AT} \mathbf{x}(n) \quad \text{Equation 83}$$

- For the continuous time relationship, assume the time variation to be simple harmonic motion, Equation 84.

$$\mathbf{x}(t) = e^{\lambda t} \mathbf{x}(0) = e^{\lambda t} \xi_A \quad \text{Equation 84}$$

An eigenvalue problem is formulated by substitution of the simple harmonic solution into the state space equations, Equation 85.

$$\mathbf{A} \xi_A = \xi_A \lambda \quad \text{Equation 85}$$

- For the discrete time relationships, approximate the time variation as a unit delay, Equation 86. The response of the system as an initial time is given a new notation.

$$\mathbf{x}(n) = z^n \mathbf{x}(0) = z^n \xi_{e^{AT}} \quad \text{Equation 86}$$

An eigenvalue problem is formulated by substitution of the unit delay solution into the discrete time state space equations, Equation 87.

$$e^{AT} \xi_{e^{AT}} = z \xi_{e^{AT}} \quad \text{Equation 87}$$

- Thus the theorem can be restated as the eigenvectors of  $\mathbf{A}$ , denoted  $\xi_A$ , are equal to the eigenvectors of  $\mathbf{A}_d$ , denoted  $\xi_{e^{AT}}$ .



Following the development of Kincaid and Cheney<sup>1</sup>, “if we possess the Jordan form  $C$  of  $A$  and we know the transformation (given in Equation 88), then we can change variables by substitution as in (Equation 89).”

$$\xi_A^{-1} A \xi_A = C \quad \text{Equation 88}$$

$$\mathbf{x} = \xi_A \mathbf{y} \quad \text{Equation 89}$$

The differential equation, Equation 70, and the prescribed initial condition,  $\mathbf{x}(0)$ , can be recast as Equation 90 and Equation 91.

$$\xi_A \dot{\mathbf{y}} = A \xi_A \mathbf{y} \quad \text{Equation 90}$$

$$\xi_A \mathbf{y}(0) = \mathbf{x}(0) \quad \text{Equation 91}$$

Rearranging Equation 90 produces Equation 92.

$$\dot{\mathbf{y}} = \xi_A^{-1} A \xi_A \mathbf{y} \quad \text{Equation 92}$$

Substituting the Jordan form matrix,  $C$ , from Equation 88 produces Equation 93.

$$\dot{\mathbf{y}} = C \mathbf{y} \quad \text{Equation 93}$$

This set of equations can then be solved, Equation 94.

$$\mathbf{y}(t) = e^{CT} \mathbf{y}(0) \quad \text{Equation 94}$$

Substituting this solution into Equation 89 and reverting to the original state vector produces Equation 95.

$$\mathbf{x}(t) = \xi_A e^{CT} \xi_A^{-1} \mathbf{x}(0) \quad \text{Equation 95}$$

Comparing Equation 95 with Equation 75 leads to the expression of the matrix exponential in terms of the Jordan form matrix exponential, Equation 96.

$$e^{AT} = \xi_A e^{CT} \xi_A^{-1} \quad \text{Equation 96}$$

---

<sup>1</sup> Kincaid, David, and Ward Cheney, *Numerical Analysis: Mathematics of Scientific Computing*, page 562

The eigenvectors of a general matrix, B, can be obtained from the eigenvectors of any similar matrix, F, if the transformation between the two matrices is known. The transformation relationship is defined, Equation 97 by the matrix R.

$$\mathbf{R}^{-1}\mathbf{F}\mathbf{R} = \mathbf{B} \quad \text{Equation 97}$$

The eigenvalues of a matrix are invariant with coordinate transformation. The eigenvalues of both matrices F and B are denoted  $\beta$  in this development. The eigenvectors are denoted  $\xi_B$ . The eigenvalue problem for B is given by Equation 98.

$$\mathbf{B}\xi_B = \xi_B\beta \quad \text{Equation 98}$$

Substituting Equation 97 and premultiplying by R results in Equation 100.

$$\mathbf{R}^{-1}\mathbf{F}\mathbf{R}\xi_B = \xi_B\beta \quad \text{Equation 99}$$

Examining this equation, it is recognized that this is an eigenvalue equation for the matrix F, where the eigenvectors are shown to be  $\mathbf{R}\xi_B$ .

$$\mathbf{F}(\mathbf{R}\xi_B) = (\mathbf{R}\xi_B)\beta \quad \text{Equation 100}$$

$$\xi_F = \mathbf{R}\xi_B \quad \text{Equation 101}$$

The preceding derivation is now applied to Equation 96, making the following substitutions.

$$\mathbf{R} = \xi_A^{-1} \quad \text{Equation 102}$$

$$\mathbf{F} = \mathbf{e}^{CT} \quad \text{Equation 103}$$

$$\mathbf{B} = \mathbf{e}^{AT} \quad \text{Equation 104}$$

This results in an expression for the discrete time system matrix in terms of the Jordan form system matrix and the continuous time eigenvectors, Equation 105, and a relationship among the eigenvectors, Equation 106.

$$\mathbf{e}^{AT} = \left(\xi_A^{-1}\right)^{-1} \mathbf{e}^{CT} \xi_A^{-1} \quad \text{Equation 105}$$

$$\xi_{e^{CT}} = \xi_A^{-1} \xi_{e^{AT}} \quad \text{Equation 106}$$

C is the Jordan form matrix associated with A, the continuous time system matrix. The formula for taking the exponential of a general matrix, P is given in Equation 107.

$$e^{PT} = \sum_{k=0}^{\infty} \frac{T^k}{k!} P^k \quad \text{Equation 107}$$

If P is a matrix of diagonal elements, the  $P^k$  is a matrix of each element to the  $k^{\text{th}}$  power. Thus for P diagonal,  $e^{PT}$  is diagonal and of the same matrix dimension. Thus,  $e^{CT}$  is a Jordan form matrix. The case of the non-diagonal Jordan matrix has been left to the truly inspired reader.

The eigenvectors of a Jordan form matrix form an identity matrix.

$$\xi_{e^{CT}} = I \quad \text{Equation 108}$$

Using this relationship and Equation 106 leads to Equation 109.

$$I = \xi_A^{-1} \xi_{e^{AT}} \quad \text{Equation 109}$$

Therefore, the eigenvectors associated with the continuous and discrete time state space equations are equal, Equation 110.

$$\xi_A = \xi_{e^{AT}} \quad \text{Equation 110}$$

## BIBLIOGRAPHY

Afolabi, Dare, Ramana M.V. Pidaparti, and Henry Y. T. Yang. *Flutter Prediction Using an Eigenvector Orientation Approach*. AIAA Journal, vol 36, no 1 (January 1998).

Bendiksen, Oddvar O. *An Energy Approach to Flutter Suppression and Aeroelastic Control*. Presented at the Confederation of European Aerospace Societies (CEAS) International Forum on Aeroelasticity, Williamsburg, VA., June 1999.

Bisplinghoff, R.E., Holt Ashley, Roger L. Halfman. *Aeroelasticity*. Mineola, New York: Dover Publications, 1996.

Bisplinghoff, Raymond L., and Holt Ashley. *Principles of Aeroelasticity*. New York: Dover 1975.

Blair, Maxwell. *Wind Tunnel Experiments on the Divergence of Swept Wings with Composite Structures*. Air Force Wright Aeronautical Laboratories Technical Report AFWAL-TR-82-3018, October 1982.

Brogan, William L. *Modern Control Theory*. Englewood Cliffs, New Jersey: Prentice Hall, 1985, 2<sup>nd</sup> edition.

Chen, P.C. *A Damping Perturbation Method for Flutter Solution: The g-Method*. Presented at the Confederation of European Aerospace Societies (CEAS) International Forum on Aeroelasticity, Williamsburg, VA., June 1999.

Clough, Ray W., and Joseph Penzien. *Dynamics of Structures*. San Francisco, California: McGraw-Hill, 1975.

Cole, Stanley R, James R. Florance, Lee B. Thompson, Charles V. Spain and Ellen P. Bullock. *Supersonic Aeroelastic Instability Results for a NASP-like Wing Model*. NASA Technical Memorandum 107739, April 1993.

Cole, Stanley R. *Divergence Study of a High-Aspect Ratio, Forward-swept Wing*. NASA Technical Memorandum 87682, June 1986.

Cunningham, Herbert J. *Analysis of Preflutter and Postflutter Characteristics with Motion-Matched Aerodynamic Forces*. NASA Technical Paper 1232, July 1978.

*DAQCard-700 User Manual*.

Dashcund, David E. *The Development of a Theoretical and Experimental Model for the Study of Active Suppression of Wing Flutter*. MAE Technical Report 1496T, December 1980, Department of Mechanical and Aerospace Engineering, Princeton University.

Diederich, Franklin W. *Divergence of Delta and Swept Surfaces in the Transonic and Supersonic Speed Ranges*. NACA reference document prepared for the structures and materials panel of advisory group for aeronautical research and development. Washington, D. C.: April 1956.

Diederich, Franklin W., and Bernhard Budiansky. *Divergence of Swept Wings*. NACA Technical Note no. 1680, Washington: August 1948.

Diederich, Franklin W., and Kenneth A. Foss. *Static Aeroelastic Phenomena of M-, W-, and  $\square$ -Wings*. NACA Research Memorandum, February 9, 1953.

Dowell, Earl H., Edward F. Crawley, Howard C. Curtiss Jr, David A. Peters, Robert H. Scanlan and Fernando Sisto. *A Modern Course in Aeroelasticity*. Dordrecht, the Netherlands: Kluwer 1995.

Dowell, Earl H., Kenneth C. Hall, and Michael C. Romanowski. *Eigenmode analysis in unsteady aerodynamics: reduced order models*. Applied Mechanics Review Vol. 50, #6, p371-385, June 1997.

Edwards, John E., *Unsteady Aerodynamic Modeling and Active Aeroelastic Control*. SUDAAR 504, February 1977, Stanford University, Center for systems research.

Ewins, D. J. *Modal Testing: Theory and Practice*. Taunton, Somerset, England: Research Studies Press Limited, 1984.

Hall, Kenneth C. *Eigenanalysis of Unsteady Flows about Airfoils, Cascades and Wings*. AIAA Journal Vol. 32, No. 12, December 1994.

Hardin, J.C. *Introduction to Time Series Analysis*. NASA Reference Publication 1145, Nov 1990.

Hassig, Hermann J. *An Approximate True Damping Solution of the Flutter Equation by Determinant Iteration*. Journal of Aircraft, vol. 8, no. 11, November 1971.

Haykin, Simon. *Adaptive Filter Theory*. Upper Saddle River, New Jersey: Prentice Hall, 1996, 3<sup>rd</sup> edition.

Johnson, R.E., and Fred L. Kiokemeister. *Calculus*. Boston: Allyn and Bacon, Inc., January 1962.

Karpel, Mordechai, and Sherwood Tiffany Hoadley. *Physically Weighted Approximations of Unsteady Aerodynamic Forces Using the Minimum-State Method*. NASA Technical Paper 3025, March 1991.

Kincaid, David, and Ward Cheney. *Numerical Analysis: Mathematics of Scientific Computing*. Pacific Grove, California: Brooks/Cole Publishing Company, 1991.

Krone, Norris J., Jr. *Divergence Elimination with Advanced Composites*. AIAA Paper no. 75-1009, August 1975.

Martin, D. J., and C. E. Watkins. *Transonic and Supersonic Divergence Characteristics of Low-aspect-ratio Wings and Controls*. Paper presented at the IAS 27<sup>th</sup> annual meeting, New York, New York, January 26-29, 1959. IAS Report no. 59-58.

Miller, Gerald D., John H. Wykes and Michael J. Brosnan. *Rigid Body-Structural Mode Coupling on a Forward Swept Wing Aircraft*. AIAA 82-0683, May 1982.

NASA Dryden Flight Research Center photo gallery world wide web page.  
<http://www.dfrc.nasa.gov/gallery/photo/X-29/index.html>

Nissim, E. *Flutter Analysis Using a New Complex  $p$ -Method*. Presented at the Confederation of European Aerospace Societies (CEAS) International Forum on Aeroelasticity, Rome, June 1997.

Oppenheim, Alan V., and Ronald W. Schaffer. *Discrete-time Signal Processing*. Englewood Cliffs, New Jersey: Prentice Hall, 1989.

Phillips, Charles L., and H. Troy Nagle, Jr. *Digital Control System Analysis and Design*. Englewood Cliffs, New Jersey: Prentice Hall, 1984.

Pugsley, A.G., and G.A. Naylor. *The Divergence Speed of an Elastic Wing*. Aeronautical Research Committee Reports and Memoranda no. 1815, London: His Majesty's Stationery Office, October 8, 1937.

Ricketts, Rodney H., and Robert V. Doggett, Jr. *Wind-tunnel Experiments on Divergence of Forward-Swept Wings*. NASA Technical Paper 1685, August 1980.

Robbins, T. *Another Roadside Attraction*. New York: Bantam Books Inc., 1990.

Rock, Stephen M., and Daniel B. DeBra. *Prediction and Experimental Verification of Transient airfoil Motion in a Small Wind Tunnel*. AIAA-81-0052, January 1981.

Rodden, William P., and Bernhard Stahl. *A Strip Method for Prediction of Damping in Subsonic Wind Tunnel and Flight Flutter Tests*. Journal of Aircraft, vol. 6, no. 1 (Jan-Feb 1969).

Rodden, W.P., R.L. Harder, and E. Dean Bellinger. *Aeroelastic Addition to NASTRAN*. NASA Contractor Report 3094, 1979.

Rodden, William P. *Approximate Solutions in Unsteady Aerodynamics. Presented to the seminar on aeroelasticity: theory and applications*, Centro Italiano Recerche Aerospaziali, Capua, Italia, September 2-6, 1996.

Rodden, William P., and E. Dean Bellinger. *Aerodynamic Lag Functions, Divergence, and the British Flutter Method*. *Journal of Aircraft*, vol. 19, no. 7 (July 1982).

Rodden, William P., and E. Dean Bellinger. *Unrestrained Aeroelastic divergence in a Dynamic Stability Analysis*. *Journal of Aircraft*, vol. 19, no. 9 (September 1982).

Rodden, William P., and Erwin J. Johnson. *MSC/NASTRAN Aeroelastic Analysis User's Guide*. Version 68, 1994.

Schuster, Lawrence S. and William A. Lokos. *Current Flight Test Experience Related to Structural Divergence of Forward-Swept Wings*. NASA Technical Memorandum 100445, 1988.

Sefic, Walter J., and Cleo M. Maxwell. *X-29A Technology Demonstrator Flight Test Program Overview*. NASA Technical Memorandum 86809, May 1986.

Shirk, M.H., T.J. Hertz, and T.B. Weisshaar. *Aeroelastic Tailoring- Theory, Practice, and Promise*. *Journal of Aircraft*, vol. 23, no. 1, January 1986.

Tang, D. M., and E. H. Dowell. *Comments on the ONERA Stall Aerodynamic Model and its Impact on Aeroelastic Stability*. *Journal of Fluids and Structures*, vol. 10, 1997.

Vepa, R. *On the use of Pade Approximants to Represent Unsteady Aerodynamic Loads for Arbitrarily Small Motions of Wings*. AIAA paper no. 76-17, 1976.

Weisshaar, Terrence B. *Forward Swept Wing Static Aeroelasticity*. Air Force Flight Dynamics Laboratory Technical Report AFFDL-TR-79-3087, June 1979.

Weisshaar, Terrence B., *Fundamentals of Static Aeroelasticity*. Course notes for Aeronautical Engineering Course 556, West Lafayette, Indiana: Purdue University 1987

<b>REPORT DOCUMENTATION PAGE</b>			Form Approved OMB No. 0704-0188	
Public reporting burden for this collection of information is estimated to average 1 hour per response, including the time for reviewing instructions, searching existing data sources, gathering and maintaining the data needed, and completing and reviewing the collection of information. Send comments regarding this burden estimate or any other aspect of this collection of information, including suggestions for reducing this burden, to Washington Headquarters Services, Directorate for Information Operations and Reports, 1215 Jefferson Davis Highway, Suite 1204, Arlington, VA 22202-4302, and to the Office of Management and Budget, Paperwork Reduction Project (0704-0188), Washington, DC 20503.				
<b>1. AGENCY USE ONLY</b> (Leave blank)		<b>2. REPORT DATE</b> November 2000	<b>3. REPORT TYPE AND DATES COVERED</b> Technical Publication	
<b>4. TITLE AND SUBTITLE</b> Dynamic Investigation of Static Divergence: Analysis and Testing			<b>5. FUNDING NUMBERS</b>  WU 522-31-31-02	
<b>6. AUTHOR(S)</b> Jennifer Heeg				
<b>7. PERFORMING ORGANIZATION NAME(S) AND ADDRESS(ES)</b>  NASA Langley Research Center Hampton, VA 23681-2199			<b>8. PERFORMING ORGANIZATION REPORT NUMBER</b>  L-18003	
<b>9. SPONSORING/MONITORING AGENCY NAME(S) AND ADDRESS(ES)</b>  National Aeronautics and Space Administration Washington, DC 20546-0001			<b>10. SPONSORING/MONITORING AGENCY REPORT NUMBER</b>  NASA/TP-2000-210310	
<b>11. SUPPLEMENTARY NOTES</b>				
<b>12a. DISTRIBUTION/AVAILABILITY STATEMENT</b> Unclassified-Unlimited Subject Category 05      Distribution: Standard Availability: NASA CASI (301) 621-0390			<b>12b. DISTRIBUTION CODE</b>	
<b>13. ABSTRACT</b> (Maximum 200 words) The phenomenon known as aeroelastic divergence is the focus of this work. The analyses and experiment presented here show that divergence can occur without a structural dynamic mode losing its oscillatory nature. Aeroelastic divergence occurs when the structural restorative capability or stiffness of a structure is overwhelmed by the static aerodynamic moment. This static aeroelastic coupling does not require the structural dynamic system behavior to cease, however. Aeroelastic changes in the dynamic mode behavior are governed not only by the stiffness, but by damping and inertial properties. The work presented here supports these fundamental assertions by examining a simple system: a typical section airfoil with only a rotational structural degree of freedom. Analytical results identified configurations that exhibit different types of dynamic mode behavior as the system encounters divergence. A wind tunnel model was designed and tested to examine divergence experimentally. The experimental results validate the analytical calculations and explicitly examine the divergence phenomenon where the dynamic mode persists.				
<b>14. SUBJECT TERMS</b> Aeroelasticity; Divergence; Eigenanalysis; Static aeroelasticity; Aerodynamic lag divergence			<b>15. NUMBER OF PAGES</b> 160	
			<b>16. PRICE CODE</b> A08	
<b>17. SECURITY CLASSIFICATION OF REPORT</b> Unclassified	<b>18. SECURITY CLASSIFICATION OF THIS PAGE</b> Unclassified	<b>19. SECURITY CLASSIFICATION OF ABSTRACT</b> Unclassified	<b>20. LIMITATION OF ABSTRACT</b> UL	